10/29/95

CONTRACTOR REPORT

SAND95–0329
Unlimited Release
UC–721

Formulation and Computational Aspects of Plasticity and Damage Models With Application to Quasi-Brittle Materials

Zhen Chen, Howard L. Schreyer
New Mexico Engineering Research Institute
University of New Mexico
Albuquerque, NM 87131

Prepared by
Sandia National Laboratories
Albuquerque, New Mexico 87185 and Livermore, California 94550
for the United States Department of Energy
under Contract DE-AC04-94AL85000

Printed September 1995

Issued by Sandia National Laboratories, operated for the United States Department of Energy by Sandia Corporation.

Available to DOE and DOE contractors from
Office of Scientific and Technical Information
PO Box 62
Oak Ridge, TN 37831

Prices available from (615) 576-8401, FTS 626-8401

Available to the public from
National Technical Information Service
US Department of Commerce
5285 Port Royal RD
Springfield, VA 22161

NTIS price codes
Printed copy: A06
Microfiche copy: A01

SAND95-0329
Unlimited Release
Printed September 1995

Distribution
Category UC-721

Formulation and Computational Aspects of Plasticity And Damage Models With Application To Quasi-Brittle Materials*

Zhen Chen and Howard L. Schreyer
New Mexico Engineering Research Institute
University of New Mexico
Albuquerque, NM 87131

ABSTRACT

The response of underground structures and transportation facilities under various external loadings and environments is critical for human safety as well as environmental protection. Since quasi-brittle materials such as concrete and rock are commonly used for underground construction, the constitutive modeling of these engineering materials, including post-limit behaviors, is one of the most important aspects in safety assessment.

From experimental, theoretical, and computational points of view, this report considers the constitutive modeling of quasi-brittle materials in general and concentrates on concrete in particular. Based on the internal variable theory of thermodynamics, the general formulations of plasticity and damage models are given to simulate two distinct modes of microstructural changes, inelastic flow and degradation of material strength and stiffness, that identify the phenomenological nonlinear behaviors of quasi-brittle materials. The computational aspects of plasticity and damage models are explored with respect to their effects on structural analyses. Specific constitutive models are then developed in a systematic manner according to the degree of completeness. A comprehensive literature survey is made to provide the up-to-date information on prediction of structural failures, which can serve as a reference for future research.

* Work performed under Contract No. 88101-02 for Performance Assessment Division (6342), Sandia National Laboratories

ACKNOWLEDGMENT

The authors thank B.M. Butcher (Div. 6345), M.G. Marietta (Div. 6342), F.T. Mendenhall (Div. 6345) and D. E. Munson (Div. 6121) of Sandia National Laboratories for their review of this report.

CONTENTS

CONTENTS (Continued)

Figures

Figures (Continued)

This Page Intentionally Left Blank

1. INTRODUCTION

The response of underground structures and transportation facilities to various external loadings is critical for environmental protection. Since quasi-brittle materials such as concrete, rock, and soil are commonly adopted for underground construction, the constitutive modeling and failure analysis of these engineering materials are currently under active research in both the academic and industrial worlds.

Nonlinear stress-strain responses of engineering materials arise mainly from two distinct modes of microstructural changes: one is inelastic flow and the other is the damaging or degradation of material properties. The damage process dominates in the cases of quasi-brittle materials under mechanical, thermal, and chemical effects, such as creep, stress corrosion, and leakage of seals. Inelastic flow, which is reflected through permanent deformation, is the consequence of a dislocation process along preferred slip planes, as in metals, or particle motion and rearrangement, as in quasi-brittle materials. Because the number of bonds between material particles is hardly altered during the inelastic process, the material stiffness remains insensitive to this mode of microstructural motion, and the change of strength is characterized by the inelastic strain hardening phenomenon. On the other hand, the nucleation, crushing, and coalescence of microcracks and microvoids result in debonding between particles, which is reflected through the damaging of material stiffness and strength. In general, both modes are present and interacting, and the structure is said to fail when macrocracks occur and propagate through it. Within the framework of continuum theories, elastoplasticity and damage mechanics are the tools to simulate the inelastic flow and the damaging process, respectively.

This report considers constitutive modeling of quasi-brittle materials in general and concentrates on concrete in particular. Nonlinear behavior in the pre-peak regime of quasi-brittle materials has been discussed extensively in the technical literature [Chen, 1982; Desai and Siriwardane, 1984; Neville and Brooks, 1987; Yazdani and Schreyer, 1988]. The failure mechanism of quasi-brittle materials is still not clear, although experimental data beyond the peak strength have been documented for some quasi-brittle materials [Van Mier, 1984; Shah and Gopalaratnam, 1985; Norman, 1990] and some promising results have been obtained toward modeling damage softening with localization [Bazant and Pijaudier-Cabot, 1988; Krajcinovic, 1989; Chen and Schreyer, 1990]. The main nonlinear features characterizing quasi-brittle materials can be summarized as follows:

1. The enhancement of material strength and apparent ductility under increasing confining pressure,
2. The difference between compressive and tensile strengths,
3. Hysteretic unloading loops,

4. The inelastic volume change as reflected through shear enhanced compaction and dilatation, and
5. The anisotropic degradation of the material strength and stiffness accompanied by the localization of intense deformation.

In this report, both inelastic hardening and damage softening of concrete will be considered based on the previous work. Considerable detail will be given to the pre-peak response, which has direct application in current engineering design codes. The following is an outline of the report.

Chapter 2 explains the notation and nomenclature that are used to express the models and solution algorithms. Based on experimental observations summarized in Chapter 3, the first section of Chapter 4 provides a general formulation of elastoplasticity as a phenomenological means to reflect the micromechanical change caused by inelastic flow. The theory of elastoplasticity is well established for metals for which the hypotheses are simple and supported by experimental evidence. Unfortunately, appropriate hypotheses for quasi-brittle materials are different than those for metals and are not agreed upon by everyone. Examples involve the need for nonassociated flow rules, dilatation, shear enhanced compaction and pressure dependence. Hence, the name "inelastic flow" is used here for quasi-brittle materials instead of "plastic flow" as used originally for metals. Numerical algorithms are discussed in the second section for solving the elastoplastic constitutive equations. The parts that are unique to a particular model are identified, and then only these parts need to be changed if the model is altered. Although the development of constitutive models has been actively researched for the past ten years, the associated computational aspects have barely been touched. Here, various plasticity models will be made available to users of advanced computational codes.

After the general formulation and computational aspects of elastoplasticity are discussed, specific models are developed where the degree of complexity is used as a guide for ordering the subject material. Starting with the elastic-perfectly plastic models in Chapter 5, it is shown in Chapter 6 how additional features can provide improvements for simulating the hardening behavior of concrete. The characteristic features for each model are described and compared with features that are representative for the class of materials under consideration. In this context, the advantages and disadvantages of each model are explored. Also, the material parameters associated with each model are identified and a method for determining each parameter is given.

The experimental, theoretical, and computational aspects associated with damage mechanics are discussed in Chapter 7. Simple damage models are then proposed in Chapter 8 to show the potential of damage mechanics in failure assessments of underground structures.

Finally, conclusions are made. This report should be beneficial with regard to the following:

1. The report provides an outline of the formulation and computational aspects of plasticity and damage mechanics for an engineer who is new to this field,
2. The report will be of assistance in selecting a suitable constitutive model and a corresponding algorithm for geotechnical design projects, and
3. The report gives the basis for modifying and incorporating additional features into an existing constitutive model.

2. NOTATION AND NOMENCLATURE

Three notations are commonly used in continuum mechanics: direct, indicial, and matrix. The direct notation has the advantage of forcing one to think conceptually rather than becoming overly involved with the details of the equations. However, to solve specific problems, coordinate systems and base vectors must be defined and then the concept of components of vectors and tensors arise. Indicial notation is an abbreviated form for representing vectors and tensors in terms of components and base vectors. If base vectors are excluded, the resulting equations involve components only, and these equations can be expressed in either indicial or matrix form. The latter is most often used in numerical algorithms.

It is assumed that the reader has an appropriate background in tensor calculus, matrix algebra, and continuum mechanics [Malvern, 1969; Golub and van Loan, 1983]. Hence, only special notations and nomenclature will be specified here. The governing equations will be expressed in terms of direct notation with boldface letters denoting tensors of first or higher orders. Indicial notation will be used if there is a possibility of confusion concerning the use of components. The summation convention is adopted for repeated Latin subscripts. Symbols are defined when they first appear in the text.

Because stress and strain tensors are often decomposed into a spherical and a deviatoric part for modeling purpose, it is convenient to introduce the spherical, $\boldsymbol{P}^s$, and deviatoric, $\boldsymbol{P}^d$, orthogonal projections. Then the fourth-order identity tensor is decomposed as follows:

$$\boldsymbol{I} = \boldsymbol{P}^s + \boldsymbol{P}^d \tag{2.1}$$

with the definitions

$$\boldsymbol{I} = \frac{1}{2}(\delta_{ik}\delta_{jl} + \delta_{il}\delta_{jk})\boldsymbol{e}_i \otimes \boldsymbol{e}_j \otimes \boldsymbol{e}_k \otimes \boldsymbol{e}_l \tag{2.2-1}$$

and

$$\boldsymbol{P}^s = \frac{1}{3}\boldsymbol{i} \otimes \boldsymbol{i} \tag{2.2-2}$$

where $\boldsymbol{i}$ is the second order identity tensor (i.e., the Kronecker delta in indicial notation). From the definitions in Eqs. (2.1) and (2.2), it follows that

$$\boldsymbol{P}^s : \boldsymbol{P}^s = \boldsymbol{P}^s \tag{2.3-1}$$

$$\boldsymbol{P}^d:\boldsymbol{P}^d=\boldsymbol{P}^d \tag{2.3-2}$$

$$\boldsymbol{P}^d:\boldsymbol{P}^s=\boldsymbol{P}^s:\boldsymbol{P}^d=\boldsymbol{0} \tag{2.3-3}$$

$$\boldsymbol{P}^s:\boldsymbol{T}=\boldsymbol{T}^s \tag{2.3-4}$$

$$\boldsymbol{P}^d:\boldsymbol{T}=\boldsymbol{T}^d \tag{2.3-5}$$

$$\boldsymbol{P}^s:\boldsymbol{T}^s=\boldsymbol{T}^s \tag{2.3-6}$$

$$\boldsymbol{P}^s:\boldsymbol{T}^d=\boldsymbol{0} \tag{2.3-7}$$

$$\boldsymbol{P}^d:\boldsymbol{T}^d=\boldsymbol{T}^d \tag{2.3-8}$$

$$\boldsymbol{P}^d:\boldsymbol{T}^s=\boldsymbol{0} \tag{2.3-9}$$

in which $\boldsymbol{T}^s$ and $\boldsymbol{T}^d$ are the spherical and deviatoric parts of the second-order tensor $\boldsymbol{T}$, respectively.

The above properties of the orthogonal projections provide a convenient way to formulate the stress-strain relations. The isotropic elasticity tensor, for example, can be written as

$$\boldsymbol{E}=\lambda \boldsymbol{i}\otimes\boldsymbol{i}+2\mu\boldsymbol{I}=(3\lambda+2\mu)\boldsymbol{P}^s+2\mu\boldsymbol{P}^d \tag{2.4}$$

where λ and μ are Lame's constants. As can be seen from Eq. (2.4), the spherical and deviatoric parts of material deformation can be treated separately for isotropic elasticity.

3. EXPERIMENTAL OBSERVATIONS

Depending on the level of stress, concrete may respond in a linear or nonlinear manner. At low stress levels, it may be safely assumed that concrete is adequately represented by a linear elastic constitutive model. At stress levels approaching 30% of the uniaxial compressive strength, the occurrence of microcracking results in nonlinear inelastic response and a suitable nonlinear constitutive model should be invoked.

In this chapter, representative examples of data from conventional laboratory tests on plain concrete will be presented. Since rock behaves in a similar manner, this will give the reader an idea of the mechanical response features typically exhibited by many quasi-brittle materials. Because of the scatter of experimental data associated with machine precision, testing techniques, and statistical variation of material properties, the primary goal of constitutive modeling should be set in the prediction of essential features observed from experiments.

The experimental data most often available are from uniaxial stress, biaxial stress, and triaxial stress tests. A common problem encountered by the analyst, however, is the lack of complete data even for the simplest of tests, the uniaxial compression test. Unless requested, the lateral strains are often not recorded and thus the volume change characteristics are unknown. When laboratory work is performed with the intent to develop constitutive models, all components of stress and strain need to be recorded. In any case, a fundamental question that must be answered is to what level of loading must the material be adequately modeled.

3.1 Uniaxial Stress Behavior

Some typical uniaxial compressive stress-strain data are shown in Figure 3-1. The peak (ultimate or failure) strength is denoted f_c. Depending on the particular concrete-mix design various strengths may be obtained [White, 1977]. While different strengths are obtainable, the compressive axial strain at which the peak stress is reached is fairly constant at $\varepsilon_1 = -0.002$. The tensile (lateral or radial) strains $(\varepsilon_2, \varepsilon_3)$ corresponding to the peak stress are approximately 0.001.

For stresses up to 30% of the peak strength, concrete exhibits nearly linear-elastic behavior. Above this level, the stress-strain curve shows decreasing curvature up to f_c. The descending branch following the peak is referred to as the post-peak or apparent softening regime. The softening of concrete is accompanied by a localized region with large

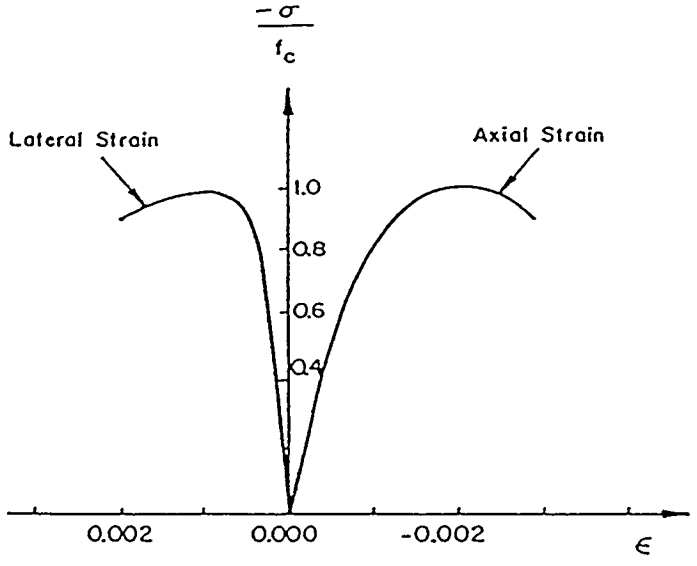

Figure 3-1. Typical stress-strain data of concrete under uniaxial compression, with f_c being peak strength [Kupfer et al., 1969].

deformations and is the subject of intense research at this time. It will be covered in some detail in Chapter 7.

The different regions associated with the uniaxial stress-strain curve are basically caused by the effects of microcracks, and the features of these regions can be specified as follows based on micromechanical experiments via X-Ray Radiography, Laser Holographic Interferometry, and Acoustic Emission. With loading up to about 30% of the peak strength, the cracks existing prior to loading do not appear to grow, and hence, elastic response is recorded. Between 30-50% of the peak strength, stable crack growth is observed. For stresses between 50-75% of the peak strength, new cracks begin to form in the mortar. At about 75% of the peak strength, the volumetric strain begins to increase, namely, the sample begins to expand. This expansion is termed dilatancy and is also a feature common to quasi-brittle materials. The progressive failure of the specimen near its peak strength results from microcracking of the mortar and the mortar-aggregate interface. The existence of both kinds of cracks yields zones of damage. With continued straining, the descending branch of the stress-strain curve is obtained and macrocracks appear on the sample surface.

Some of the information that can be obtained from uniaxial compressive testing are Young's Modulus, E, Poisson's ratio, ν, and the peak strength, f_c.

Young's Modulus may also be estimated by using the ACI (American Concrete Institute) empirical formula:

$$E = 33w^{1.5}f_c \tag{3.1}$$

where E is in psi, w is the unit weight in lb/ft^3, and f_c is the uniaxial compressive strength in psi .

Poisson's ratio is defined from elastic strains as follows:

$$\upsilon = -\frac{\varepsilon_r}{\varepsilon_v} \tag{3.2}$$

where ε_r and ε_v denote the radial (lateral) and axial (longitudinal) strains, respectively, with tensile strain positive and compressive strain negative. Typical values of Poisson's ratio for concrete range from 0.15 to 0.22, with 0.19 normally being used.

While not common, uniaxial tensile tests are sometimes performed. The ratio of uniaxial tensile to uniaxial compressive strengths varies considerably but usually a value of 0.1 is used in concrete design.

The obvious point to be made here is that concrete is much stronger in compression than in tension and a constitutive model should be capable of simulating this phenomenon.

3.2 Biaxial Stress Behavior

Biaxial loading implies the application of either a traction or displacement boundary condition on two faces of a cubical specimen. The third direction is traction free. If stresses are applied in the $x_1 - x_2$ plane, the failure surface can be plotted in the plane of the principal stresses of σ_1 and σ_2 .

It has been found that the maximum strength occurs when the biaxial compressive stress ratio is approximately 0.5. This increase is about 25% with respect to uniaxial compression. For equal biaxial compressive stresses, the increase is about 15%. Under biaxial compression-tension, the ultimate compressive strength decreases almost linearly as the tensile stress is increased. There is little difference between the biaxial tensile strength and the uniaxial tensile strength.

In general, the ductility of concrete subjected to biaxial stress states depends on whether these stresses are compressive or tensile. In the case of biaxial compression, the average compressive strain at which the peak stress is reached is about –0.003 as compared

to –0.002 in uniaxial compression. The average tensile strain at failure varies from 0.002 to 0.004 when both stresses are compressive.

In biaxial compression-tension, the magnitude at failure of the compressive and tensile strains decreases with increasing tensile stress. Thus, concrete becomes less ductile when the tensile stress is increased. This is as expected since we know from experience that concrete behaves in a brittle fashion in tension.

In general, concrete fails because of tensile splitting with the fracture surfaces orthogonal to the maximum principal tensile strain. It has been observed that the maximum strength envelope is not greatly dependent on the loading path for normal weight concretes. The weight of concrete is determined by the content of mixtures [White, 1977]. Figure 3-2 shows a typical biaxial failure envelope and Figure 3-3 illustrates typical stress-strain relationships under biaxial compression, with β_p being uniaxial compressive stress at peak.

The volume-change characteristics show a behavior similar to those of uniaxial curves. Under increasing compression, the concrete first compacts and eventually dilates because of microcracking, as shown in Figure 3-4(a) for triaxial stress behavior. The experimental data available do not clearly indicate when dilation first occurs. Some data indicate that it occurs just after the peak compressive stress while other data show that it occurs well before the peak is reached. Possible explanations for these differences appear to be the method of load application and the measurement techniques [Chen, 1982].

3.3 Hydrostatic Stress Behavior

If a hydrostatic compressive loading ($\sigma_1 = \sigma_2 = \sigma_3$) is performed, no failure is possible. However, the stress-strain behavior is nonlinear as indicated in Figure. 3-5.

3.4 Triaxial Stress Behavior

The typical triaxial test is performed on a cylindrical sample so that the loading is the same in two directions. Initially, hydrostatic compression is applied to the sample, and the resulting stress state is called confining stress. Next, increasing (triaxial compression) or decreasing (triaxial extension) one of the loading components is accomplished until failure is reached. In general, the larger the compressive confining stress the larger will be the compressive failure strength. A typical example of stress-strain data under triaxial compression for different confining stresses is shown in Figure 3-4(b). The increases in both ductility and strength with an increase in confining pressure are features common to

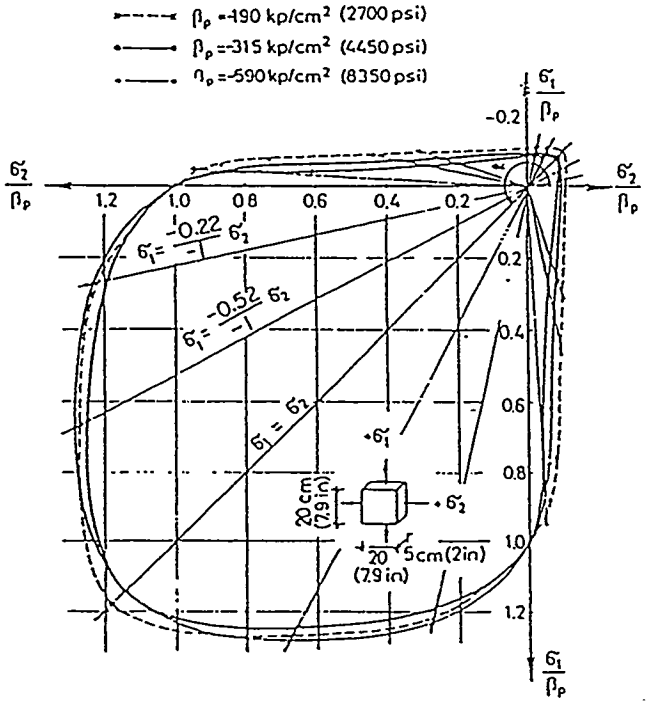

Figure 3-2. Biaxial failure envelope of concrete in σ_1 - σ_2 plane, with β_p being uniaxial compressive stress at peak [Kupfer et al., 1969].

all quasi-brittle materials. Because of these pressure-dependent phenomena, quasi-brittle materials are also called frictional materials in order to distinguish from nonfrictional materials such as metals. Plots of normal pressure ($P = \sigma_{ii}/3$) versus volumetric strain ($\varepsilon^v = \varepsilon_{ii}$) for different confining stresses are given in Figure 3-4(a). An interesting result is that with the triaxial tests where shear is present, more volumetric strain is observed than for the hydrostatic case. This phenomenon is called shear enhanced compaction.

3.5 Uniaxial Strain Behavior

Another test performed commonly on soils that sometimes is used with concrete is the uniaxial strain test. Here, no deformation is allowed in two directions while in the other direction the strain component is decreased. Because of the confinement, no failure strength is observed. Although no example is given here, almost invariably greater compaction for the same confining stress is shown by the uniaxial strain specimen as compared to the hydrostatic response, which is simply another manifestation of shear enhanced compaction.

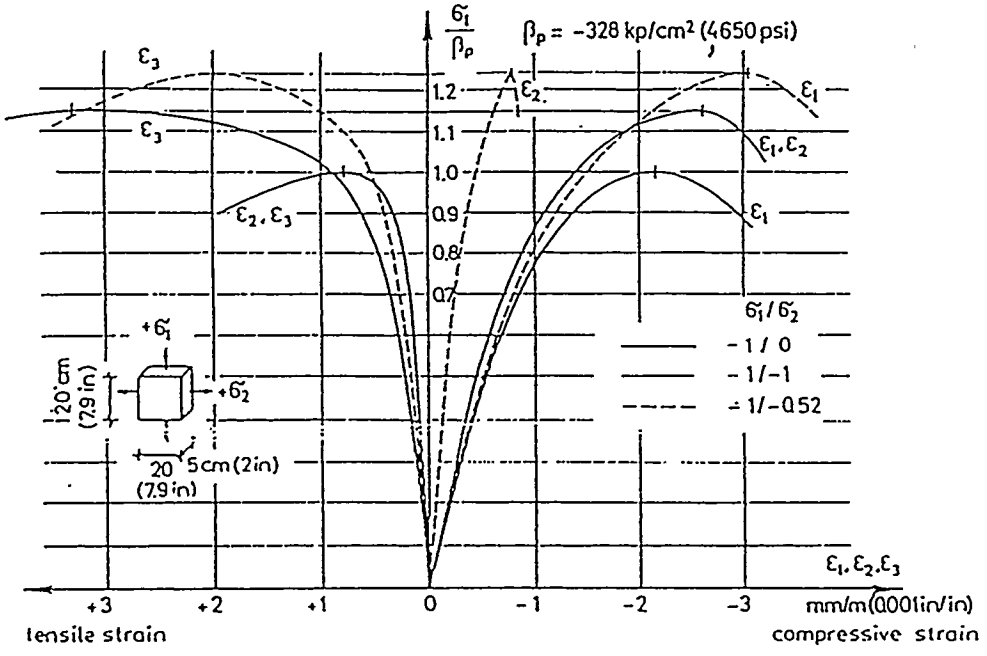

Figure 3-3. Stress-strain data of concrete under biaxial compression, with β_p being uniaxial compressive stress at peak [Kupfer et al., 1969].

3.6 Summary

It appears that for large values of compressive hydrostatic pressure the failure surface in the deviatoric plane is circular, while at lower values, the failure surface is somewhat triangular in shape. This triangular shape requires the use of three stress invariants to accurately model the failure of concrete [Schreyer and Babcock, 1985]. Various failure theories based on elastoplasticity for frictional materials will be presented later in the report. In summary:

1. The uniaxial stress test indicates that 3 phases occur during compressive loading:
   (a) linear-elastic up to about 30% of the peak strength,
   (b) nonlinear phase from 30-75% of , and
   (c) damage associated with microcracks for loading beyond 75% of .
2. In biaxial compression, the concrete is at least as strong as in uniaxial compression, but in biaxial compression-tension, the compressive strength decreases as the tensile stress is increased.
3. The axial strength of concrete increases as confining stress increases. The sample also becomes more ductile at high confining stresses.

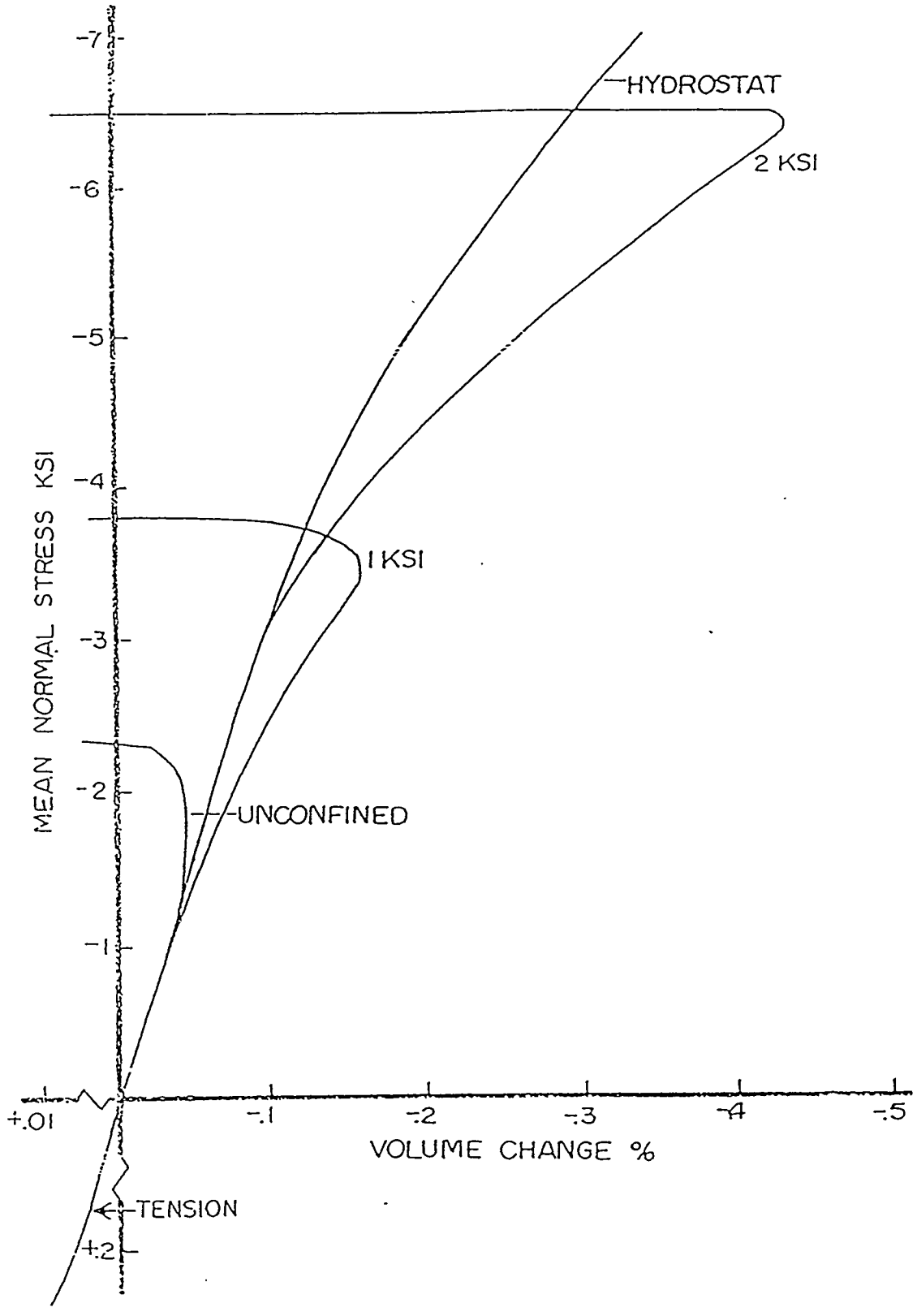

(a) Mean normal stress $\left(\frac{1}{3}\sigma_{ii}\right)$ versus volume change (ε_{ii}) for different confining pressures

Figure 3-4. Response of concrete under triaxial compression [Green and Swanson, 1973].

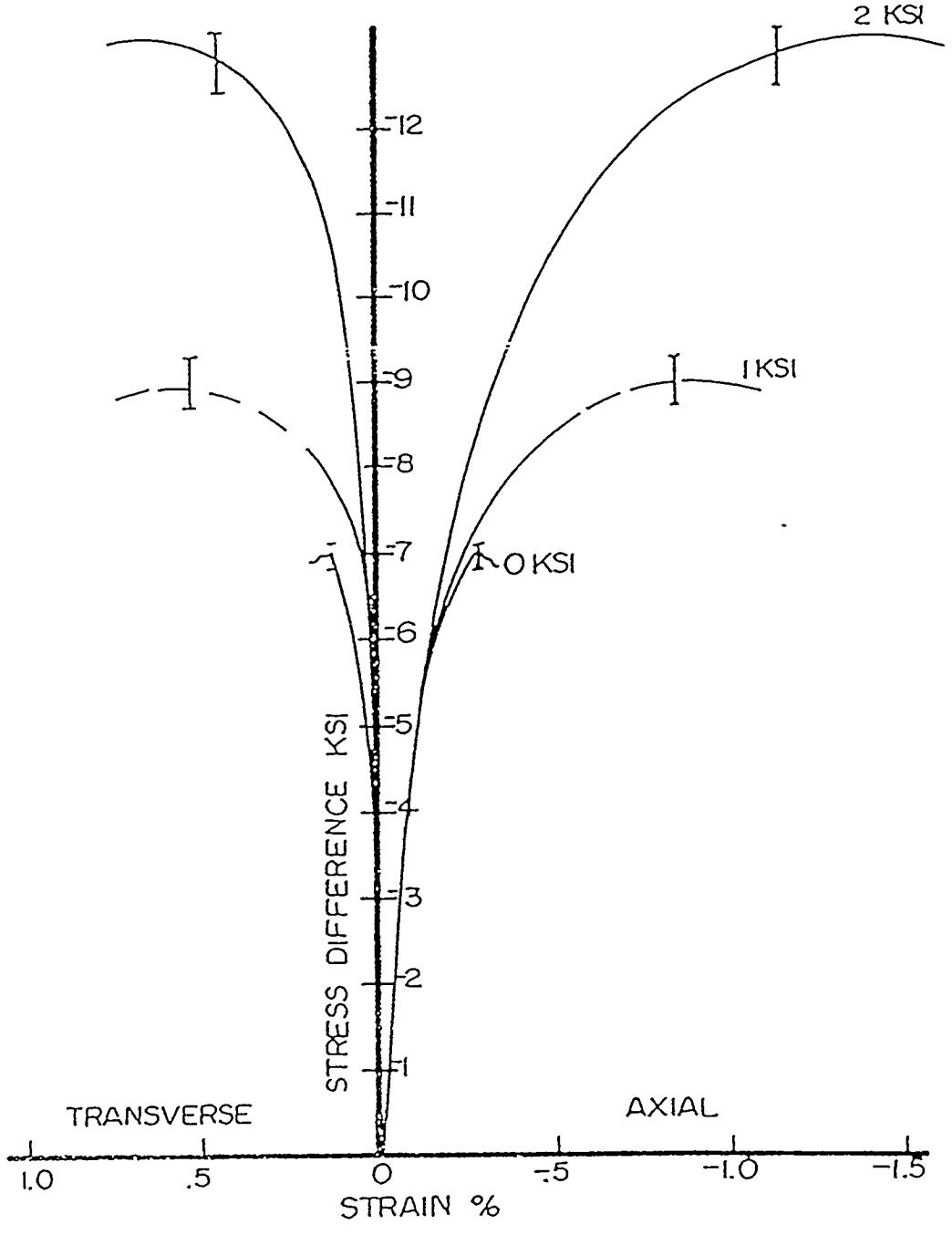

(b) Stress difference versus axial and transverse strains for different confining pressures, with data scatter shown by bars

Figure 3-4. (continued) Response of concrete under triaxial compression [Green and Swanson, 1973].

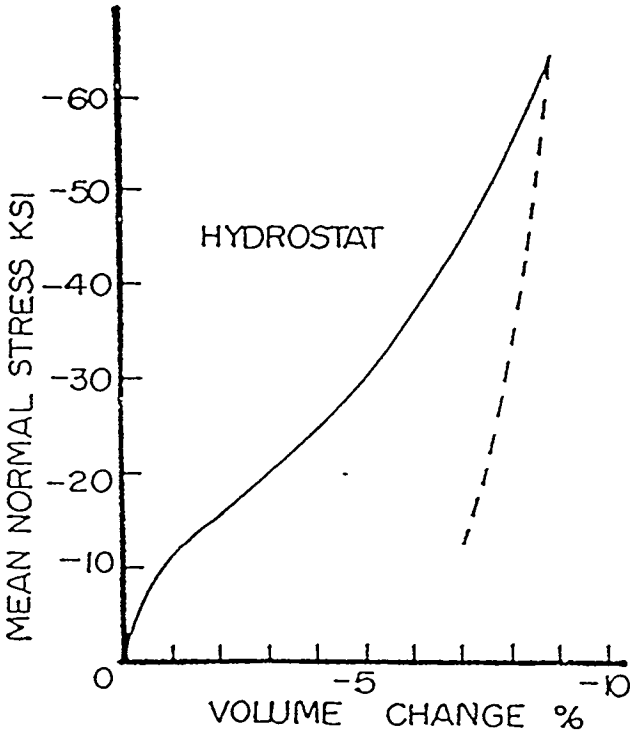

Figure 3-5. Loading and unloading of the pressure $\left(\frac{1}{3}\sigma_{ii}\right)$ versus volumetric strain (ε_{ii}) response under hydrostatic compression [Green and Swanson, 1973].

4. The presence of shear stresses (deviatoric stress) results in increased (negative) volumetric strain called shear enhanced compaction.
5. Near failure, the concrete sample will begin expanding. This increase in (positive) volumetric strain is called dilation or dilatation.

4. ELASTOPLASTICITY

The theory of elastoplasticity is an approach commonly used to model both recoverable (elastic) and irrecoverable (plastic or permanent) deformations of engineering materials under external loads. The development of this theory stemmed from the description of metals where permanent deformation is associated with the dislocation process along preferred slip planes. Plasticity was then adapted to quasi-brittle materials where permanent deformation is caused by particle motion and rearrangement. Because of the different micromechanical structure, quasi-brittle materials exhibit some unique features such as shear enhanced compaction, dilatation, and pressure dependence, which are in addition to the hardening and rate dependence observed for metals. Hence, there is some objection to the use of the theory of elastoplasticity in the case of quasi-brittle materials. In order to model concrete in this report, the theory of elastoplasticity will be modified and referred to as inelasticity theories because there exist several approaches. It should be emphasized that a meaningful constitutive model must be consistent with the micromechanical nature of the material considered, although both phenomenological and micromechanical methods are employed for modeling purpose. In other words, mathematical descriptions of material behavior with certain assumptions should always satisfy relevant physical theories. Because of the limitations of current experimental techniques, however, the understanding of the micromechanical natures of engineering materials is still not complete. Hence, the accuracy of the constitutive models developed at a given time represents the level of science and technology corresponding to that time.

It is assumed that the reader is generally familiar with the theory of elastoplasticity [Hill, 1950; Malvern, 1969; Martin, 1975; Chen, 1982]. Therefore, basic equations in a general format are summarized without detailed specifications in the first section, but more attention will be given to the discussion of a constitutive equation solver in the second section of this chapter. The ensuing chapters address specific inelastic models developed from the general elastoplastic formulations, which are suitable for concrete.

4.1 General Formulation

In the theory of elastoplasticity, it is postulated that there exists a domain in stress space. The hypersurface bounding the domain is called the plastic yield surface, which is assumed to be closed and convex. The yield surface divides the constitutive feature into three regimes: a region inside the surface that defines elasticity, a region on the surface that defines elastoplasticity, and a region outside the surface that can not be reached. If the yield

surface remains fixed during plastic deformations, it simulates the perfectly plastic behavior of materials. If the yield surface expands out from a lower bound to a higher bound, the surface reflects hardening behavior. The lower bound is known as the elastic surface because there are no plastic deformations below this bound. The higher bound is called the peak, ultimate, or failure limit surface. If the yield surface contracts from the peak limit surface to some residual value in a controlled manner, it models one part of the apparent softening behavior, namely, the material strength softens with the loading process. The modeling of softening will not be discussed until Chapter 7. The yield surface is considered to be a function of both stress and certain internal variables that record the part of the stress history involving plastic behavior and other sources affecting yielding. Generally, the yield surface can be written as

$$f(\boldsymbol{\sigma}, I_i) = 0 \qquad i = 1, 2, \ldots, n \qquad (4.1)$$

where σ is the stress tensor, and I_i are internal variables that can be functions of zeroth or higher order tensors and represent the internal constitution of the material. If the stress appears in Eq. (4.1) only through the stress invariants, the yield surface is said to be isotropic, otherwise it is anisotropic.

In order to simulate those paths that are load dependent, the classical theory of elastoplasticity is based on a differential form. Usually, the total strain is known, and the stress, elastic strain, and plastic strain are solved from the differential equations governing elastoplastic behavior. According to the theory of elastoplasticity, the governing equations for the inelastic models can be developed as follows.

For small deformation cases, it can be assumed that no differentiation among the various stress and strain tensors is required, and that the differential of total strain ε can be decomposed into elastic and inelastic parts:

$$d\boldsymbol{\varepsilon} = d\boldsymbol{\varepsilon}^e + d\boldsymbol{\varepsilon}^i \qquad (4.2)$$

where the differential of the elastic strain, $d\varepsilon^e$, is related to the differential stress, $d\sigma$, through a linear isotropic elasticity tensor, $\boldsymbol{E}$, as follows:

$$d\boldsymbol{\sigma} = \boldsymbol{E} : d\boldsymbol{\varepsilon}^e = [(3\lambda + 2\mu)\boldsymbol{P}^s + 2\mu\boldsymbol{P}^d] : d\boldsymbol{\varepsilon}^e$$

$$= 3B\ d\boldsymbol{\varepsilon}^{es} + 2G\ d\boldsymbol{\varepsilon}^{ed} = d\boldsymbol{\sigma}^s + d\boldsymbol{\sigma}^d \qquad (4.3)$$

where B, is the bulk modulus, and $G = \mu$, the shear modulus. The differential of the inelastic strain, $d\varepsilon^i$, is given by a flow rule

$$d\varepsilon^i = d\lambda\, M(\sigma, I_i) \qquad i = 1,2,...,n \tag{4.4}$$

where M is a unit tensor function of stress and internal variables (i.e., $M : M = 1$) that describes the direction of the differential of the inelastic strain. If N is the unit normal to the yield surface in the stress space, that is,

$$N = \frac{1}{N}\frac{\partial f}{\partial \sigma} \tag{4.5}$$

where N is the magnitude of the gradient defined by

$$N = \left(\frac{\partial f}{\partial \sigma} : \frac{\partial f}{\partial \sigma}\right)^{\frac{1}{2}} \tag{4.6}$$

then the flow rule is said to be associated (a consequence of Drucker's postulate) if

$$M = N \tag{4.7}$$

Otherwise, the flow rule is nonassociated. It has been known from experimental observations that the associated flow rule (normality rule) holds generally for metals but not for quasi-brittle materials [Vermeer and de Borst, 1984]. The parameter $d\lambda$ is larger than zero for inelastic deformations and chosen such that the inelastic consistency condition

$$df(\sigma, I_i) = 0 \tag{4.8}$$

is satisfied, which guarantees that the stress remains on the yield surface during inelastic deformations. The internal variables are determined by a suitable set of hardening rules:

$$dI_i = d\lambda h_i(\sigma, I_i) \qquad i = 1,2,...,n \tag{4.9}$$

where h_i are inelastic moduli.

The loading, neutral loading, and unloading criteria of an inelastic model may be expressed in a compact manner by

$$f \le 0, \qquad d\lambda \ge 0, \qquad d\lambda f \equiv 0 \tag{4.10}$$

If $f < 0$, then $d\lambda = 0$ and the process is elastic loading or unloading. If $d\lambda > 0$, then $f = 0$ and the process is inelastic loading. If both f and $d\lambda$ equal zero, neutral loading occurs without any inelastic deformation.

With the use of differential constitutive equations consisting of Eqs. (4.2), (4.3), (4.4), (4.8), and (4.9) together with the loading and unloading criteria defined by Eq. (4.10), the stress, elastic strain, and inelastic strain tensors can be obtained for given increments in the total strain tensor. The difference between different inelastic models depends on the specific yield surface, flow rule, and hardening rules.

4.2 Constitutive Equation Solver

Because the inelastic models are often highly nonlinear, an incremental-iterative integration scheme is required to solve the constitutive equations. This section will first give integration rules, and then address the application of the rules in two general cases: integration schemes with and without the use of the tangent stiffness tensor.

4.2.1 Integration Rules

In the analysis of nonlinear inelastic problems, the precision with which differential constitutive equations are integrated has a direct impact on the overall accuracy of the analysis. Since the differential form is approximated by incremental forms in numerical algorithms, an acceptable incremental-iterative algorithm must satisfy three basic requirements [Ortiz and Popov, 1985]: (a) consistency with the constitutive equations to be integrated, (b) numerical stability, and (c) incremental inelastic consistency condition. Requirements (a) and (b) are necessary for attaining convergence of the numerical solution as the incremental step becomes vanishingly small [Gear, 1971]. Requirement (c) is the algorithmic counterpart of the differential inelastic consistency condition, Eq. (4.8).

Two families of algorithms exist for the integration of inelastic constitutive equations: the generalized trapezoidal and midpoint rules. These two rules are acceptable in the sense of requirements (a) to (c) and commonly used in commercial codes. For the constitutive equations summarized as follows:

$$d\boldsymbol{\varepsilon} = d\boldsymbol{\varepsilon}^e + d\boldsymbol{\varepsilon}^i \tag{4.11-1}$$

$$d\boldsymbol{\sigma} = \boldsymbol{E} : d\boldsymbol{\varepsilon}^{e} \tag{4.11-2}$$

$$d\boldsymbol{\varepsilon}^{i} = d\,\lambda \boldsymbol{M}(\boldsymbol{\sigma}, I_i) \tag{4.11-3}$$

$$dI_i = d\lambda h_i(\boldsymbol{\sigma}, I_i) \tag{4.11-4}$$

$$df(\boldsymbol{\sigma}, I_i) = 0 \tag{4.11-5}$$

the trapezoidal rule generalized for integrating Eqs. (4-11) takes the form of

$$\boldsymbol{\sigma}_n = \boldsymbol{\sigma}_{n-1} + \boldsymbol{E} : \left[\left(\boldsymbol{\varepsilon}_n - \boldsymbol{\varepsilon}_{n-1} \right) - \left(\boldsymbol{\varepsilon}^{i}_n - \boldsymbol{\varepsilon}^{i}_{n-1} \right) \right] \tag{4.12-1}$$

$$\boldsymbol{\varepsilon}^{i}_n = \boldsymbol{\varepsilon}^{i}_{n-1} + \Delta\lambda \left[(1-\alpha)\boldsymbol{M}_{n-1} + \alpha \boldsymbol{M}_n \right] \tag{4.12-2}$$

$$\left(I_i\right)_n = \left(I_i\right)_{n-1} + \Delta\lambda \left[(1-\alpha)\left(h_i\right)_{n-1} + \alpha \left(h_i\right)_n \right] \tag{4.12-3}$$

$$f_n = 0 \tag{4.12-4}$$

where

$$\boldsymbol{M}_{n-1} = \boldsymbol{M}[\boldsymbol{\sigma}_{n-1}, (I_i)_{n-1}] \tag{4.13-1}$$

$$\boldsymbol{M}_n = \boldsymbol{M}[\boldsymbol{\sigma}_n, (I_i)_n] \tag{4.13-2}$$

$$(h_i)_{n-1} = h_i[\,\boldsymbol{\sigma}_{n-1}, (I_i)_{n-1}] \tag{4.13-3}$$

$$(h_i)_n = h_i[\boldsymbol{\sigma}_n, (I_i)_n] \tag{4.13-4}$$

The numerical values of $\boldsymbol{\varepsilon}_{n-1}, \boldsymbol{\varepsilon}^{i}_{n-1}, \boldsymbol{\sigma}_{n-1}$, and $\left(I_i\right)_{n-1}$ are known at the previous time, t_{n-1}, whereas $\boldsymbol{\varepsilon}^{i}_n, \boldsymbol{\sigma}_n$, and $\left(I_i\right)_n$, need to be solved for the updated total strains $\boldsymbol{\varepsilon}_n$ that are given at the beginning of the current time, $t_n = t_{n-1} + \Delta t$, with Δt being the time step. The incremental inelastic parameter, $\Delta\lambda$, is determined by the use of the incremental inelastic consistency condition: $f_n - f_{n-1} = 0$, which results from Eq. (4.12-4). The trapezoidal rule is explicit for $\alpha = 0$, and implicit for $0 < \alpha \leq 1$. The geometric interpretation of the algorithm can be made clear by combining Eqs. (4.12-1) and (4.12-2) into

$$\boldsymbol{\sigma}_n = \boldsymbol{\sigma}^{*}_n - \Delta\lambda(1-\alpha)\boldsymbol{E} : \boldsymbol{M}_{n-1} - \Delta\lambda\ \alpha \boldsymbol{E} : \boldsymbol{M}_n \tag{4.14}$$

where

$$\boldsymbol{\sigma}^{*}_n = \boldsymbol{\sigma}_{n-1} + \boldsymbol{E} : \left(\boldsymbol{\varepsilon}_n - \boldsymbol{\varepsilon}_{n-1} \right) \tag{4.15}$$

represents the elastic prediction for the updated stress. The final state of stress is obtained by mapping the elastically predicted stress onto an updated yield surface through two tensorial subtractions along the initial flow direction M_{n-1} and the final flow direction M_n.

As an alternative family of algorithms, the generalized midpoint rule is given by

$$\sigma_n = \sigma_{n-1} + E:\left[\left(\varepsilon_n - \varepsilon_{n-1}\right) - \left(\varepsilon_n^i - \varepsilon_{n-1}^i\right)\right] \tag{4.16-1}$$

$$\varepsilon_n^i = \varepsilon_{n-1}^i + \Delta\lambda M_{n+\alpha} \tag{4.16-2}$$

$$(I_i)_n = (I_i)_{n-1} + \Delta\lambda (h_i)_{n+\alpha} \tag{4.16-3}$$

$$f_n = 0 \tag{4.16-4}$$

where

$$M_{n+\alpha} = M[(1-\alpha)\,\sigma_{n-1} + \alpha\,\sigma_n,\ (1-\alpha)(I_i)_{n-1} + \alpha(I_i)_n] \tag{4.17-1}$$

$$(h_i)_{n+\alpha} = h_i[(1-\alpha)\,\sigma_{n-1} + \alpha\,\sigma_n,\ (1-\alpha)(I_i)_{n-1} + \alpha(I_i)_n] \tag{4.17-2}$$

As in the case of the generalized trapezoidal rule, this algorithm is explicit for $\alpha = 0$ and implicit for $0 < \alpha \le 1$. The unknowns $\varepsilon_n^i, \sigma_n$, $(I_i)_n$, and $\Delta\lambda$ are solved through Eqs. (4.16) to (4.17) for the updated total strains ε_n. The geometric interpretation of the midpoint rule can also be seen by combining Eqs. (4.16-1) and (4.16-2) into

$$\sigma_n = \sigma_n^* - \Delta\lambda\, E: M_{n+\alpha} \tag{4.18}$$

Both the generalized trapezoidal and midpoint rules are applicable to associated or nonassociated inelastic models described by Eqs. (4.11) and include well-known integration schemes as particular cases such as the radial return, mean normal, and closest point schemes. Ortiz and Popov [1985] have shown that these two rules satisfy the incremental inelastic consistency, are consistent with the constitutive equations to be integrated (first-order accurate) for α ranging from 0 to 1, and are second-order accurate if $\alpha = \frac{1}{2}$ in the linear case. The trapezoidal rule is unconditionally stable for $\alpha \ge \alpha_c$ where α_c varies from a value of $\frac{1}{2}$ for a surface of constant curvature such as the von Mises surface, to a value of 1 for surfaces with corners. Hence, the stability of the trapezoidal rule is very sensitive to the degree of distortion of the yield surface. On the other hand, the midpoint rule is unconditionally stable for all surfaces if $\alpha \ge \frac{1}{2}$. Thus, it appears that the

midpoint rule is a better choice for numerical integration than the trapezoidal rule, although these two rules coincide for the particular case of the associated von Mises model.

In order to solve a static problem with a direct method or a dynamic problem with an implicit time integrator [Belytschko, 1983; Hughes, 1983], an inelastic structural stiffness matrix often needs to be formulated based on an inelastic stiffness tensor. From the differential form of the constitutive equations, it is a natural approach to construct an inelastic tangent stiffness tensor instead of a secant tensor. As a result, the structural tangent stiffness matrix becomes singular at limit or bifurcation points, which will be explored further in Chapter 7. If an explicit time integrator [Belytschko, 1983; Hughes, 1983] is used for a dynamic problem or the dynamic relaxation method [Underwood, 1983] is employed for a static problem, there is no need to invoke a stiffness tensor and the constitutive equations can be solved directly by the use of either the trapezoidal or the midpoint rule. Although the explicit time integrator is preferred in large scale computation because of the cost in forming a stiffness matrix, the theoretical insight from the stiffness matrix might be lost and the time step must be chosen according to certain stability criterion. Next, the integration schemes with and without the formation of stiffness tensor are discussed for solving the inelastic constitutive equations and for providing the basis necessary to understand the literature on the subject.

4.2.2 Algorithms with Tangent Stiffness Tensor

The tangent stiffness tensor $\boldsymbol{T}$ is defined such that differentials of stress and total strain are related through

$$d\boldsymbol{\sigma} = \boldsymbol{T} : d\boldsymbol{\varepsilon} \tag{4.19}$$

while the secant stiffness tensor $\boldsymbol{S}$ relates total strain to stress through

$$\boldsymbol{\sigma} = \boldsymbol{S} : \boldsymbol{\varepsilon} \tag{4.20}$$

The inelastic tangent stiffness tensor can be derived based on differential governing equations, (4.11), as shown below. However, this is not the case for the secant stiffness tensor when using the classical approach of elastoplasticity.

In order to obtain an explicit expression for the tangent stiffness tensor, consider first the consistency condition:

$$df(\sigma, I_i) = \frac{\partial f}{\partial \sigma} d\sigma + \sum_{i=1}^{n} \frac{\partial f}{\partial I_i} dI_i = 0 \tag{4.21}$$

With the use of Eqs. (4.5) and (4.11-4), an alternative form of the consistency condition is

$$df(\sigma, I_i) = NN : d\sigma + d\lambda \sum_{i=1}^{n} h_i \frac{\partial f}{\partial I_i} = 0 \tag{4.22}$$

From the first three equations of (4.11), it follows that

$$d\sigma = E : (d\varepsilon - d\lambda M) \tag{4.23}$$

An inner product of Eq. (4.23) with NN yields

$$NN : d\sigma = NN : E : d\varepsilon - d\lambda NN : E : M \tag{4.24}$$

If the term $NN : d\sigma$ is eliminated between Eqs. (4.22) and (4.24), the resulting equation gives the following expression for $d\lambda$:

$$d\lambda = \frac{N : E : d\varepsilon}{N : E : M - \sum_{i=1}^{n} \frac{h_i}{N} \frac{\partial f}{\partial I_i}} \tag{4.25}$$

The substitution of Eq. (4.25) into Eq. (4.23) and factoring out the term $d\varepsilon$ yields the tangent stiffness tensor

$$T = E - \frac{E : M \otimes N : E}{N : E : M - \sum_{i=1}^{n} \frac{h_i}{N} \frac{\partial f}{\partial I_i}} \tag{4.26}$$

The specific form of Eq. (4.26) for an inelastic model can be written as soon as N, M, h_i and $\frac{\partial f}{\partial I_i}$ are given. It can be observed that

1. If the flow rule is associated, then $N = M$ and T retain the same symmetry properties as E.
2. If the denominator of the last term in Eq. (4.26) is infinite, the tangent stiffness tensor is equal to the elasticity tensor.

3. If the denominator is small enough, there is a possibility that $\boldsymbol{T}$ will be singular and the structural tangent stiffness matrix will be ill-conditioned.

Nonlinear features of engineering materials can be analyzed with the use of $\boldsymbol{T}$. A failure limit point in stress space is characterized by the condition that

$$\boldsymbol{T}:d\boldsymbol{\varepsilon}=0 \tag{4.27}$$

for nonzero $d\boldsymbol{\varepsilon}$ if $\boldsymbol{T}$ is symmetric. The collection of all such points constitutes a failure limit surface in stress space. If $\boldsymbol{T}$ is not symmetric, a bifurcation point is identified by the condition in Eq. (4.27), and the failure limit point is obtained by using the symmetric part of $\boldsymbol{T}$ in Eq. (4.27). A bifurcation point is defined to be a point on the solution path where the governing equation admits more than one solution. The bifurcation point can occur before or after the failure limit point is reached. Structural failure problems, such as buckling and failure zones, can be attributed to the existence of critical points (i.e., limit and bifurcation points). For the inelastic tangent stiffness tensor given by Eq. (4.26), the term $\sum_{i=1}^{n}\frac{h_i}{N}\frac{\partial f}{\partial I_i}$ plays a very important role in determining critical points. In order to illustrate this, suppose $\boldsymbol{T}$ is symmetric and $d\boldsymbol{\varepsilon}$ is proportional to $\boldsymbol{N}$. Then

$$\boldsymbol{T}:\boldsymbol{N}=\boldsymbol{E}:\boldsymbol{N}-\frac{\boldsymbol{E}:\boldsymbol{N}\,(\boldsymbol{N}:\boldsymbol{E}:\boldsymbol{N})}{\boldsymbol{N}:\boldsymbol{E}:\boldsymbol{N}-\sum_{i=1}^{n}\frac{h_i}{N}\frac{\partial f}{\partial I_i}}$$

$$=\frac{-\sum_{i=1}^{n}\frac{h_i}{N}\frac{\partial f}{\partial I_i}}{\boldsymbol{N}:\boldsymbol{E}:\boldsymbol{N}-\sum_{i=1}^{n}\frac{h_i}{N}\frac{\partial f}{\partial I_i}}\boldsymbol{E}:\boldsymbol{N} \tag{4.28}$$

Since $\boldsymbol{E}$ is a positive definite tensor, $\boldsymbol{N}:\boldsymbol{E}:\boldsymbol{N}>0$ for $\boldsymbol{N}\neq 0$, and a limit point exists if the term $\sum_{i=1}^{n}\frac{h_i}{N}\frac{\partial f}{\partial I_i}=0$. As can be seen, where a limit point will appear depends on the functional forms of f and h_i.

In order to reflect explicitly the loading/unloading criteria of an inelastic model in a computational code, the tangent stiffness tensor given by Eq. (4.26) is usually written as

$$\boldsymbol{T}(\boldsymbol{\sigma},I_i)=\boldsymbol{E}-H[f]\frac{\boldsymbol{E}:\boldsymbol{M}\otimes\boldsymbol{N}:\boldsymbol{E}}{A+B} \tag{4.29}$$

where $H[\ ]$ denotes the Heaviside function and the notations

$$A = N : E : M \tag{4.30-1}$$

$$B = -\sum_{i=1}^{n} \frac{h_i}{N} \frac{\partial f}{\partial I_i} \tag{4.30-2}$$

have been introduced for convenience. If $f < 0$, $T = E$. Otherwise, the tangent stiffness tensor includes both elastic and inelastic effects.

Because T is generally a nonlinear function of σ and I_i, an incremental-iterative integration scheme is required to find the corresponding stress increments and internal variables for given total strain increments. To be efficient, for each increment the current T should be formulated at the end of the iteration loop instead of at each iteration, and then the structural stiffness matrix can be updated based on the current stiffness tensor T. Because of the nonlinearity of the general structural stiffness matrix, another incremental-iterative integration scheme is needed to solve the unknown incremental displacement vector, which in turn gives the total strain increment. Therefore, for nonlinear analyses using the displacement-based finite element method [Bathe, 1982], two incremental-iterative integration loops are needed: one in the stress-strain space and the other in the load-displacement space. Although the integration scheme in any space should satisfy consistency and stability requirements to achieve convergence, there exist some different numerical issues in these two different spaces. For example, singularity or bifurcation problems may occur in the load-displacement space but not in the stress-strain space, and vice versa. The overall accuracy of nonlinear structural analyses depends not only on the unique characteristics of each space but also on the relation between two spaces. Hence, the knowledge of the features of solution schemes used in both spaces is essential for large scale computation. Recently, active research has been conducted toward reviewing and developing solution procedures for nonlinear structural analyses, especially for failure simulation characterized by bifurcation and limit points [Chen and Schreyer, 1989 and 1990]. In this report, no attempt will be made to explore the integration scheme used in the load-displacement space, and instead, two incremental-iterative schemes will be discussed in Subsection 4.2.3 for integrating the differential stress-strain relation. For special cases such as small increments in the total strain or linear inelastic models, however, there are two single-step integration methods without iteration, which, based on the trapezoidal rule, replace the differential form of Eq. (4.19) by the following incremental form within a time step Δt

$$\Delta\sigma = \int_{t-\Delta t}^{t} T : d\varepsilon = [(1-\alpha)T_{t-\Delta t} + \alpha T_t] : \Delta\varepsilon \tag{4.31}$$

where α ranges from 0 to 1 . An Euler forward method is obtained for $\alpha = 0$, while an Euler backward method takes $\alpha = 1$. It should be noted that T_t is unknown in advance if T is not constant.

The single-step Euler forward method is very simple and fairly accurate for linear models; however, very small increments in the total strain should be prescribed for nonlinear models in order to keep numerical errors small. Overshooting also exists, which is caused by transitions of the stiffness tensor between two different regimes, such as from elastic to hardening regimes. The following is an outline of the Euler forward method.

Algorithm 1.

For each increment Δt , the states of stress, total strain, elastic strain, inelastic strain, and internal variables at the end of the previous increment are known and denoted as $\sigma_{n-1}, \varepsilon_{n-1}, \varepsilon^e_{n-1}, \varepsilon^i_{n-1}$, and $(I_i)_{n-1}$, respectively, and the current increment in the total strain, $\Delta\varepsilon$, is prescribed.

Step 1

Assume in the predictor phase that the step is elastically loading or unloading, and calculate the stress increment $\Delta\sigma$ through the elasticity tensor:

$$\Delta\varepsilon^e = \Delta\varepsilon$$
$$\Delta\varepsilon^i = 0$$
$$\Delta\sigma = E:\Delta\varepsilon^e$$

Step 2

Evaluate the yield surface, $f\left[\sigma^t, (I_i)_{n-1}\right]$, with the test stress

$$\sigma^t = \sigma_{n-1} + \Delta\sigma$$

where σ_{n-1} and $(I_i)_{n-1}$ are known from the previous increment.

Step 3

Check the yield criterion:

If $f\left[\sigma^t, (I_i)_{n-1}\right] < 0$, then the solution is elastic. Go to Step 5. Otherwise, the inelastic regime has been reached.

Step 4

In this inelastic corrector phase, calculate the inelastic solution through the inelastic tangent stiffness tensor:

$$\Delta\boldsymbol{\sigma} = \boldsymbol{T}_{n-1} : \Delta\boldsymbol{\varepsilon}$$
$$\Delta\boldsymbol{\varepsilon}^e = \boldsymbol{E}^{-1} : \Delta\boldsymbol{\sigma}$$
$$\Delta\boldsymbol{\varepsilon}^i = \Delta\boldsymbol{\varepsilon} - \Delta\boldsymbol{\varepsilon}^e$$

Step 5

Update variables at the end of the increment:

$$\boldsymbol{\sigma}_n = \boldsymbol{\sigma}_{n-1} + \Delta\boldsymbol{\sigma}$$
$$\boldsymbol{\varepsilon}_n = \boldsymbol{\varepsilon}_{n-1} + \Delta\boldsymbol{\varepsilon}$$
$$\boldsymbol{\varepsilon}_n^e = \boldsymbol{\varepsilon}_{n-1}^e + \Delta\boldsymbol{\varepsilon}^e$$
$$\boldsymbol{\varepsilon}_n^i = \boldsymbol{\varepsilon}_{n-1}^i + \Delta\boldsymbol{\varepsilon}^i$$

and

$$(I_i)_n = (I_i)_{n-1} + \Delta I_i = (I_i)_{n-1} + \Delta\lambda (h_i)_{n-1}$$

where

$$\Delta\lambda = H[f] \frac{(\boldsymbol{N} : \boldsymbol{E})_{n-1}}{A + B} : \Delta\boldsymbol{\varepsilon}$$
$$A = (\boldsymbol{N} : \boldsymbol{E} : \boldsymbol{M})_{n-1}$$
$$B = -\left(\sum_{i=1}^{n} \frac{h_i}{N} \frac{\partial f}{\partial I_i} \right)_{n-1}$$

Step 6

Evaluate the current tangent stiffness tensor

$$\boldsymbol{T}_n = \boldsymbol{E} - H[f] \left(\frac{\boldsymbol{E} : \boldsymbol{M} \otimes \boldsymbol{N} : \boldsymbol{E}}{A + B} \right)_n$$

that will be used in the next increment. The current tangent stiffness matrix construction is based on $\boldsymbol{T}_n$.

Exit or go to Step 1 for the next increment. #

Another single-step integration scheme, which can be conceived as a mixed Euler forward/backward method, is derived as follows. According to the definition of the yield surface, Eq. (4.1), the Taylor series of f around the previous state $(\boldsymbol{\sigma}, I_i)_{n-1}$ is given by

$$f_n = f_{n-1} + \left(\frac{\partial f}{\partial \boldsymbol{\sigma}}\right)_{n-1} : \Delta\boldsymbol{\sigma} + \sum_i \left(\frac{\partial f}{\partial I_i}\right)_{n-1} \Delta I_i + \text{higher order terms} \qquad (4.32)$$

If f is linear in the principal stress and internal variable spaces, and M and h_i are constant, it follows that the higher order terms in Eq. (4.32) vanish and

$$\Delta\boldsymbol{\varepsilon}^i = \Delta\lambda M \qquad (4.33\text{-}1)$$
$$\Delta I_i = \Delta\lambda h_i \qquad (4.33\text{-}2)$$

By putting $f_n = 0$, the errors from transitions between two different regimes and other sources are not carried along and a rigorous return to the yield surface is guaranteed. Thus, from Eqs. (4.5), (4.32), and (4.33), we arrive at

$$f_{n-1} + NN : \Delta\boldsymbol{\sigma} + \Delta\lambda \sum_i \frac{\partial f}{\partial I_i} h_i = 0 \qquad (4.34)$$

in which the subscript $n - 1$ has been dropped except for f_{n-1}, because of the assumption of linearity. If nonlinear models are considered, it should be kept in mind that all the terms in Eq. (4.34) are evaluated at the previous state, and therefore the truncated Taylor series will incur numerical errors. Since

$$\Delta\boldsymbol{\sigma} = \boldsymbol{\sigma}_n - \boldsymbol{\sigma}_{n-1} = E : (\Delta\boldsymbol{\varepsilon} - \Delta\lambda M) \qquad (4.35)$$

an inner product of Eq. (4.35) with NN and a substitution of the result into Eq. (4.34) yields

$$\Delta\lambda = \frac{\frac{f_{n-1}}{N} + N : E : \Delta\boldsymbol{\varepsilon}}{A + B} \qquad (4.36)$$

where A and B are defined by Eq. (4.30). For the test stress computed in the elastic predictor phase,

$$\boldsymbol{\sigma}^t = \boldsymbol{\sigma}_{n-1} + E : \Delta\boldsymbol{\varepsilon} \qquad (4.37)$$

a correction must be applied to make the final stress $\boldsymbol{\sigma}_n$ remain on the yield surface if $\boldsymbol{\sigma}^t$ appears to lie outside the yield surface. To do so, we can combine Eqs. (4.37) and (4.35)

together and delete the term σ_{n-1} . With the use of Eq. (4.36), the final stress can be found through

$$\sigma_n = \sigma^t - \frac{\frac{f_{n-1}}{N} + N:E:\Delta\varepsilon}{A+B} E:M \tag{4.38}$$

The current increments in the inelastic strain and internal variables can then be obtained. The following is an outline of the corresponding algorithm, which offers a rigorous return to the yield surface for linear models and produces fewer errors than Algorithm 1 for nonlinear models although a few more calculations are needed.

Algorithm 2.

For each increment Δt , the states of stress, total strain, elastic strain, inelastic strain, and internal variables at the end of the previous increment are known and denoted as $\sigma_{n-1}, \varepsilon_{n-1}, \varepsilon^e_{n-1}, \varepsilon^i_{n-1}$, and $(I_i)_{n-1}$, respectively, and the current increment in the total strain, $\Delta\varepsilon$, is prescribed.

Step 1

Assume in the predictor phase that the step is elastically loading or unloading, and calculate the test stress σ^t through the elasticity tensor:

$$\Delta\varepsilon^e = \Delta\varepsilon$$
$$\Delta\varepsilon^i = 0$$
$$\sigma^t = \sigma_{n-1} + E:\Delta\varepsilon$$

Step 2

Evaluate the yield surface, $f\left[\sigma^t, (I_i)_{n-1}\right]$, with the test stress σ^t and internal variables $(I_i)_{n-1}$.

Step 3

Check the yield criterion:

If $f\left[\sigma^t, (I_i)_{n-1}\right] < 0$, then the solution is elastic, $\sigma_n = \sigma^t$. Go to Step 5.

Otherwise, the inelastic regime has been reached.

Step 4

In this inelastic corrector phase, calculate the inelastic solution as follows:

$$\Delta\lambda = \left(\frac{\frac{f}{N} + N:E}{A+B} \right)_{n-1} :\Delta\varepsilon$$

$$\sigma_n = \sigma^t - \Delta\lambda E : M_{n-1}$$
$$\Delta\varepsilon^i = \Delta\lambda M_{n-1}$$
$$\Delta\varepsilon^e = \Delta\varepsilon - \Delta\varepsilon^i$$

Step 5

Update variables at the end of the increment:

$$\varepsilon_n = \varepsilon_{n-1} + \Delta\varepsilon$$
$$\varepsilon_n^e = \varepsilon_{n-1}^e + \Delta\varepsilon^e$$
$$\varepsilon_n^i = \varepsilon_{n-1}^i + \Delta\varepsilon^i$$
$$(I_i)_n = (I_i)_{n-1} + \Delta I_i$$

Step 6

Find $N_n : E, E : M_n$, $A = (N : E : M)_n$ and $B = \left(-\sum_{i=1}^{n} \frac{h_i}{N} \frac{\partial f}{\partial I_i} \right)_n$ for formulating the current tangent stiffness matrix and $\Delta\lambda$ in the next increment, which can be omitted if no changes occur in these variables.

Exit or go to Step 1 for the next increment. #

The two single-step algorithms discussed above are robust for the case where a stiffness tensor has to be formed. Algorithm 2 is much more accurate than Algorithm 1 because of the self-correcting feature of Eq. (4.34). Algorithm 1 uses the tangent stiffness tensor in Step 4, but Algorithm 2 does not require explicitly the use of the stiffness tensor. If a given inelastic model is highly nonlinear, however, it is recommended to use the incremental-iterative integration schemes given in the next subsection. The current tangent stiffness tensor T_n is constructed at the end of the iteration loop if it is required to formulate a stiffness matrix in a structural solution scheme.

4.2.3 Algorithms without Tangent Stiffness Tensor

If an explicit time integrator is adopted to obtain numerical solutions to the dynamic field equations or the dynamic relaxation method is employed for a static problem, there is no need to obtain a tangent stiffness tensor and the differential constitutive equations can be solved directly by using either the generalized trapezoidal or the midpoint rule. One such method is the incremental-iterative approach outlined in Algorithm 3, given later, where the choice of the trapezoidal or midpoint rule can be made. As stated in Subsection 4.2.1, the

incremental inelastic parameter, $\Delta\lambda$, is determined by the equation, $f = 0$, which requires the inelastic consistency condition. If f is nonlinear, the Newton-Raphson method or its further approximation, the secant method [Atkinson, 1978; Bathe, 1982], can be utilized to find the root λ for $f = f(\boldsymbol{\sigma}, I_i) = \bar{f}(\boldsymbol{\sigma}, \lambda) = 0$ and then the increment $\Delta\lambda$ can be solved with respect to the previous state. With the subscript j denoting the iteration loop, the Newton-Raphson method takes the form of

$$\lambda_{j+1} = \lambda_j - \frac{f_j}{\left(\frac{\partial f}{\partial \lambda}\right)_j} \qquad j \geq 0 \tag{4.39}$$

where

$$\left(\frac{\partial f}{\partial \lambda}\right)_j = \sum_i \left(\frac{\partial f}{\partial I_i} h_i\right)_j \tag{4.40}$$

Numerically, Eq. (4.40) is often approximated with

$$\left(\frac{\partial f}{\partial \lambda}\right)_j \approx \frac{f_j - f_{j-1}}{\lambda_j - \lambda_{j-1}} \qquad j \geq 1 \tag{4.41}$$

Substitution of Eq. (4.41) into Eq. (4.39) results in the secant method

$$\lambda_{j+1} = \lambda_j - f_j \frac{\lambda_j - \lambda_{j-1}}{f_j - f_{j-1}} \qquad j \geq 1 \tag{4.42}$$

Algorithm 3 is unconditionally stable provided $\alpha \geq \alpha_c$, where α_c depends on the integration rule and the yield surface. But the initial guess for λ, which relies on the prescribed total strain increment, must be within the region of convergence of the iterative Newton-Raphson or secant method.

Usually, $\Delta\lambda$ is solved without iteration, since it may not be necessary to obtain an exact value for $\Delta\lambda$ at each iteration step of the iteration loop for solving constitutive equations for a given increment in the total strain. As a result of a one-step Newton-Raphson method, Algorithm 4 shows an alternative approach called the cutting plane method, which is often more efficient than Algorithm 3. In effect, the approach is an automatic subincrementing procedure because the one-step Newton-Raphson method produces a subincrement in λ, $\delta\lambda_k = \lambda_k - \lambda_{k-1}$, with the subscript k being the iteration

index for solving constitutive equations and δ denoting here the subincrement of a variable. The total increment in λ is then given by $\Delta\lambda = \sum_k \delta\lambda_k$. The method is simple and explicit, but it is conditionally stable. Special care must be taken for regions of the yield surface where the radius of curvature is small.

The following are the outlines of Algorithms 3 and 4. The prescribed total strain increment is assumed to be reasonably small because of the use of the Newton-Raphson or secant method in finding $\Delta\lambda$. If resulting numerical solutions appear to diverge, it is often a good practice to bisect the original total strain increment and try again.

Algorithm 3.

For each increment Δt , the states of stress, total strain, elastic strain, inelastic strain, and internal variables at the end of previous increment are known and denoted as $\sigma_{n-1}, \varepsilon_{n-1}, \varepsilon^e_{n-1}, \varepsilon^i_{n-1}$, and $(I_i)_{n-1}$, respectively, and the current total strain ε_n is prescribed. The iteration loop for solving the constitutive equation starts with the index $k = 0$. Let $\sigma_k, \varepsilon^i_k$, and $(I_i)_k$ be the current iterative estimates for $\sigma_n, \varepsilon^i_n$, and $(I_i)_n$, respectively. A small positive tolerance parameter, *tol* , is used to ensure the convergence of numerical solutions. The parameter, α , ranging from *0* to *1*, identifies the algorithm according to the definition of the trapezoidal or midpoint rule.

Step 1

If $k = 0$, then

$$\varepsilon^i_k = \varepsilon^i_{n-1}$$
$$(I_i)_k = (I_i)_{n-1}$$

For $k \geq 0$, calculate the stress σ_k through the elasticity tensor $\boldsymbol{E}$:

$$\sigma_k = \boldsymbol{E} : (\varepsilon_n - \varepsilon^i_k)$$

Step 2

Evaluate the yield surface $f_k = f\left[\sigma_k, (I_i)_k\right]$ and check the yield criterion:

If $f_0 > tol$, or $|f_k| > tol$ for $k \geq 1$, then go to Step 3. Otherwise, the solution is converged; update the following variables:

$$\sigma_n = \sigma_k$$
$$(I_i)_n = (I_i)_k$$
$$\varepsilon_n^i = \varepsilon_k^i$$
$$\varepsilon_n^e = \varepsilon_n - \varepsilon_n^i$$

Exit or go to Step 1 for the next increment.

Step 3

To implement the trapezoidal rule, go to Step 4; to implement the midpoint rule, go to Step 5.

Step 4

$$(h_i)_k^c = (1-\alpha)h_i\left[\sigma_{n-1}, (I_i)_{n-1}\right] + \alpha h_i\left[\sigma_k, (I_i)_k\right]$$
$$M_k^c = (1-\alpha)M\left[\sigma_{n-1}, (I_i)_{n-1}\right] + \alpha M\left[\sigma_k, (I_i)_k\right]$$

Go to Step 6.

Step 5

$$(h_i)_k^c = h_i\left[(1-\alpha)\sigma_{n-1} + \alpha\sigma_k, (1-\alpha)(I_i)_{n-1} + \alpha(I_i)_k\right]$$
$$M_k^c = M\left[(1-\alpha)\sigma_{n-1} + \alpha\sigma_k, (1-\alpha)(I_i)_{n-1} + \alpha(I_i)_k\right]$$

Step 6

Solve $f\left[\sigma_k, (I_i)_k\right] = 0$ for λ_k by using either the Newton-Raphson or secant method (iterative or one-step), and let $\Delta\lambda_k = \lambda_k - \lambda_{n-1}$.

Step 7

$$(I_i)_{k+1} = (I_i)_{n-1} + \Delta\lambda_k (h_i)_k^c$$
$$\varepsilon_{k+1}^i = \varepsilon_{n-1}^i + \Delta\lambda_k M_k^c$$

Advance the subscript: $k = k + 1$, and go to Step 1. #

Algorithm 4.

For each increment Δt, the states of stress, total strain, elastic strain, inelastic strain, and internal variables at the end of previous increment are known and denoted as $\sigma_{n-1}, \varepsilon_{n-1}, \varepsilon_{n-1}^e, \varepsilon_{n-1}^i$, and $(I_i)_{n-1}$, respectively, and the current total strain ε_n is

prescribed. The iteration loop for solving the constitutive equation starts with the index $k = 0$. Let $\sigma_k, \varepsilon_k^i$,and $(I_i)_k$ be the current iterative estimates for $\sigma_n, \varepsilon_n^i$, and $(I_i)_n$, respectively. A small positive tolerance parameter, *tol* , is used to ensure the convergence of numerical solutions.

Step 1

If $k = 0$, then

$$\varepsilon_k^i = \varepsilon_{n-1}^i$$
$$(I_i)_k = (I_i)_{n-1}$$

For $k \geq 0$, calculate the stress σ_k through the elasticity tensor E :

$$\sigma_k = E : \left(\varepsilon_n - \varepsilon_k^i\right)$$

Step 2

Evaluate the yield surface $f_k = f\left[\sigma_k, (I_i)_k\right]$ and check the yield criterion:

If $f_0 > tol$, or $|f_k| > tol$ for $k \geq 1$, then go to Step 3. Otherwise, the solution is converged; update the following variables:

$$\sigma_n = \sigma_k$$
$$(I_i)_n = (I_i)_k$$
$$\varepsilon_n^i = \varepsilon_k^i$$
$$\varepsilon_n^e = \varepsilon_n - \varepsilon_n^i$$

Exit or go to Step 1 for the next increment.

Step 3

Calculate the subincrement $\delta\lambda_k$ by using the Newton-Raphson method:

$$\left(\frac{\partial f}{\partial \lambda}\right)_k = \left(\frac{\partial f}{\partial I_i} h_i\right)_k$$
$$\delta\lambda_k = -\frac{f_k}{\left(\frac{\partial f}{\partial \lambda}\right)_k}$$

where $\delta\lambda_k = \lambda_{k+1} - \lambda_k$ with $\lambda_0 = \lambda_{n-1}$. For $k > 0$ and $\lambda_{n-1} > 0$, or $k > 1$ and

$\lambda_{n-1} = 0$. The secant method can be used instead of the Newton-Raphson method, as follows:

$$\delta\lambda_k = -f_k \frac{\lambda_k - \lambda_{k-1}}{f_k - f_{k-1}}$$

Step 4

$$(h_i)_k = h_i\left[\boldsymbol{\sigma}_k, (I_i)_k\right]$$
$$\boldsymbol{M}_k = \boldsymbol{M}\left[\boldsymbol{\sigma}_k, (I_i)_k\right]$$

Step 5

$$(I_i)_{k+1} = (I_i)_k + \delta\lambda_k h_k$$
$$\boldsymbol{\varepsilon}^i_{k+1} = \boldsymbol{\varepsilon}^i_k + \delta\lambda_k \boldsymbol{M}_k$$

Advance the subscript: $k = k + 1$, and go to Step 1. #

In summary, this chapter discusses the general formulation of inelastic models based on the framework of classical elastoplasticity, which is given in terms of differential forms by Eqs. (4.11-1) to (4.11-5). A specific model can be established as long as the specific yield surface, flow rule, and hardening rules are defined. In order to solve differential constitutive equations, the generalized trapezoidal and midpoint rules are provided as a basis for designing algorithms. Algorithms 1 and 2 are robust and quite accurate for the case where both a linear model is used and a stiffness tensor is required. For other cases, Algorithms 3 and 4 are recommended, and a stiffness tensor can be constructed for updated values of $\boldsymbol{N}, \boldsymbol{M}, h_i$, and $\frac{\partial f}{\partial I_i}$ at the end of the iteration loop, if the tensor is needed.

In the next two chapters, various models ranging from the category of elastic-perfect plasticity to that of elastic-strain hardening plasticity are investigated with emphasis on their applicability to concrete. The yield surface, flow rule, and hardening rules are defined for each model, and the expressions of $\boldsymbol{N}:\boldsymbol{E}, \boldsymbol{E}:\boldsymbol{M}, \boldsymbol{N}:\boldsymbol{E}:\boldsymbol{M}$, and $\frac{\partial f}{\partial I_i}$ are given if it is efficient to construct a tangent stiffness tensor in structural analysis.

5. ELASTIC-PERFECTLY PLASTIC MODELS

The elastic-perfect plasticity models are the simplest category among many in classical plasticity, and still commonly employed in design codes, especially for the limit design of metal structures and some simple structures made of quasi-brittle materials. Other categories of elastoplastic models, with more features and the increased degree of complexity, are developed from this starting point. The basic assumption of elastic-perfectly plasticity is that the material behaves elastically until the limit surface is reached (i.e., the elastic surface coincides with the limit surface). Then the yield surface remains fixed during continued deformation. Hence, the yield surface and flow rule are assumed to be functions of stress only, and no hardening rules are needed. The assumption of isotropy is also invoked.

5.1 von Mises Model

One of the simplest elastic-perfectly plastic models is the associated von Mises model defined by

$$f(\boldsymbol{\sigma}) = 3J_2 - H^2 \tag{5.1-1}$$

$$M(\boldsymbol{\sigma}) = N(\boldsymbol{\sigma}) \tag{5.1-2}$$

where the second invariant of the deviatoric stress tensor, J_2, is given by

$$J_2 = \frac{1}{2}\boldsymbol{\sigma}^d : \boldsymbol{\sigma}^d \tag{5.2}$$

and the coefficient 3 is chosen so that $\sqrt{3J_2} = \sigma$, the value of the stress for uniaxial stress problems. H is a material constant to be determined from experiments. As can be seen from Eqs. (5.1-1) and (5.2), H is equal to the uniaxial peak strength, where no difference is made between uniaxial compression and tension. In fact, this model assumes that yielding begins when the distortional energy reaches a value that equals the distortional energy at yield in the uniaxial stress state. On the deviatoric (octahedral or pi-) plane, the yield surface described by $f = 0$ is a circle. From definitions (5.1) to (5.2), it follows that

$$\frac{\partial f}{\partial \boldsymbol{\sigma}} = 3\boldsymbol{\sigma}^d \tag{5.3-1}$$

$$N = \frac{1}{N}\frac{\partial f}{\partial \sigma} = \frac{\sigma^d}{\left(\sigma^d : \sigma^d\right)^{\frac{1}{2}}} \tag{5.3-2}$$

$$N : E = E : M = \frac{\sigma^d}{\left(\sigma^d : \sigma^d\right)^{\frac{1}{2}}} : \left(3BP^s + 2GP^d\right) = \frac{2G\sigma^d}{\left(\sigma^d : \sigma^d\right)^{\frac{1}{2}}} \tag{5.3-3}$$

$$N : E : M = 2G \tag{5.3-4}$$

Stress-strain curves for triaxial compression obtained with this model are shown in Figure 5-1, with typical values assigned for material constants where $H = f_c$ is adopted so that the theory predicts the failure strength, f_c, in uniaxial compression. Since the von Mises model is formulated in the deviatoric space as can be observed from Eqs. (5.1), (5.2), and (5.3), no information in the spherical space can be determined because of the independence of two spaces. Thus, the model displays no enhancement in strength with an increase in mean pressure, no yielding under the state of hydrostatic stress, and no volumetric inelastic deformation for any state of stress because

$$P^s : d\varepsilon^i = d\lambda P^s : M = d\lambda \frac{P^s : \sigma^d}{\left(\sigma^d : \sigma^d\right)^{\frac{1}{2}}} = 0 \tag{5.4}$$

In addition, no shear enhanced compaction, no dilatation, and no difference between tension and compression can be simulated. Hence, the model is of limited usefulness for geotechnical materials, although it is very simple for program testing and is of considerable use for metals.

5.2 Prager-Drucker Model

In order to remedy one of the limitations of the von Mises model, the pressure independence of material strength, a model proposed by Prager and Drucker involves the assumption that H is a linear function of mean pressure $P = -\frac{\sigma_{ii}}{3}$. An associated Prager-Drucker model then takes the form of

$$f(\sigma) = 3J_2 - H^2 = 3J_2 - \left(\alpha f_c + \beta P\right)^2 \tag{5.5-1}$$

$$M(\sigma) = N(\sigma) \tag{5.5-2}$$

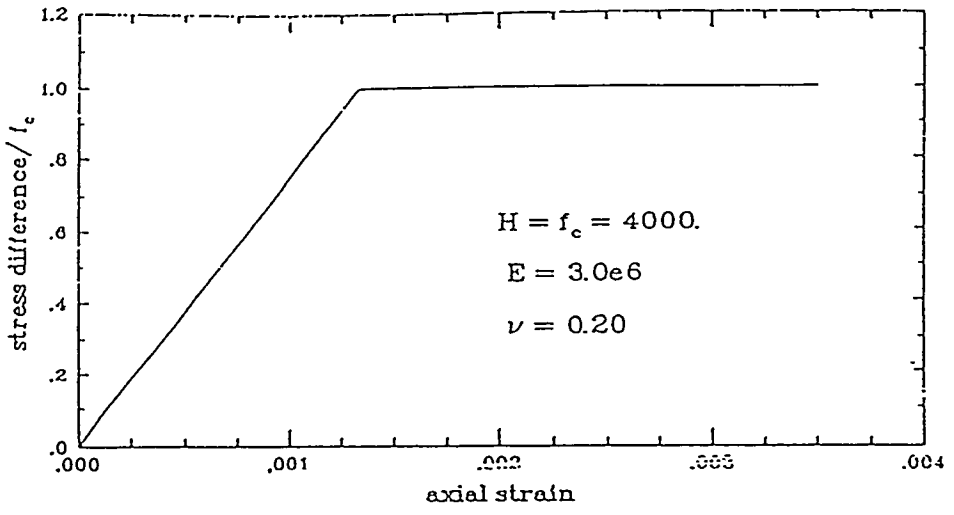

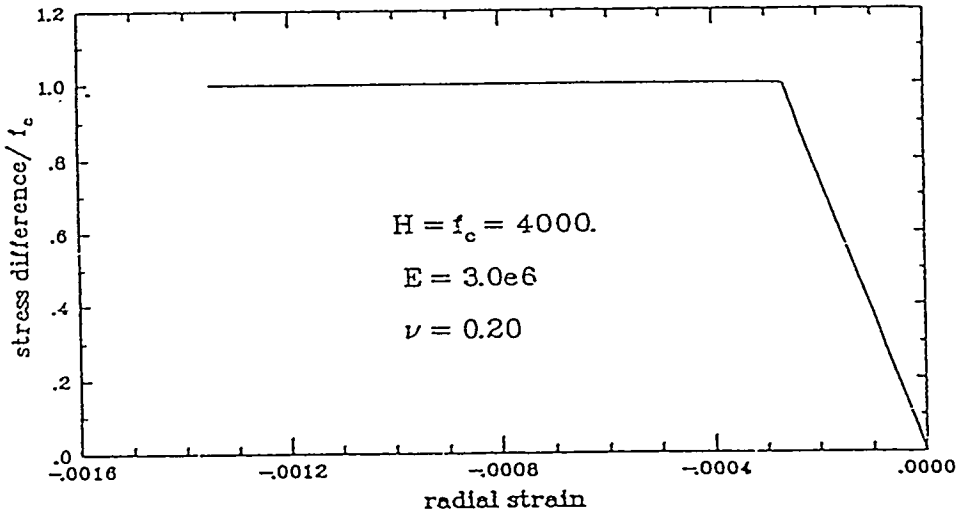

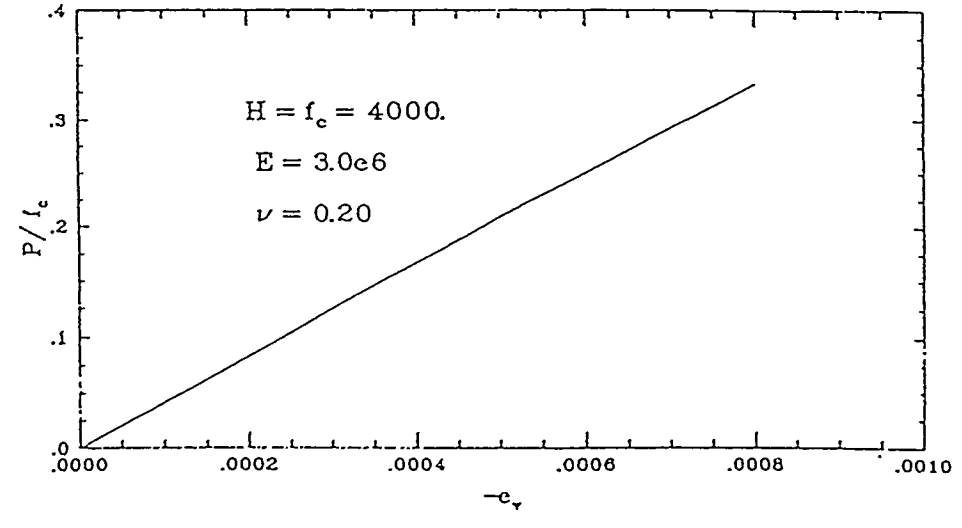

Figure 5-1. Stress-strain curves for triaxial compression predicted by the perfectly plastic von Mises model, with $P = -\frac{1}{3}\sigma_{ii}$ and $e_v = \varepsilon_{ii}$.

in which α, β, and f_c are material constants that can be determined from the slope and the intercept of the failure envelope plotted in the $P-\sqrt{3J_2}$ space. Triaxial compression tests can be employed to established the failure envelope for a given material. On the deviatoric plane, the yield surface $f=0$ is a circle, the radius of which changes with P. According to Eqs. (5.5-1) to (5.5-2), it follows that

$$\frac{\partial f}{\partial \sigma} = 3\sigma^d + \frac{2\beta}{3} Hi \tag{5.6-1}$$

$$N = \frac{1}{N}\frac{\partial f}{\partial \sigma} = \frac{9\sigma^d + 2\beta Hi}{3\sqrt{3}\left[6J_2 + (2\beta H)^2\right]^{\frac{1}{2}}} \tag{5.6-2}$$

$$N:E = E:M = \frac{6G\sigma^d + 2B\beta Hi}{\sqrt{3}\left[6J_2 + (2\beta H)^2\right]^{\frac{1}{2}}} \tag{5.6-3}$$

$$N:E:M = \frac{36GJ_2 + B(2\beta H)^2}{3\left[6J_2 + (2\beta H)^2\right]} \tag{5.6-4}$$

Stress-strain curves for triaxial compression are given in Figure 5-2 for various values of initial mean pressure, with $\alpha = 0.5$ and $\beta = 1.5$, which are representative of concrete. As can be observed, the enhancement of strength with mean pressure is displayed so that this model is a considerable improvement over the von Mises model. The use of the associated flow rule results in too much dilatation once the yielding occurs since

$$P^s:d\varepsilon^i = d\lambda P^s:M = d\lambda \frac{2\beta Hi}{3\sqrt{3}\left[6J_2 + (2\beta H)^2\right]^{\frac{1}{2}}} \tag{5.7}$$

This feature is considered to be undesirable for concrete, and therefore, a nonassociated Prager-Drucker model is often used with the flow rule being of the following form:

$$M = \frac{9\sigma^d + 2\beta' Hi}{3\sqrt{3}\left[6J_2 + (2\beta H)^2\right]^{\frac{1}{2}}} \tag{5.8}$$

in which β in Eq. (5.6-2) is merely replaced with β'. One possibility is $\beta' = 0$ for which only the deviatoric part of the total strain tensor contains inelastic components. A more suitable flow rule ($\beta' \neq 0$) should be devised if the correct amount of dilatation is to be predicted. Shear enhanced compaction can be predicted by choosing $\beta' < 0$, but then β'

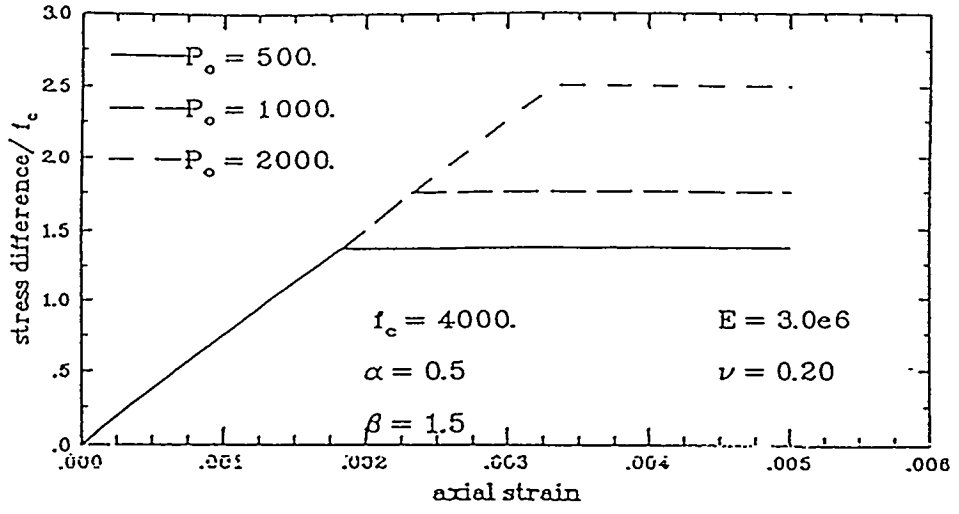

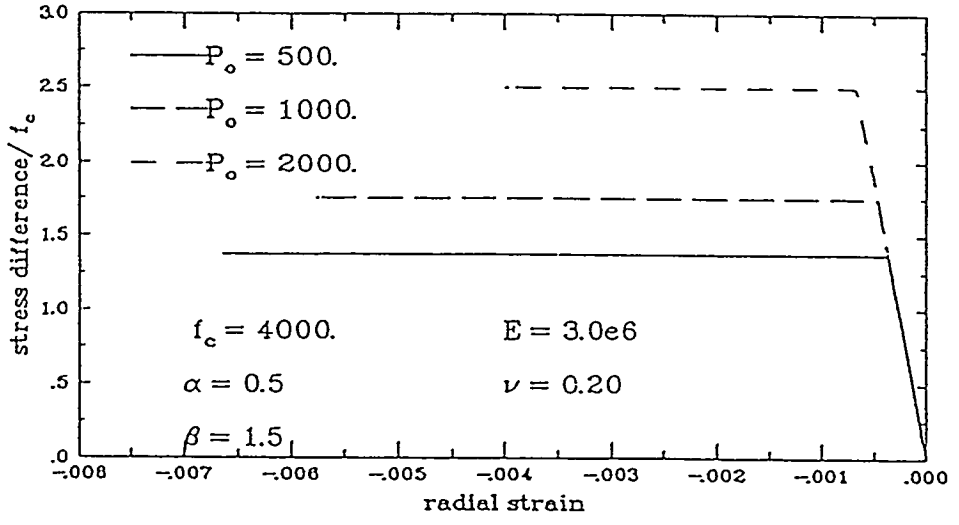

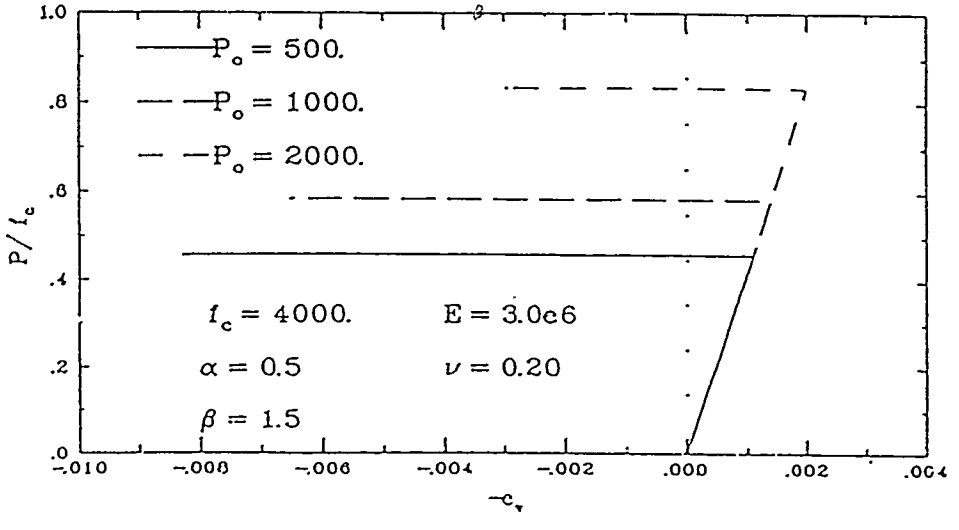

Figure 5-2. Stress-strain curves for triaxial compression predicted by the perfectly plastic Prager-Drucker model, with $P = -\frac{1}{3}\sigma_{ii}$ and $e_v = \varepsilon_{ii}$.

would have to change to predict dilatation. Such an approach becomes overly complicated. Other limitations of the model are the facts that no yielding for hydrostatic compression can be modeled and that the strength for negative mean pressure (tensile regime) is generally too high.

5.3 Modified Prager-Drucker Model

With the assumptions that J_2 attains a limiting value S_m as P increases positively and that the hydrostatic tensile strength is P_t, a more accurate representation of material strength as a function of mean pressure can be constructed. A modification to Eq. (5.5-1) that provides a smooth transition to S_m and P_t is given as follows:

$$H = \left(1 - e^{-k}\right)\left[\alpha f_c + \beta P\left(1 - e^{-y}\right)\right] \tag{5.9-1}$$

where

$$k = \left(1 - \frac{P}{P_t}\right)^m \tag{5.9-2}$$

$$y = \frac{S_m}{\beta(P - P_t)} \tag{5.9-3}$$

The material constants α, β, m, S_m, and P_t can be determined by curve fitting, such as with a least square method, in the $P - \sqrt{3J_2}$ space of experimental data obtained from triaxial compression tests. The yield surface described by $f = 0$ is shown in Figure 5-3 for the given parameters. The intersection with the P- axis at $P = P_t$ is exhibited together with the decrease in slope for large values of P.

With the use of either an associated or a nonassociated flow rule, stress-strain curves for typical triaxial compression paths obtained with this model are similar to those obtained from the Prager-Drucker model with the exception that improved values of strength are shown for the low and high range of mean pressure. However, this modified Prager-Drucker model is still inadequate if the details of inelastic deformation need to be simulated. And also, it is not efficient to form the tangent stiffness tensor in numerical integration schemes, because of the added complexity of the yield surface.

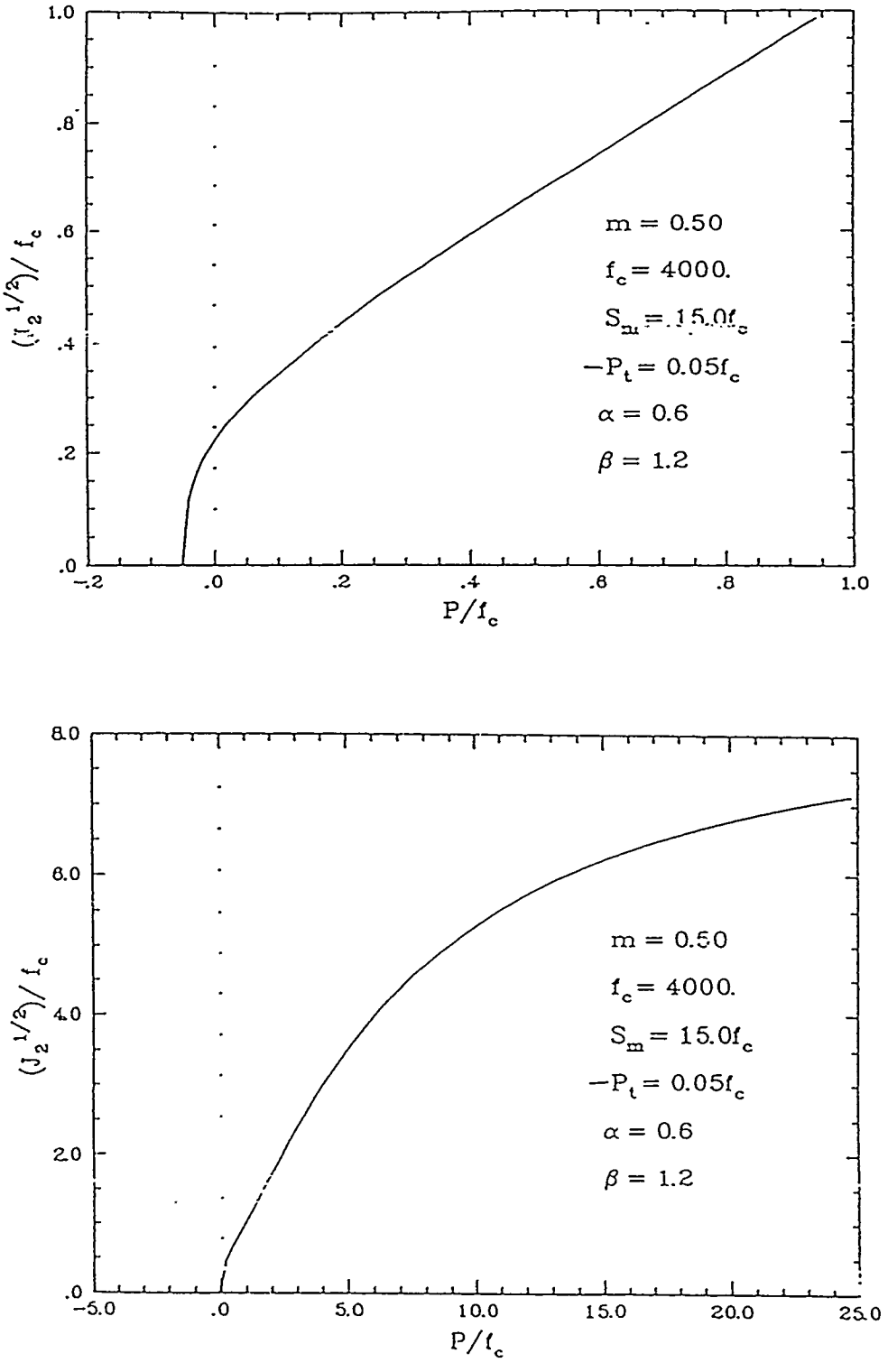

Figure 5-3. The yield surface with different scales for the modified Prager-Drucker model $\left(J_2 = \frac{1}{2}\sigma^d : \sigma^d \text{ and } P = -\frac{1}{3}\sigma_{ii}\right)$.

5.4 Noncircular Pressure-Dependent Model

All of the models discussed previously in this chapter define yield surfaces that are circular in the deviatoric plane. According to Chen [1982], experimental data in the deviatoric plane show that for a given value of mean pressure there is a considerable variation with polar angle in the limit value of effective stress. For low values of mean pressure, it is believed that the maximum principal stress criterion is most appropriate. For large values of mean pressure, the circular shape is considered adequate. Thus, an accurate limit state surface in the deviatoric plane should vary from a triangular shape at low values of mean pressure to a circular shape at high values of mean pressure. To do so, consider a yield function

$$f(\boldsymbol{\sigma}) = R\left(J_2 - \frac{H^2}{3}\right) + \left(\frac{2}{27}H^3 - III^d\right) \tag{5.10}$$

in which H is given by Eqs. (5.9), the third invariant III^d is defined as the negative determinant of the deviatoric stress, namely,

$$III^d = -det\left(\boldsymbol{\sigma}^d\right) \tag{5.11}$$

and R is a parameter that controls the shape of the yield surface $f = 0$ in the deviatoric plane. Examples are given in Figure 5-4 for various values of R and $H = 1$. The minimum value of R that gives a convex yield surface is $R = \frac{1}{3}$, while the surface for $R = 10$ is very close to circular. Hence, a simple relation where R increases with P is desirable. After an attempt to fit experimental data, the following relation appears to be suitable:

$$R = \frac{1}{3}\left(1 + \varsigma\frac{H}{f_c}\right) \tag{5.12}$$

where ς is a material parameter chosen to match experimental data. In the absence of data for a particular material, $\varsigma = 0.3$ provides a yield surface that is reasonable for concrete. The use of three stress invariants in constructing a noncircular yield surface was discussed in detail by Schreyer and Babcock [1985].

For triaxial compression, stress-strain curves based on this model are not different from those obtained with the modified Prager-Drucker model. However, for other classes of paths, the stress-strain curves are similar with the exception that the limit stresses are

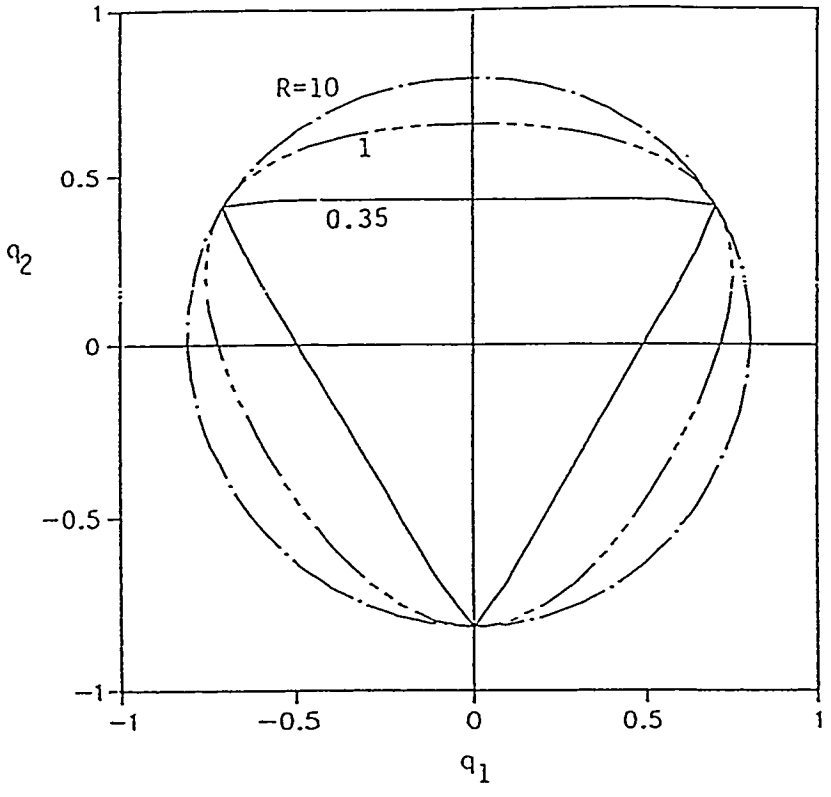

Figure 5-4. Dependence on R of the shape of the yield surface in the deviatoric plane $\left[q_1 = \frac{1}{\sqrt{6}}(\sigma_1 - \sigma_2) \text{ and } q_2 = -\frac{1}{\sqrt{18}}(\sigma_1 + \sigma_2 - 2\sigma_3) \right]$.

lower. For analyses where limit values must be accurate, the modifications to R and the yield surface with the third invariant of stress may be nontrivial in a constitutive model. In addition, it is not recommended to formulate the tangent stiffness tensor in numerical calculations because of the complexity of the yield surface.

6. ELASTIC-PLASTIC STRAIN HARDENING MODELS

Many frictional materials display a certain amount of ductility and an increase of yield strength beyond the elastic strength with increased deformation, a feature often called strain hardening. Since the elastic strain is only a part of the total strain during the hardening process, accurate analyses near the limit state require a good representation of the inelastic strain. The purpose of this chapter is to demonstrate how isotropic hardening models, which reflect the essential features of strain hardening, can be developed from the starting point of elastic-perfectly plastic models. The fundamental assumption of an isotropic hardening model is that stress appears in the expression for the yield function as invariants of stress only, but the internal variables can change with inelastic deformation. Suppose here that only one internal variable is used. Implicit in this assumption is that no matter which path is followed in stress space, the internal variable governing isotropic hardening obtains the same value at the limit state. Thus, the yield surface, flow rule, and hardening rules are assumed to be functions of the invariants of both stress and inelastic strain. At the limit surface, the model becomes one of perfect plasticity.

For engineering computations, whenever an element reaches the limit state, the consequent calculations in the post-peak regime should be suspect because large deformations may localize into an element. Without a proper treatment of softening with localization as indicated in Chapter 7, the predicted energy dissipation may be too high since zones of localization are frequently much smaller than the width of an element in a mesh generated for typical engineering calculations. Also, it must be pointed out that accurate predictions for strain under multiaxial states of stress are much harder to achieve than predictions for limit states in terms of stress. Future research should be able to resolve the limitations inherent in classical plasticity.

6.1 von Mises Model

The strain-hardening von Mises model with an associated flow rule is defined by

$$f(\boldsymbol{\sigma}, I_1) = 3J_2 - H^2(I_1) \tag{6.1-1}$$

$$M(\boldsymbol{\sigma}, I_1) = N(\boldsymbol{\sigma}, I_1) = \frac{1}{N}\frac{\partial f}{\partial \boldsymbol{\sigma}} \tag{6.1-2}$$

$$dI_1 = d\bar{e}^i = d\lambda \tag{6.1-3}$$

where the second invariant of inelastic strain, $\bar{e}^i$, is given by:

$$\bar{e}^i = \int \left(d\boldsymbol{\varepsilon}^i : d\boldsymbol{\varepsilon}^i \right)^{\frac{1}{2}} = \int \left\{ \left[d\lambda \frac{\boldsymbol{\sigma}^d}{\left(\boldsymbol{\sigma}^d : \boldsymbol{\sigma}^d \right)^{\frac{1}{2}}} \right] : \left[d\lambda \frac{\boldsymbol{\sigma}^d}{\left(\boldsymbol{\sigma}^d : \boldsymbol{\sigma}^d \right)^{\frac{1}{2}}} \right] \right\}^{\frac{1}{2}}$$
$$= \int d\lambda = \lambda \qquad (6.2)$$

Therefore, H is a hardening function of the internal variable $\bar{e}^i$. An elementary smooth relation can be assumed for H as follows:

$$H = H_0 + (H_L - H_0) \sin\left[\frac{\pi}{2} \left(\frac{\bar{e}^i}{\bar{e}^i_L} \right)^n \right] \qquad 0 \le \bar{e}^i < \bar{e}^i_L \qquad (6.3\text{-}1)$$

$$H = H_L \qquad \bar{e}^i \ge \bar{e}^i_L \qquad (6.3\text{-}2)$$

in which H_0 and H_L correspond to the elastic and peak strengths, respectively. The limit state is achieved when the inelastic strain invariant reaches the limit value $\bar{e}^i_L$. The material parameters H_0, H_L, $\bar{e}^i_L$, and n can be identified from an experimental stress-strain curve in a uniaxial stress test where $\sqrt{3J_2} = |\sigma_{11}|$ and $\bar{e}^i = |\varepsilon^i_{11}|$ for the case where the loading axis is identified as x_1.

On the deviatoric plane, the yield surface described by $f = 0$ is a circle, the radius of which expands with $\bar{e}^i$. Equations (5.3-1) to (5.3-4) are still valid because the partial derivative of the yield surface with respect to stress does not include the internal variable $\bar{e}^i$, but now the partial derivative of the yield surface with respect to the internal variable is not equal to zero because of the hardening feature and can be written as

$$\frac{\partial f}{\partial I_1} = \frac{\pi n (H_L - H_0)}{\bar{e}^i_L} \left(\frac{\bar{e}^i}{\bar{e}^i_L} \right)^{n-1} H \cos\left[\frac{\pi}{2} \left(\frac{\bar{e}^i}{\bar{e}^i_L} \right)^n \right] \qquad (6.4)$$

For many materials, $H_0 = \frac{H_L}{2}$ is a reasonable choice. Typical stress-strain curves with this choice and for various values of n are shown in Figure 6-1. It can be observed that with $n = 0.5$ a shape is achieved that is representative of many experimental data. The strain at which the maximum stress is reached can be adjusted through the parameter $\bar{e}^i_L$.

Since the yield surface and flow rule are formulated in the deviatoric stress space, the criticisms given in Section 5.1 are still applicable here except that the strain hardening phenomenon is now predicted. Therefore, this model is not of much use for geotechnical

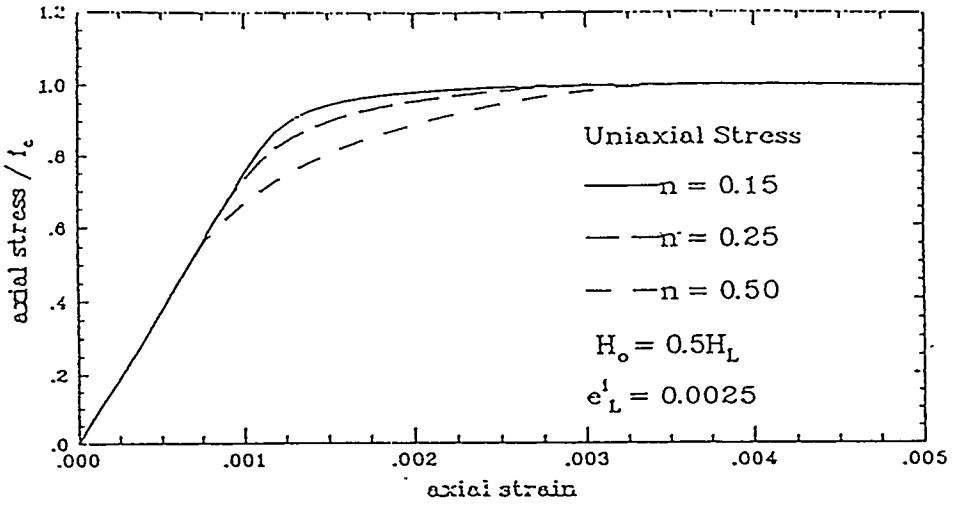

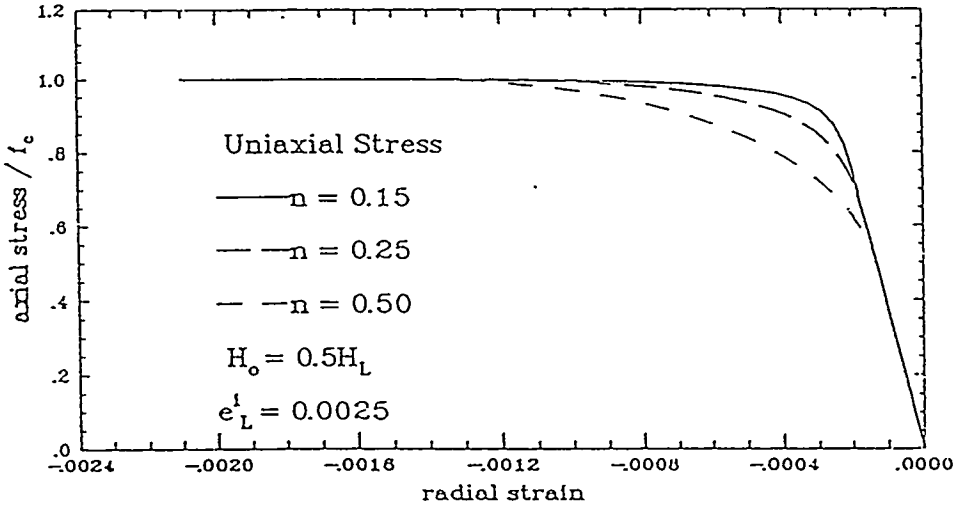

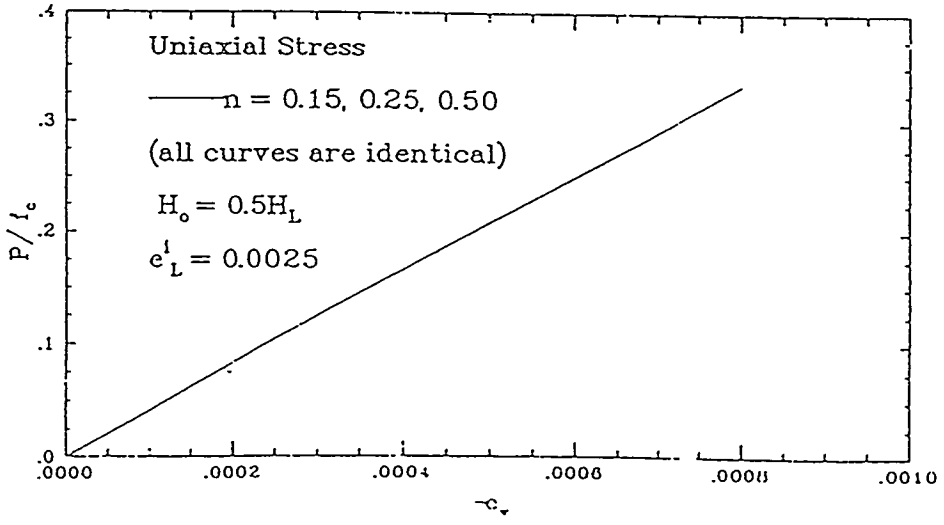

Figure 6-1. Stress-strain curves for uniaxial compression for a strain hardening von Mises model, with $P = -\frac{1}{3}\sigma_{ii}$ and $e_v = \varepsilon_{ii}$.

materials, although it is very suitable for describing the strain-hardening behavior of metals under monotonic loading.

6.2 Prager-Drucker Model

A strain-hardening version of the Prager-Drucker model is set up by choosing a yield surface of the type

$$f = 3J_2 - H^2(I_1, P) \tag{6.5-1}$$

$$M(\sigma, I_1) = N(\sigma, I_1) \tag{6.5-2}$$

$$dI_1 = d\bar{e}^i = d\lambda \tag{6.5-3}$$

where the hardening function takes the form of

$$H = H_0 + (H_L - H_0)\sin\left[\frac{\pi}{2}\left(\frac{\bar{e}^i}{\bar{e}^i_L}\right)^n\right] \qquad 0 \le \bar{e}^i < \bar{e}^i_L \tag{6.6-1}$$

$$H = H_L \qquad \bar{e}^i \ge \bar{e}^i_L \tag{6.6-2}$$

$$H_L = \alpha f_c + \beta P \tag{6.6-3}$$

The parameters α and β are defined in Section 5.2. Since H_L is now a linear function of mean pressure P, this model simulates both strain hardening and variations of material strength with mean pressure, which gives an improvement over the von Mises hardening model. On the deviatoric plane, therefore, the radius of the circle described by $f = 0$ changes not only with I_1 but also with P. Equations (5.6-1) to (5.6-4) can be valid here if the parameter β in those equations is replaced by $\beta \sin\left[\frac{\pi}{2}\left(\frac{\bar{e}^i}{\bar{e}^i_L}\right)^n\right]$, which reflects the hardening feature of the model. From Eqs. (6.5) to (6.6), it follows that the partial derivative $\frac{\partial f}{\partial I_1}$ can also be found from Eq. (6.4) with the new definition of H_L.

Typical stress-strain curves for triaxial compression are shown in Figure 6-2 for various values of mean pressure. As in Section 5.2, the pressure-volumetric strain curve still exhibits too much dilatation. If we redefine the internal variable I_1 in terms of the deviatoric part of the inelastic strain tensor, that is, let

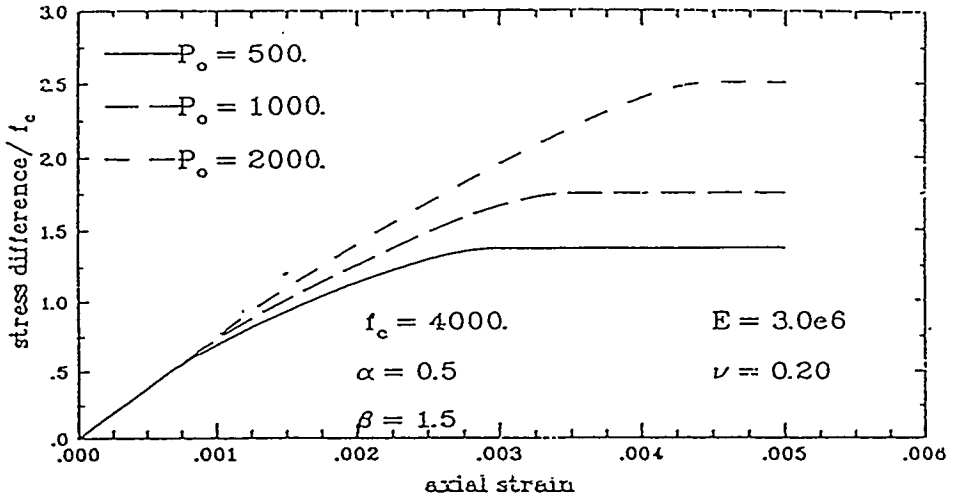

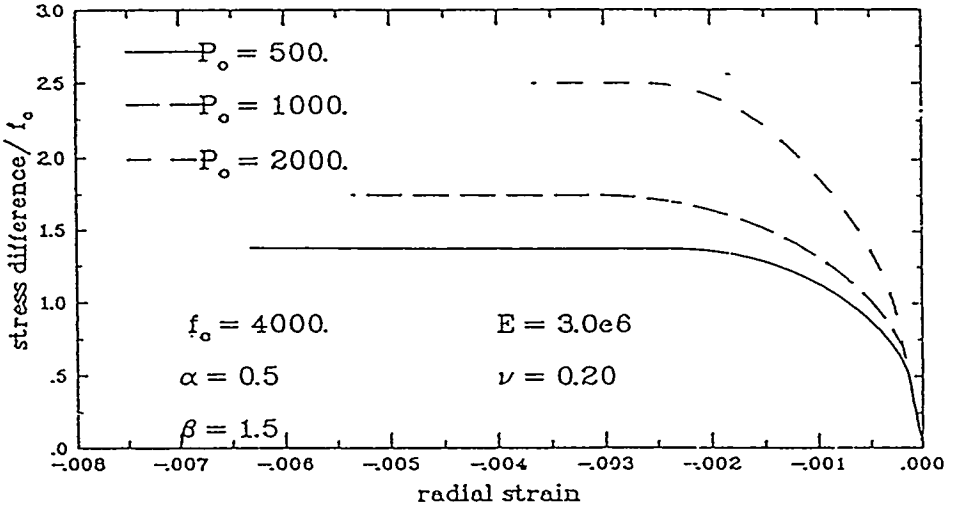

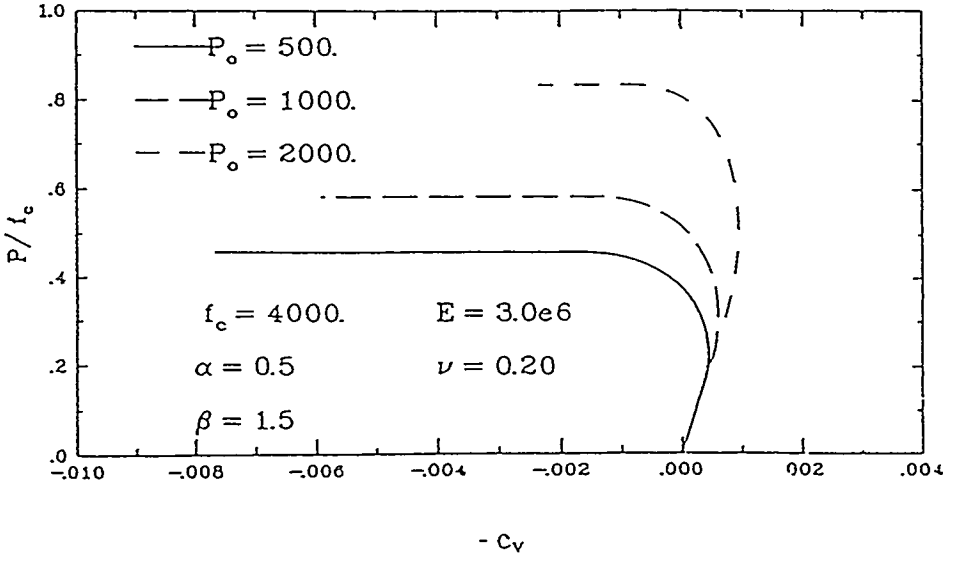

Figure 6-2. Stress-strain curves for triaxial compression for an associated hardening Prager-Drucker model, with $P = -\frac{1}{3}\sigma_{ii}$ and $e_v = \varepsilon_{ii}$.

$$I_1 = \bar{e}^{id} = \int \left(d\boldsymbol{\varepsilon}^{id} : d\boldsymbol{\varepsilon}^{id} \right)^{\frac{1}{2}} \tag{6.7-1}$$

$$\boldsymbol{\varepsilon}^{id} = \boldsymbol{\varepsilon}^{i} - \frac{1}{3}\varepsilon^{i}_{ii}\mathbf{i} \tag{6.7-2}$$

the almost identical results can be seen from Figure 6-3. This comparison illustrates the point that the choice of internal variable is usually not a critical factor in establishing an isotropic strain-hardening model, and instead, the flow rule plays an leading role as indicated by Eq. (5.7). If the flow rule of von Mises' type is used, the result is that no volumetric inelastic strain is predicted so that $\bar{e}^{id} = \bar{e}^{i}$. Typical stress-strain curves are given by Figure 6-4, which are different from those in the previous two figures.

Although strain hardening is now simulated, experimental data indicate much more inelastic behaviors for large values of mean pressure than those shown in Figures 6-2 through 6-4. The lack of correlation can be corrected by scaling the increment dI_1 with a coefficient proportional to the inverse of mean pressure. Such a modification is not warranted at this stage because of other limitations of the model, such as no shear enhanced compaction and no yielding for hydrostatic compression.

6.3 Modified Prager-Drucker Model

If H_L in Eqs. (6.6) is redefined by Eqs. (5.9), namely,

$$H = H_0 + (H_L - H_0)\sin\left[\frac{\pi}{2}\left(\frac{\bar{e}^{i}}{\bar{e}^{i}_{L}}\right)^{n}\right] \qquad 0 \le \bar{e}^{i} < \bar{e}^{i}_{L} \tag{6.8-1}$$

$$H = H_L \qquad \bar{e}^{i} \ge \bar{e}^{i}_{L} \tag{6.8-2}$$

$$H_L = \left(1 - e^{-k}\right)\left[\alpha f_c + \beta P\left(1 - e^{-y}\right)\right] \tag{6.8-3}$$

then a strain-hardening version of the modified Prager-Drucker model is obtained. The advantage of this model is that a realistic limit for negative mean pressure (tensile regime) is achieved and strain hardening is displayed for all paths except hydrostatic compression.

However, this model still contains some serious deficiencies. No shear enhanced compaction is shown for uniaxial strain and triaxial compression, and the amount of ductility displayed for triaxial compression is too low for a large mean pressure. In addition, the formulation of the tangent stiffness tensor is complicated.

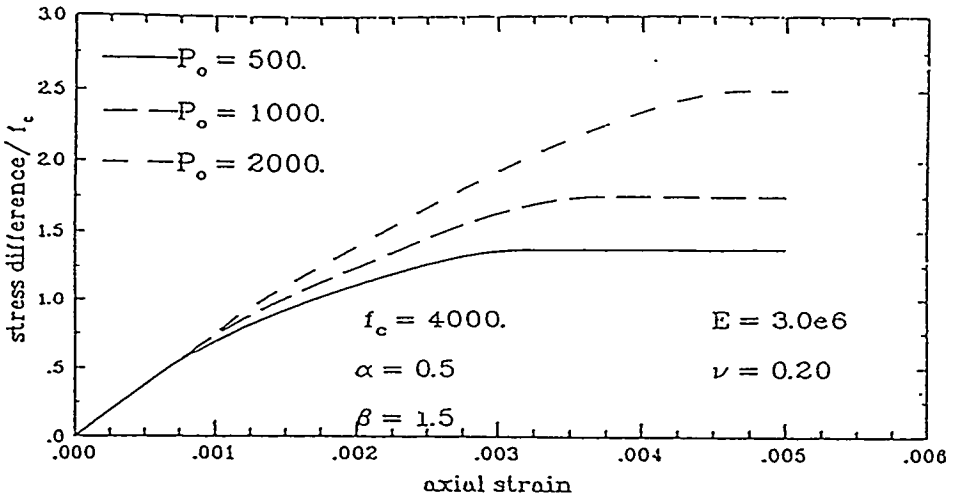

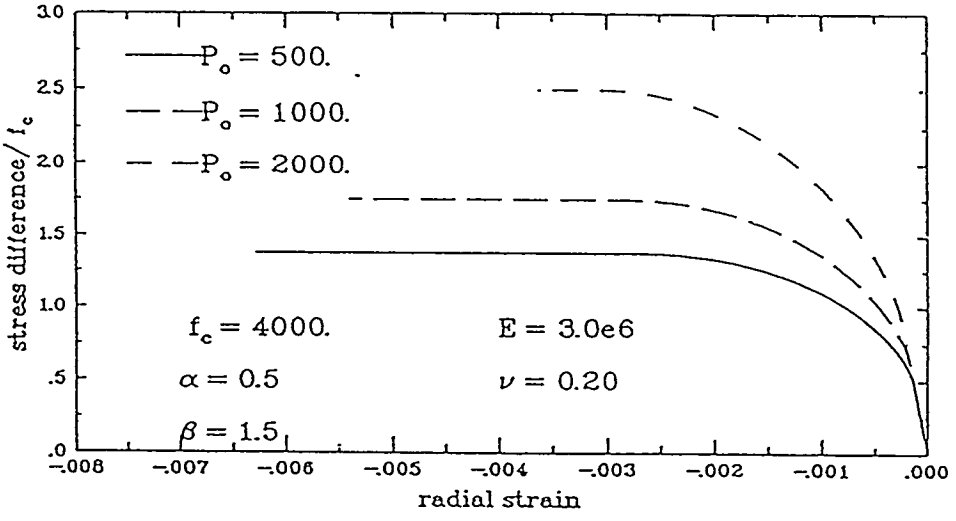

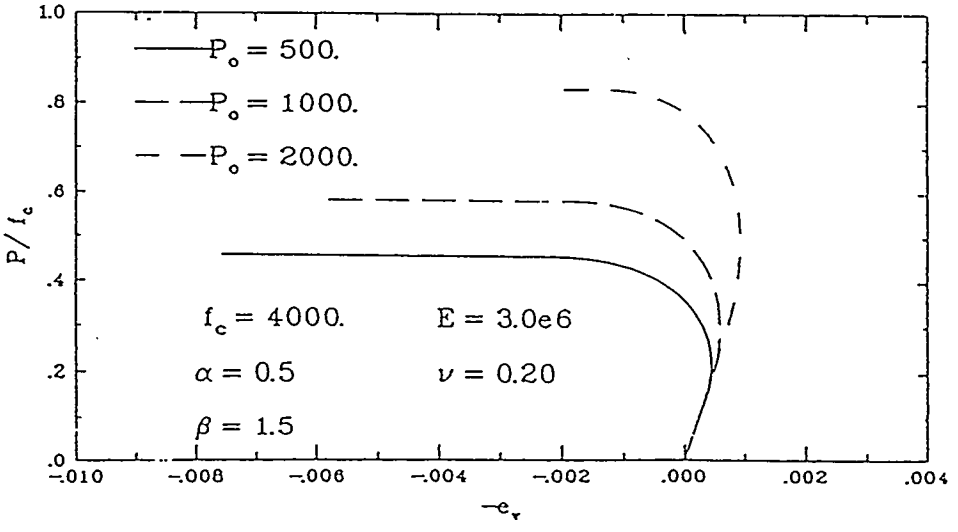

Figure 6-3. Stress-strain curves for triaxial compression for an associated hardening Prager-Drucker model with an alternative internal variable.

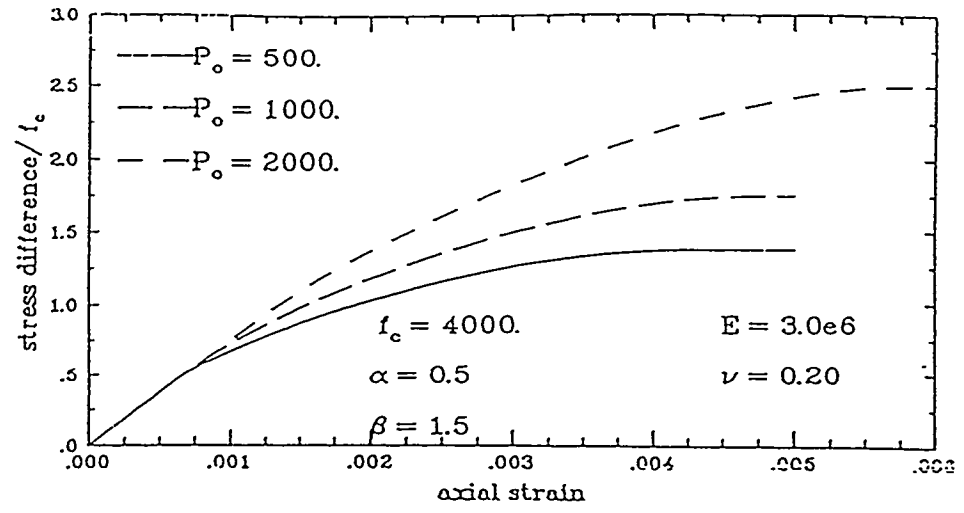

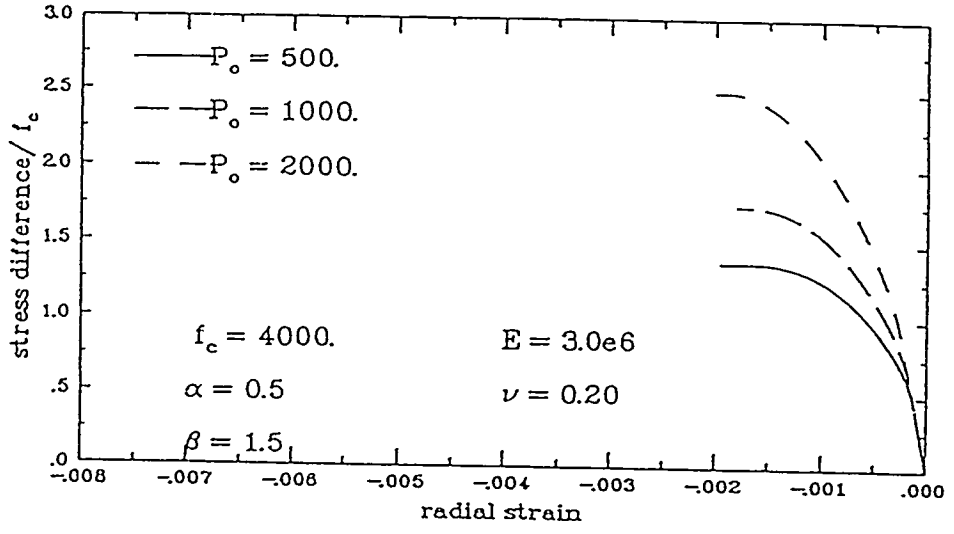

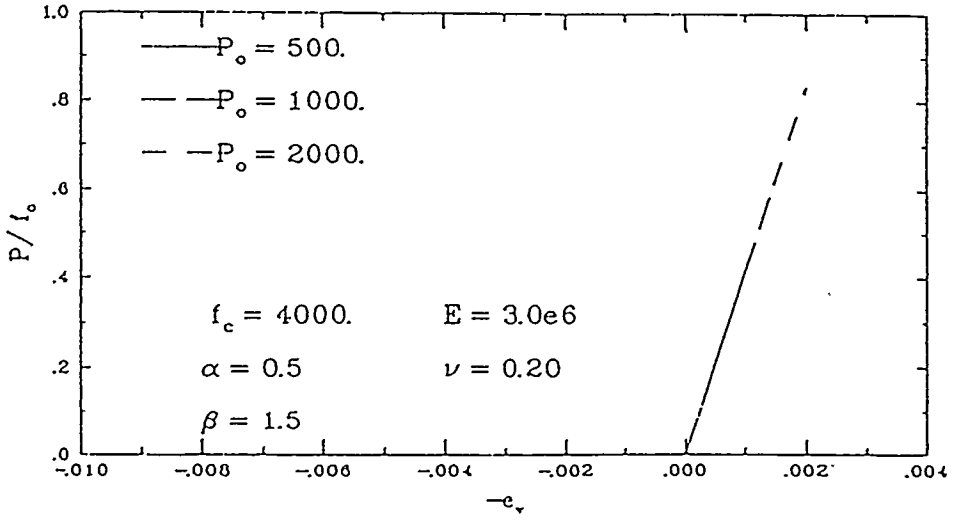

Figure 6-4. Stress-strain curves for triaxial compression for a nonassociated hardening Prager-Drucker model, with $P = -\frac{1}{3}\sigma_{ii}$ and $e_v = \varepsilon_{ii}$.

6.4 Noncircular Pressure-Dependent Model

A strain-hardening yield surface with a noncircular cross-section in the deviatoric plane can be developed if the function H in Eq. (5.10) is redefined by Eqs. (6.8). There is no question that for relatively small values of P, the hardening yield surface is triangular in the deviatoric plane. However, this degree of refinement for a general constitutive model involves considerably more computations, primarily because of the calculations of $\frac{\partial f}{\partial \sigma}$ and $\frac{\partial f}{\partial I_1}$. At present, it is difficult to justify such a degree of sophistication in computational codes so that the main focus of this chapter is to develop in the next section the modified Prager-Drucker model with a cap, which provides a balance among simplicity, computational efficiency, and reasonable predictions for the inelastic behavior of concrete.

6.5 Modified Prager-Drucker Model with a Cap

All the inelastic models investigated up to this stage can not simulate features representative of concrete, i.e.,

1. Strain hardening for all stress paths including hydrostatic compression,
2. More ductility predicted for paths associated with large values of mean pressure than for paths associated with low values of mean pressure, and
3. Shear enhanced compaction and dilatation.

In order to remedy the shortcomings of the previous models, the modified Prager-Drucker yield surface described in Section 6.3, which does not intersect with the positive P-axis in the $P-\sqrt{3J_2}$ space, can be connected to the positive P-axis by the addition of a cap surface. Several versions of cap models are available [Sandler et al., 1976; Sandler and Rubin, 1979; Resende and Martin, 1985; Faruque and Chang, 1986; Simo et al., 1988], but some of them involve a discontinuity in slope at the junction of the original yield surface and the cap surface. Since the flow rule usually contains the normal to the yield surface, the flow rule for a stress state at the junction point is complicated by the consistency conditions associated with two yield surfaces that must be satisfied simultaneously. The result is an integration scheme that is more complicated than if a single smooth surface is used.

By trial and error, a single yield surface providing a smooth transition from the modified Prager-Drucker surface to the cap surface can be developed. The yield surface is continuous and has a continuous derivative everywhere so that a corner algorithm is not required. In addition, the flow rule is associated, the yield surface is convex and intersects

the P -axis at right angles for both positive and negative values of P, so that the uniqueness of solutions is assured and no deviatoric strain occurs for hydrostatic stress states.

6.5.1 Description of the Model

A smooth yield surface is defined by

$$f(\sigma, I_i) = 3J_2 - \hat{H}^2 \tag{6.9-1}$$

$$M(\sigma, I_i) = N(\sigma, I_i) \tag{6.9-2}$$

$$I_1 = \bar{e}_1^i = \int \frac{P_0}{P + P_0} d\bar{e}^{id} \tag{6.9-3}$$

$$I_2 = \bar{e}_2^i = \int \left\langle -d\varepsilon_{ii}^i - c_2 d\bar{e}^i \right\rangle^1 \tag{6.9-4}$$

with

$$\hat{H} = HH_c \tag{6.10}$$

where the hardening function H takes the form of

$$H = H_L \left\{ H_0 + (1 - H_0) \sin\left[\frac{\pi}{2} \left(\frac{\bar{e}_1^i}{\bar{e}_L^i} \right)^n \right] \right\} \qquad 0 \le \bar{e}_1^i < \bar{e}_L^i \tag{6.11-1}$$

$$H = H_L \qquad \bar{e}_1^i \ge \bar{e}_L^i \tag{6.11-2}$$

$$H_L = \left(1 - e^{-k}\right)\left[\alpha f_c + \beta P\left(1 - e^{-y}\right)\right] \tag{6.11-3}$$

with k and y defined by Eqs. (5.9-2) and (5.9-3). The key point for obtaining a smooth transition between two surfaces is the choice of the cap function H_c . Here, the choice is made to let

$$H_c = \left| 1 - \frac{(P - sP_c)^2}{(P_c - sP_c)^2} \right|^q sign(P_c - P) \qquad P > sP_c \tag{6.12-1}$$

$$H_c = 1 \qquad P \le sP_c \tag{6.12-2}$$

where

$$s = c_1 + (0.98 - c_1)\left(\frac{\bar{e}_1^i}{\bar{e}_L^i}\right)^{c_4} \tag{6.12-3}$$

$$P_c = P_{co}\, exp\left(c_3 \frac{\bar{e}_2^i}{\bar{e}_L^i}\right) \tag{6.12-4}$$

In Eqs. (6.9) to (6.12), which describe the yield surface, the material parameters can be grouped according to their function as follows.

The limit state H_L is defined by α, β, P_t, m, and S_m in the $P - \sqrt{3J_2}$ space as shown in Figure 5-3. For a linear approximation given by Eq. (5.5-1), αf_c is the intercept on the $\sqrt{3J_2}$-axis and β is the slope. The intercept of the surface with the negative P-axis (hydrostatic tension) is P_t. The shape of the transition from the tensile intercept to the hydrostatic compression regime is controlled by m. The maximum value of $\sqrt{3J_2}$ for large positive P is adjusted through S_m.

The strain hardening of the yield surface, as reflected through Eq. (6.11-1), is governed by the parameters H_0, $\bar{e}_L^i$, and n. The fraction of the peak limit stress, where inelasticity first appears, is given by H_0. The strain invariant of Eq. (6.2) or (6.7-1) proves to be inadequate if reasonable predictions of strain are required, since the use of Eq. (6.2) or (6.7-1) implies that the same amount of shear deformation is obtained to reach the limit state regardless of the value of mean pressure. Experimental data suggest that for a tensile state of stress or strain, less shear deformation is needed than for a compressive state. Hence, the invariant defined by Eq. (6.9-3) is proposed for use in Eqs. (6.11). As a material parameter, P_0 controls ductility. If P_0 is large relative to P for all points on a stress path, the invariant $\bar{e}_1^i$ reduces to the usual deviatoric invariant $\bar{e}^{id}$. However, if P_0 is small relative to P, then $d\bar{e}_1^i$ will accumulate at a slower rate than $d\bar{e}^{id}$. The result is that for large values of P, the model will predict a greater amount of ductility, which is a feature exhibited by many frictional materials. The parameter P_0 can be determined together with $\bar{e}_L^i$ by matching uniaxial and triaxial data. The shape of the strain-hardening curve is controlled by n.

The shape and change of the cap surface is described by Eqs. (6.12-1) to (6.12-4) and adjusted through the parameters q, P_{co}, c_1, c_2, c_3, and c_4. The absolute value is required so that the operation involving the exponent q ($0 < q < 1$) can be performed. The exponent q controls the shape of the cap surface. P_c is the value of P at which the cap surface intersects the positive P- axis. The function H_c and hence $\hat{H}$ is zero when $P = P_c$. The value of P_c evolves with compressive volumetric strain. If shear is present, the increase in pressure with volumetric strain should be less rapid, which is called shear enhanced compaction as shown in Figure 3-4(a). To predict the shear enhanced compaction, P_c in Eq. (6.12-4) is assumed to be a function of the strain invariant defined

by Eq. (6.9-4) where $d\bar{e}_2^i$ equals the quantity inside the triangular bracket if the quantity is positive and otherwise, zero. For a hydrostatic compression test, $\bar{e}_2^i = -\varepsilon_{ii}^i$ and P_{co} is the value of P where inelastic deformation is first exhibited. The material parameter c_3 is chosen to provide a fit to the experimental data, and the shape of the predicted pressure versus volumetric strain curve under hydrostatic pressure is described through c_3. The degree of shear enhanced compaction under uniaxial strain is governed by the parameter c_2. H_c is defined to be unity for $P \leq sP_c$ such that the point $P = sP_c$ connects the modified Prager-Drucker surface to the cap surface where $P > sP_c$. The derivative of H_c with respect to P is zero at $P = sP_c$ and infinite at $P = P_c$. The first condition provides the continuous derivative between two surfaces, while the last condition yields a strictly volumetric compaction under hydrostatic compression. The sign function is appended to produce a negative value to H_c whenever $P > P_c$, a situation that can occur during numerical calculations. In order to control the value of P at which the cap function becomes effective, s, in Eq. (6.12-3), is taken to be a function of inelastic deformations as observed from experimental results. c_1 is a material parameter that provides the location where the cap surface first displays a horizontal tangent. The point sP_c varies from an initial value of $c_1 P_c$ to $0.98P_c$ at the limit point that means the cap becomes almost flat and perpendicular to the positive P- axis as the limit state is approached. The parameter c_4 is used to monitor the rate at which s increases with inelastic strain, and a value of $c_4 = 1$ appears adequate for most cases. The value of c_1 can be determined by identifying the lowest confining pressure where triaxial loading curves first display shear enhanced compaction.

In summary, the material parameters can be divided into the following three groups:

Limit state:	α, β, P_t, m, S_m
Strain hardening:	H_0, $\bar{e}_L^i$, n, P_0
Cap surface:	q, P_{co}, c_1, c_2, c_3, c_4

The shear part of the whole yield surface evolves to the limit state while the cap part moves monotonically out along the positive P- axis. The incremental-iterative integration schemes discussed in Subsection 4.2.3 should be used to solve the nonlinear constitutive equations consisting of Eqs. (6.9) to (6.12), and it is not numerically efficient to find the tangent stiffness tensor. In the following subsection, typical values of material parameters for concrete are given, and the effect of each parameter is explored by the use of Algorithm 4 discussed in Subsection 4.2.3.

6.5.2 Sensitivity of Material Parameters for Concrete

For design purposes, the most important material parameters are usually those associated with the limit state. A straight line fit to data in the $P-\sqrt{3J_2}$ plane immediately results in values for αf_c and β. If f_c is taken to be the peak strength in uniaxial compression, it follows from Eq. (5.5-1) that

$$\alpha+\frac{\beta}{3}=1 \tag{6.13}$$

Typical values for concrete are $\alpha = 0.6$ and $\beta = 1.2$. The strength in hydrostatic tension is often not available from experimental data so that P_t must be selected along with m to fit data in the tensile zone. Values of $P_t = -0.05\ f_c$ and $m = 0.75$ are reasonable for concrete. Data are rarely available for large values of P, and hence, $S_m = 25 f_c$ is recommended here based on extrapolation. The effects of m and S_m on the limit surface are shown in Figure 6-5 for $P_t = -0.05 f_c$, $\alpha = 0.6$ and $\beta = 1.2$.

The initial shape of the cap is governed by the parameters c_1, q, and P_{co}. The parameter P_{co} denotes the value where inelasticity first appears in the experimental curve describing hydrostatic pressure as a function of volumetric strain. If this value is not available, $P_{co} = f_c$ is reasonable for concrete. The transition point where the cap attains a horizontal tangent is given by $P = c_1 P_{co}$ with $c_1 = 0.4$ recommended for concrete unless triaxial compression test data for several different values of confining pressure are available. The value of P at which shear compaction is first noted for the lowest confining pressure identifies c_1. These experimental data can also be adopted to determine q although $q=\frac{1}{2}$ appears to be satisfactory for most cases. Figure 6-6 shows the effect of q on the shape of the cap.

Triaxial or uniaxial data are useful for identifying the strain hardening parameters. The fraction of the limit strength at which inelasticity first appears is given by H_0 with $H_0 = 0.5$ a reasonable choice for most materials. The value of the invariant of the inelastic strain at the limit state, $\bar{e}_L^i$, can be taken to be 0.0025 for concrete. The shape of the stress-strain curve in the hardening regime is controlled through the parameter n although $n = 0.5$ seems most appropriate for almost all materials. The effects of these parameters are shown in Figure 6-7.

Under hydrostatic compression, most frictional materials display an initial elastic regime, then a regime of monotonically decreasing stiffness followed by that of monotonically increasing stiffness up to the value of initial volumetric elastic stiffness. An exponential function defined in Eq. (6.12-4) has been chosen to reflect this observed

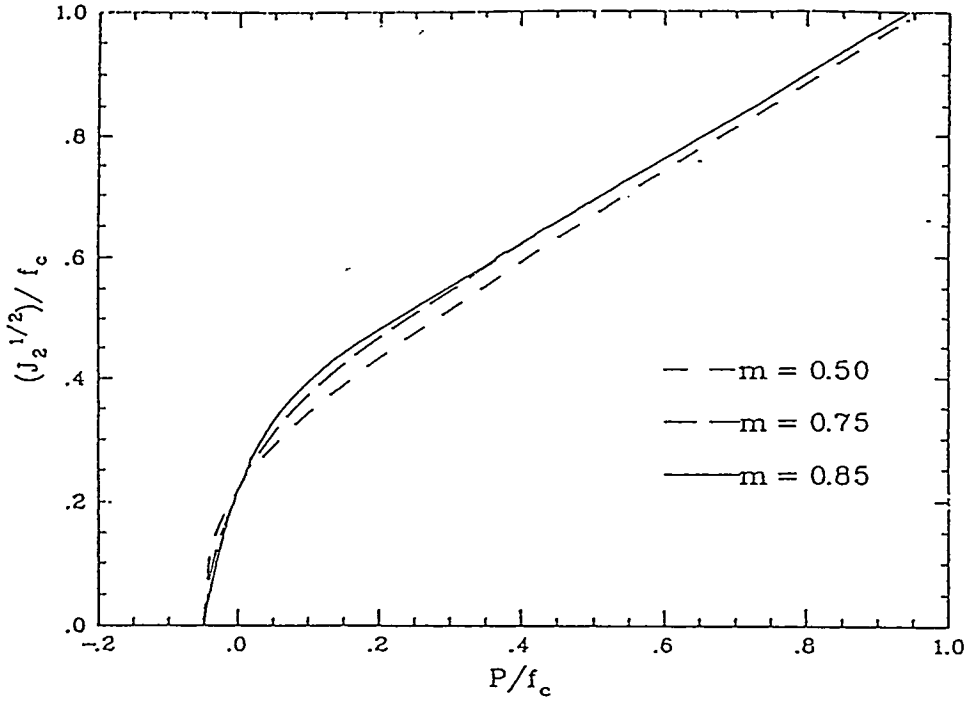

(a) Effect of m

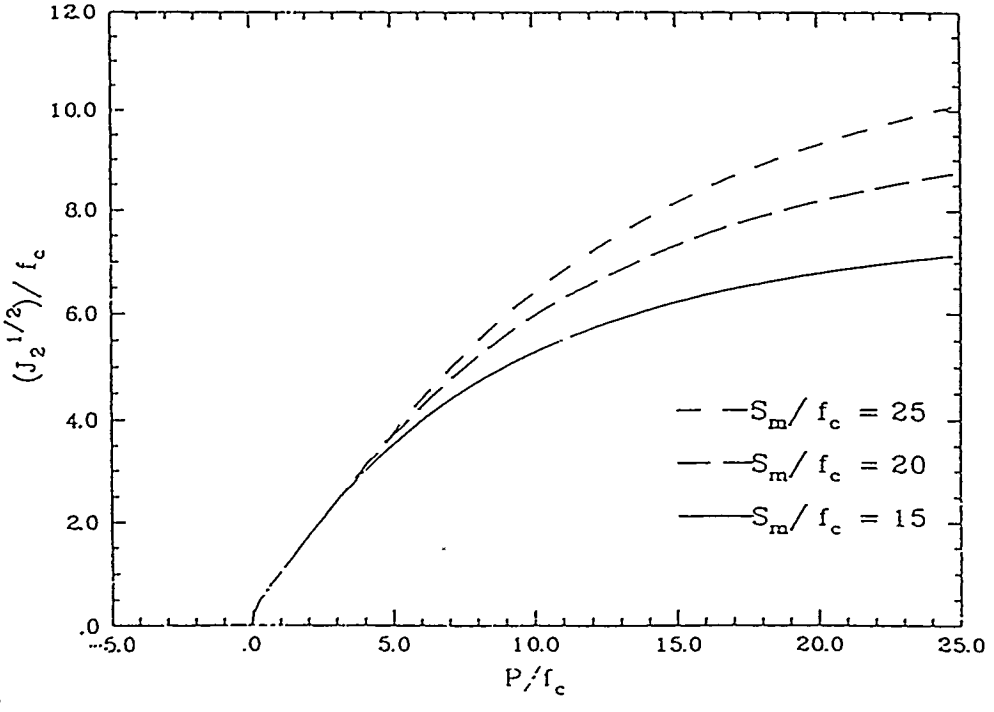

(b) Effect of S_m

Figure 6-5. The effects of m and S_m on the limit surface, with $J_2 = \frac{1}{2}\,\sigma^d{:}\,\sigma^d$ and $P = -\frac{1}{3}\,\sigma_{ii}$.

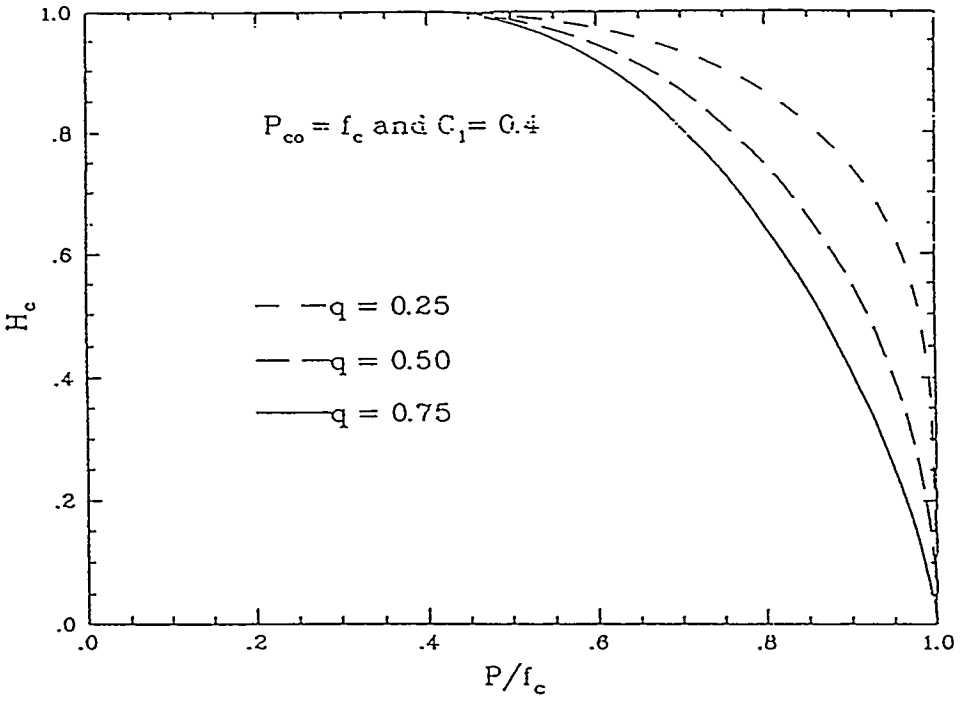

Figure 6-6. The effect of q on the shape of the cap, with $P = -\frac{1}{3}\sigma_{ii}$.

feature. Under hydrostatic compression, $d\bar{e}_2^i = \left|d\varepsilon_{ii}^i\right|$ so that the only remaining parameter in Eq. (6.12-4) to fit data is c_3. The effect of c_3 is shown in Figure 6-8. If the experimental data cannot be fitted satisfactorily, then a different mathematical formulation must be prescribed.

Triaxial paths generally display both shear enhanced compaction and enhanced ductility with an increase in confining pressure. Thus, the last two parameters to be determined, P_0 and c_2, can be found simultaneously from triaxial data. The most difficult task is to seek reasonable values to initiate a sensitivity study. For concrete, however, $P_0 = 5f_c$ and $c_2 = 1$ have appeared to be a good choice so that these values can be used as starting values for obtaining a fit to a specific material. The effects of variations in these two parameters are shown in Figures 6-9 and 6-10 for the case where the other parameters were assigned the "standard" values described previously in this subsection and confining pressure is taken to be f_c.

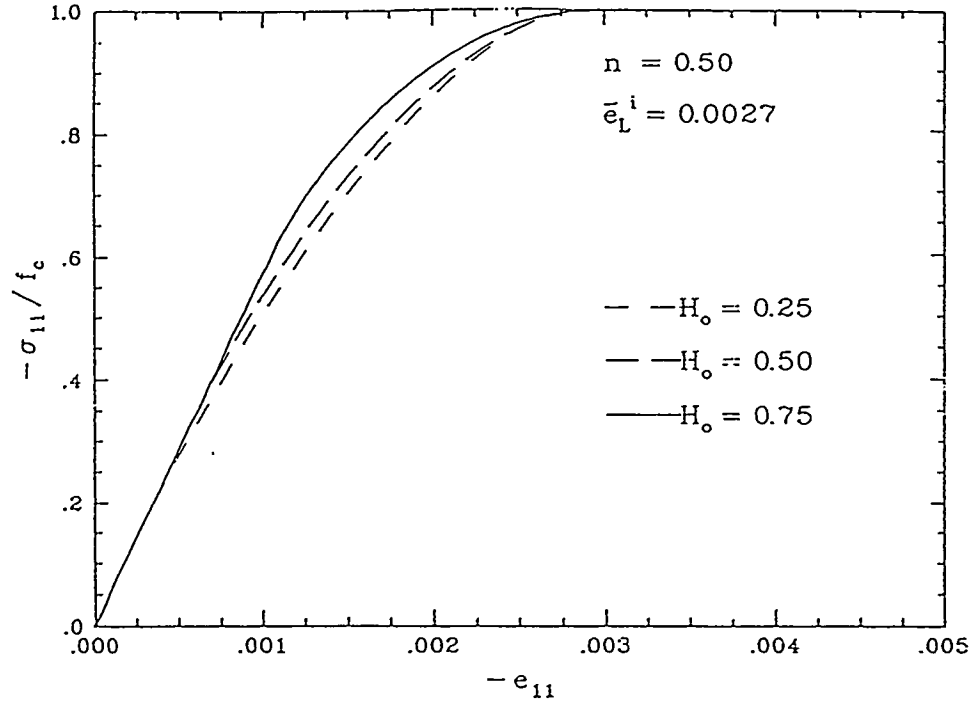

(a) Effect of H_0

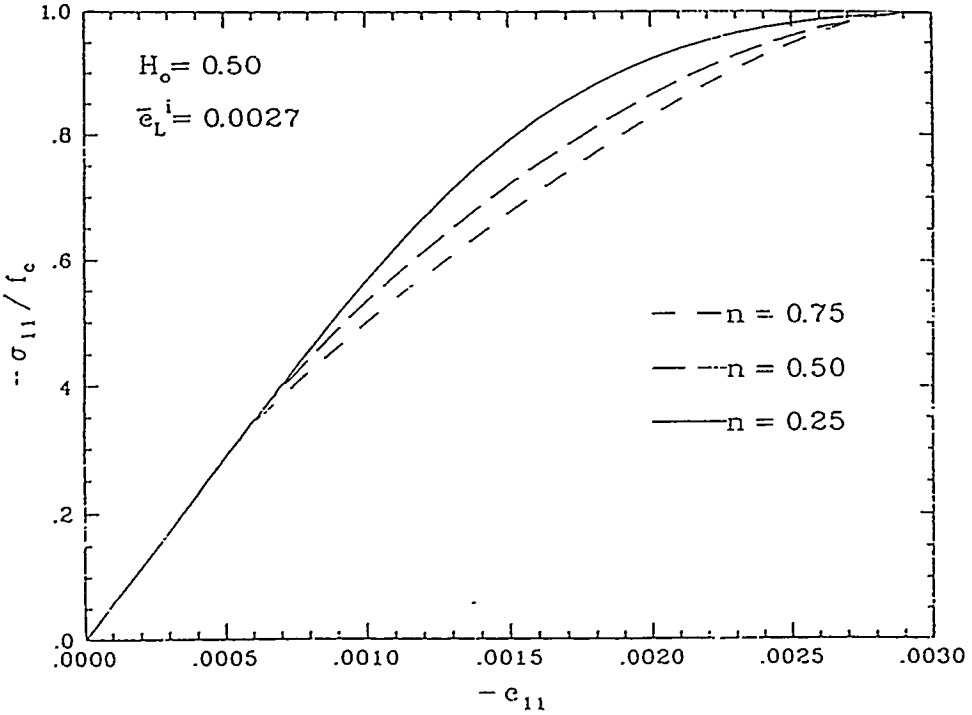

(b) Effect of n

Figure 6-7. The effects of strain hardening parameters on the predicted stress-strain curve for uniaxial stress in compression.

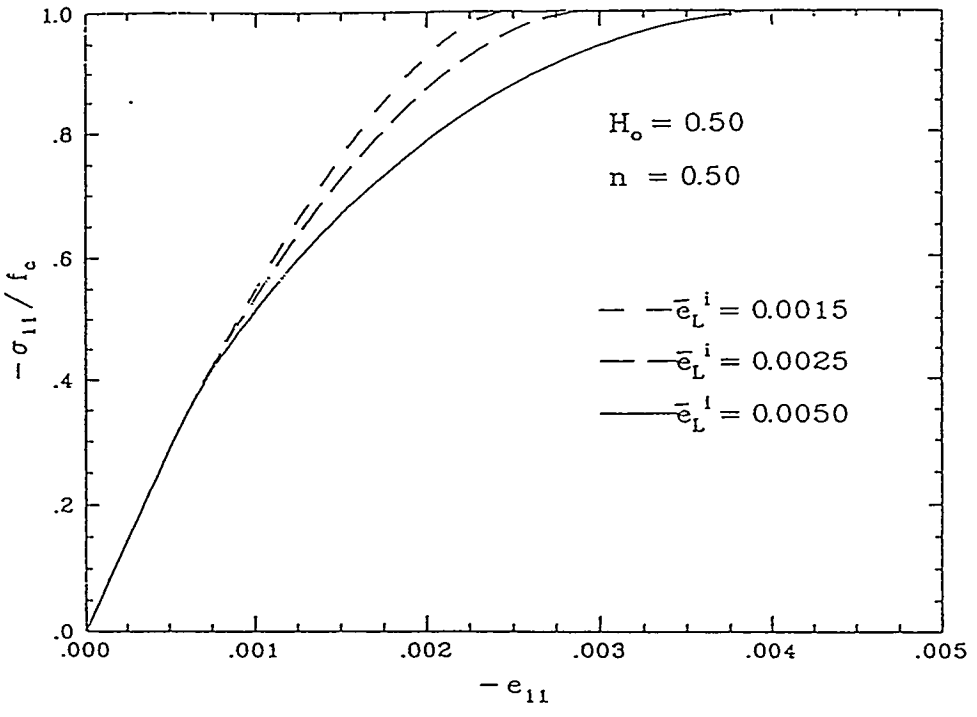

(c) Effect of $\bar{e}_L^i$

Figure 6-7. (continued) The effects of strain hardening parameters on the predicted stress-strain curve for uniaxial stress in compression.

The following list gives the standard values of material parameters for concrete:

$\alpha = 0.6$	$\beta = 1.2$	$P_t = -0.05 f_c$	$m = 0.75$
$S_m = 25 f_c$	$P_{co} = f_c$	$q = 0.5$	$c_1 = 0.4$
$c_2 = 1$	$c_3 = 1$	$c_4 = 1$	$P_0 = 5 f_c$
$\bar{e}_L^i = 0.0025$	$n = 0.5$	$H_0 = 0.5$	

6.5.3 Comparison of the Model Predictions with Experimental Data

To illustrate the degree of agreement of experimental data with the modified Prager-Drucker model with a cap, model predictions for a high-strength concrete are compared with experimental data in stress-strain plots.

With the use of the experimental data of Green and Swanson [1973], the values of material parameters were obtained by curve fitting following the method mentioned in the previous subsection. This procedure can be systematized to rigorously minimize the error norm for an optimal fit to experimental data [Kovarna, 1981; Simo et al., 1988]. The

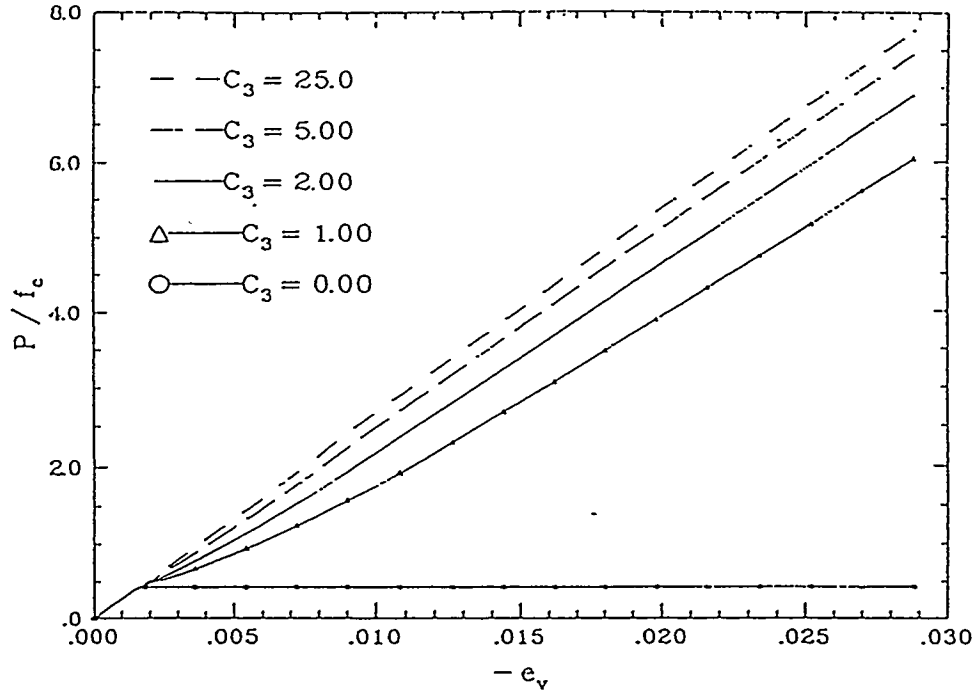

(a) Normalized pressure versus total volumetric strain

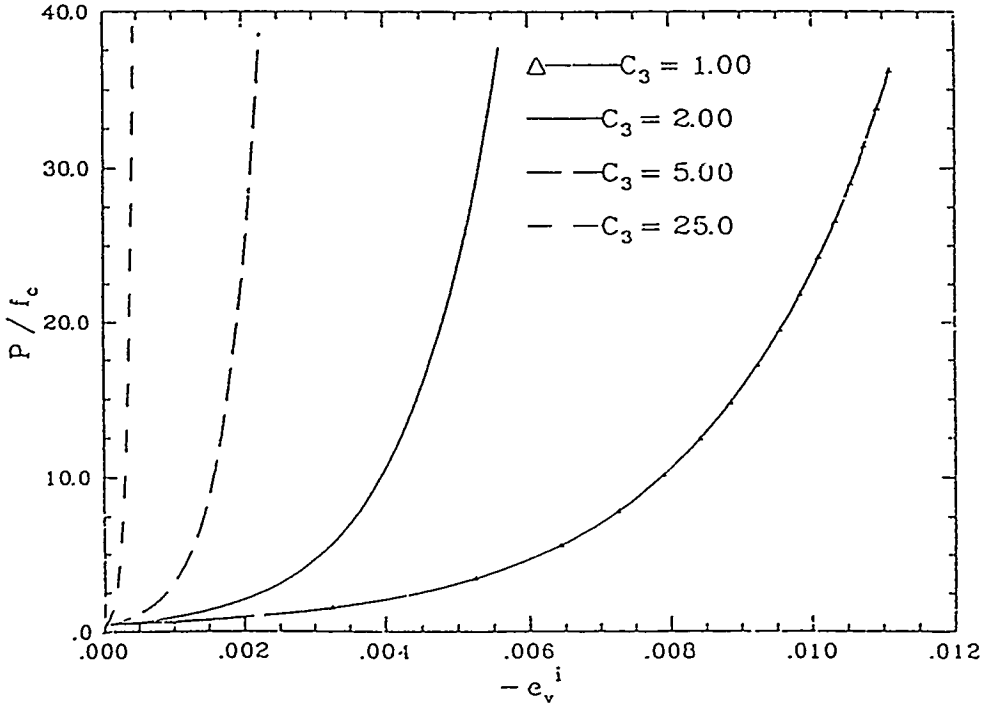

(b) Normalized pressure versus inelastic volumetric strain

Figure 6-8. The effect of the parameter *C3* on the predicted response for hydrostatic compression.

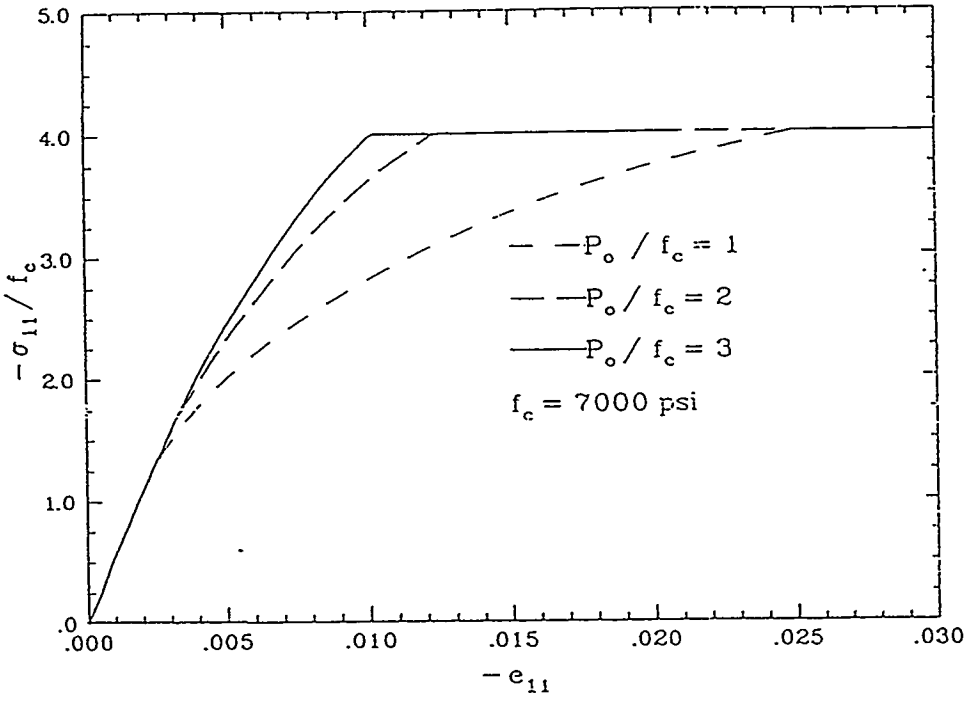

(a) Longitudinal stress versus strain

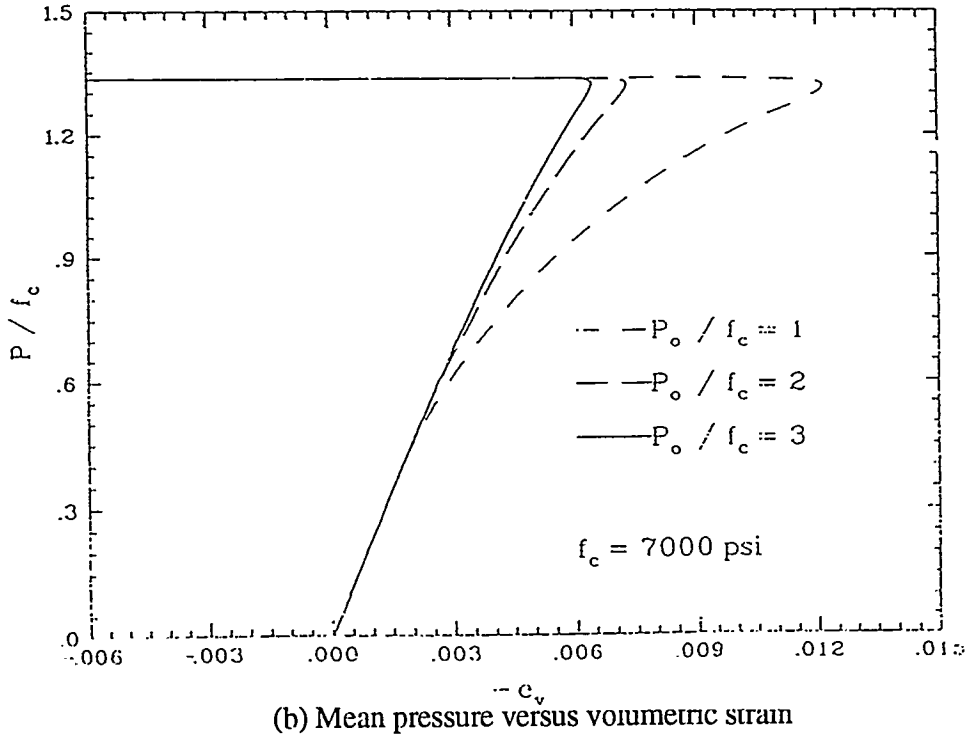

(b) Mean pressure versus volumetric strain

Figure 6-9. The effect of the parameter P_0 on the predicted response for triaxial compression.

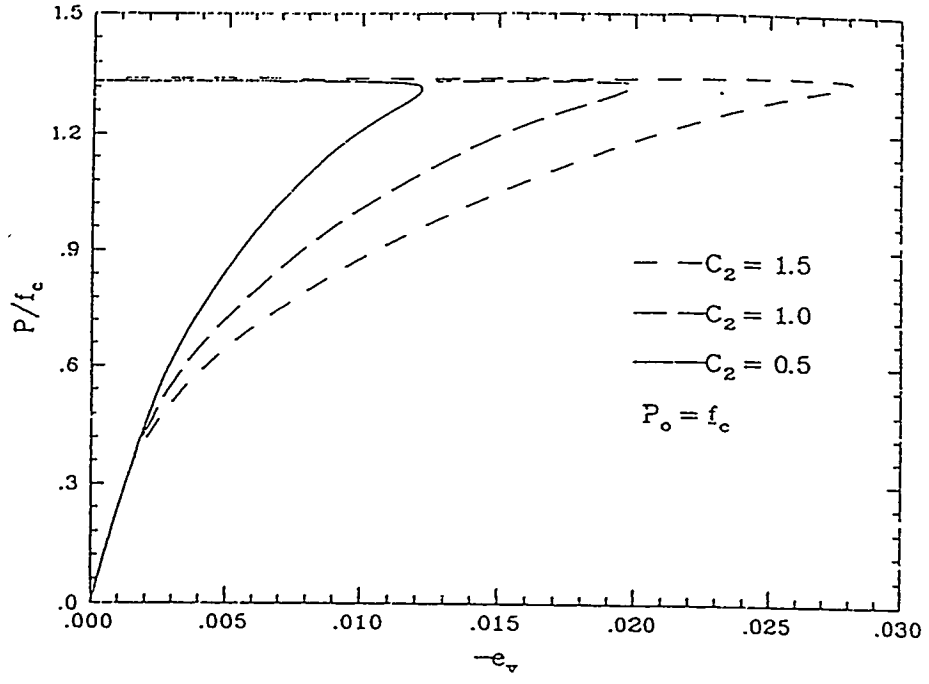

(a) Mean pressure versus volumetric strain for triaxial compression

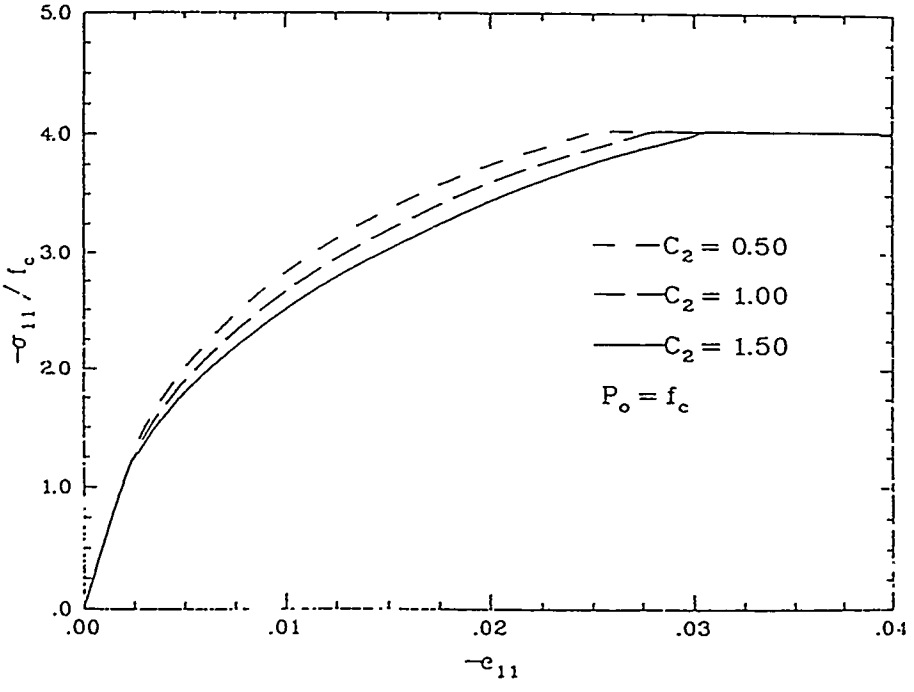

(b) Stress versus strain for triaxial compression

Figure 6-10. The effect of the parameter C_2 on shear enhanced compaction.

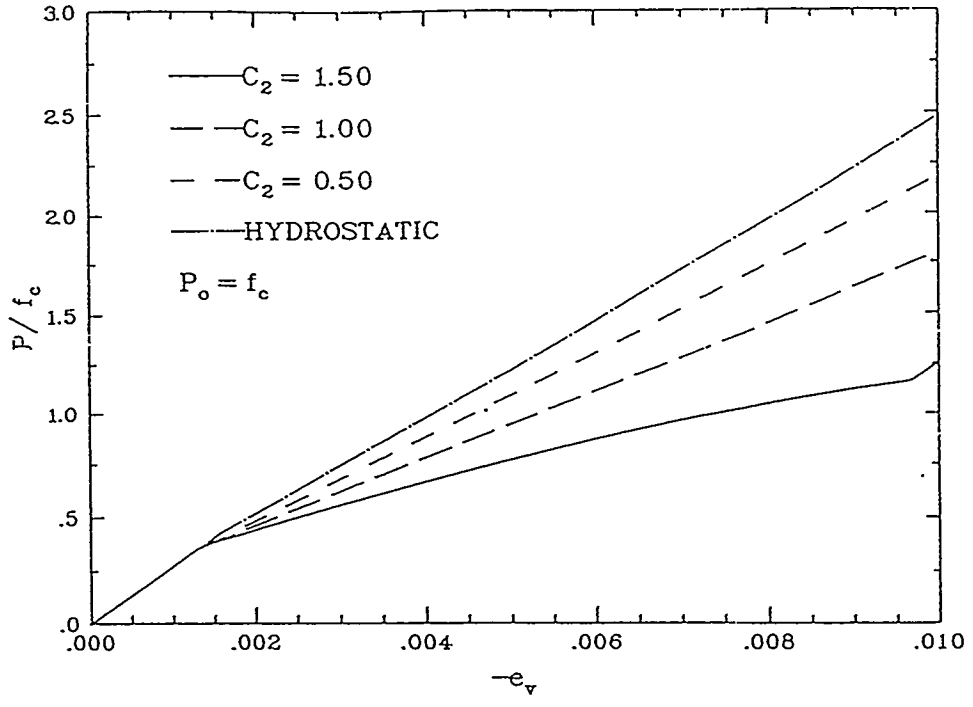

(c) Mean pressure versus volumetric strain for hydrostatic compression and uniaxial strain

Figure 6-10. (continued) The effect of the parameter C_2 on shear enhanced compaction.

values of material parameters for a high-strength concrete obtained by matching data are given as follows:

$\alpha = 0.50$	$\beta = 1.5$	$P_t = -200$	$m = 0.75$
$S_m = 25 f_c$	$P_{co} = \frac{3}{7} f_c$	$q = 0.30$	$c_1 = 0.60$
$c_2 = 0.50$	$c_3 = 5.0$	$c_4 = 1.0$	$P_0 = \frac{4}{7} f_c$
$\bar{e}_L^i = 0.0027$	$n = 0.25$	$H_0 = 0.50$	$f_c = 7000\,psi$

The fit for triaxial paths is shown in Figure 6-11 for three values of confining pressure. As can be seen, reasonable values of both stress and strain are predicted at the limit state except for Figure 6-11(b) where the confining pressure is *1000 psi* and the predicted limit stress is approximately *10 %* higher than tested.

For frequently used strain driven algorithms such as Algorithms 1 to 4, the lack of an accurate constitutive model will be reflected as errors in both stress and strain, especially near the limit state. For problems where estimates of load capability are of primary concern, such errors can result in misleading conclusions even though the computational algorithm is adequate. Hence, it is imperative that constitutive models provide reasonable fits to both stress and strain if the models are to be useful. From a micromechanical point of view, the

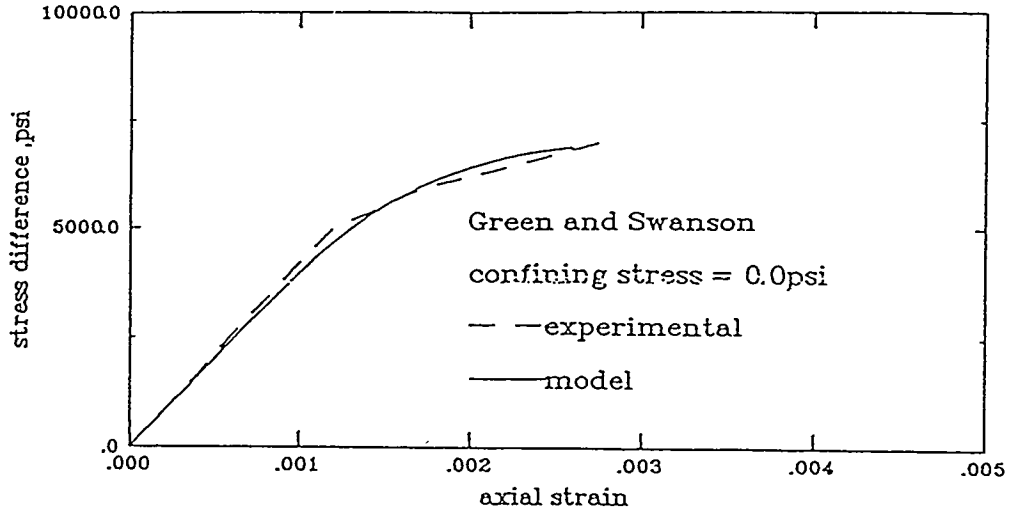

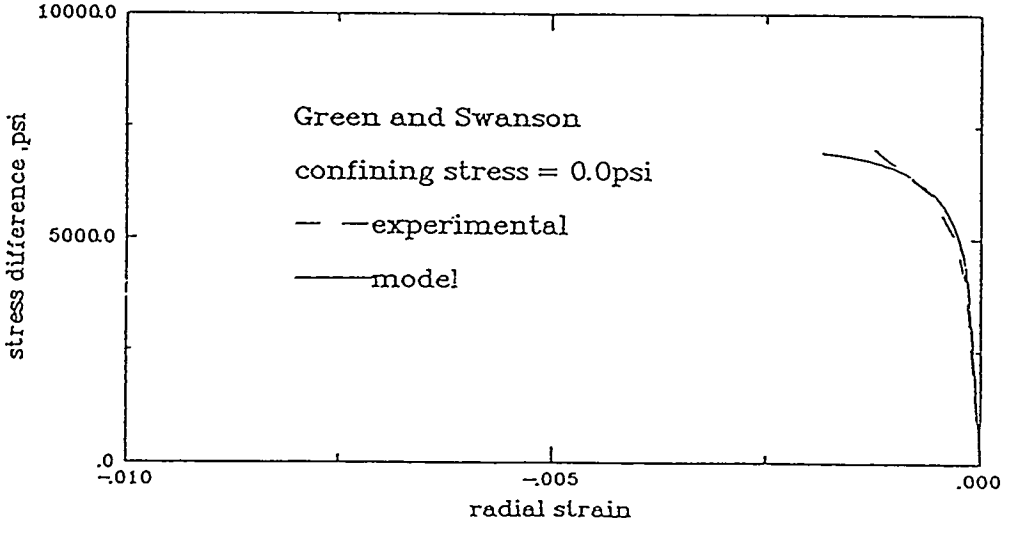

(a) Confining stress = 0.0 psi

Figure 6-11. Comparison of experimental [Green and Swanson, 1973] and theoretical curves of stress versus strain for triaxial paths.

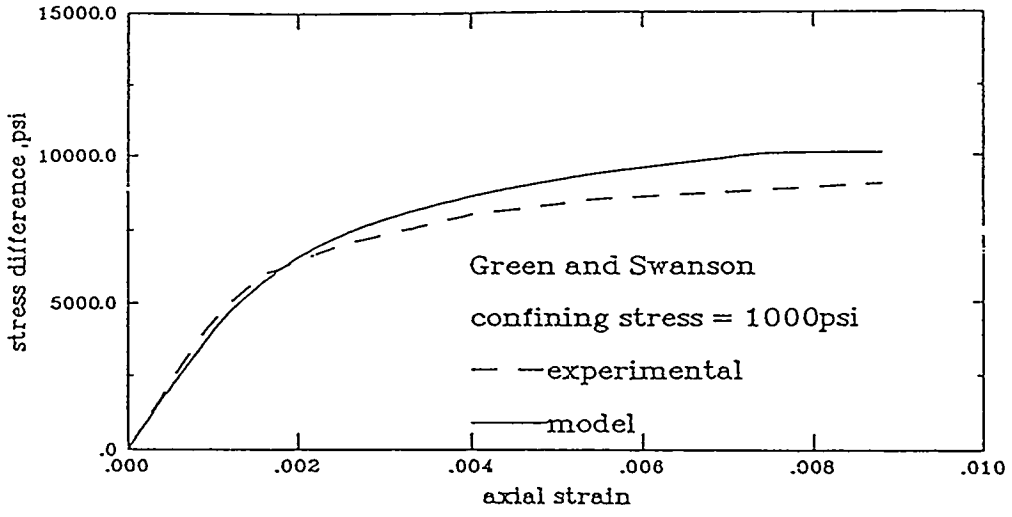

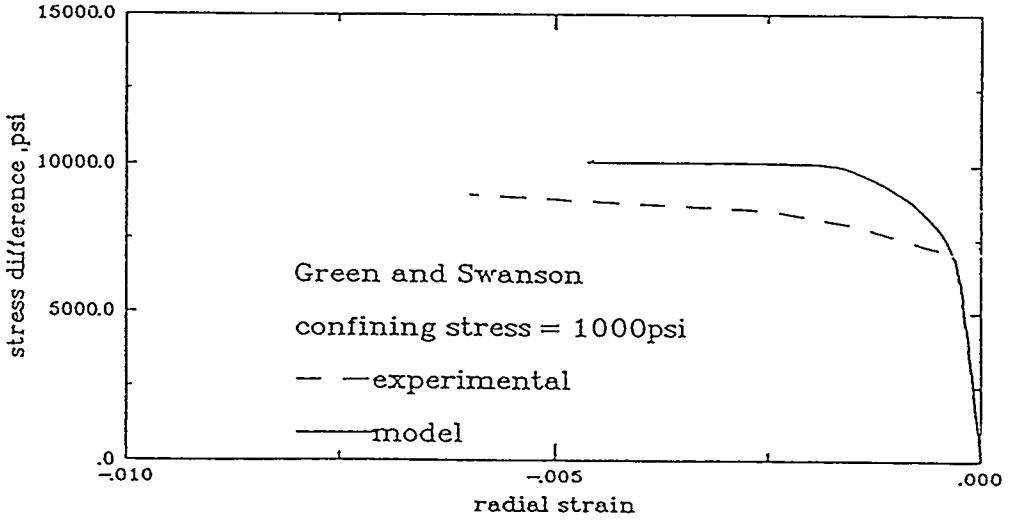

(b) Confining stress = 1000 psi

Figure 6-11. Comparison of experimental [Green and Swanson, 1973] and theoretical curves of stress versus strain for triaxial paths.

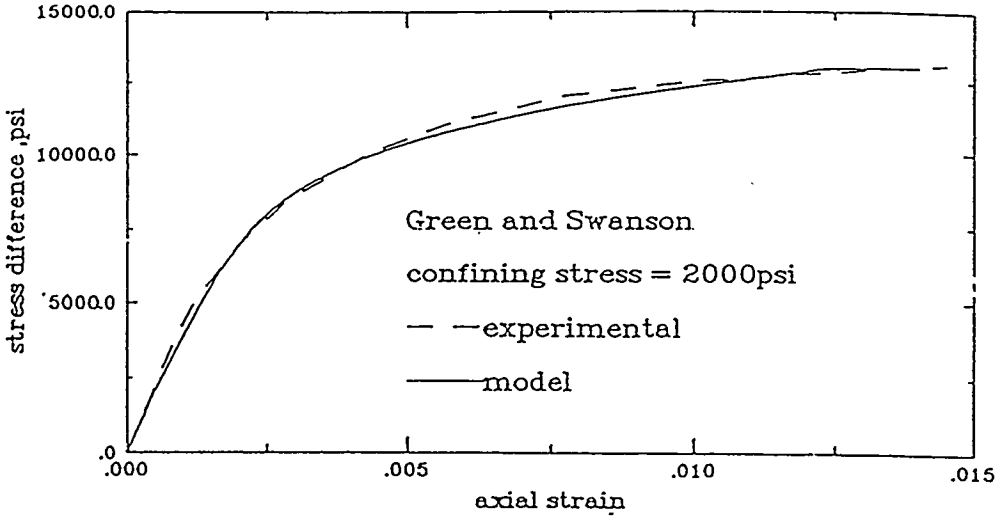

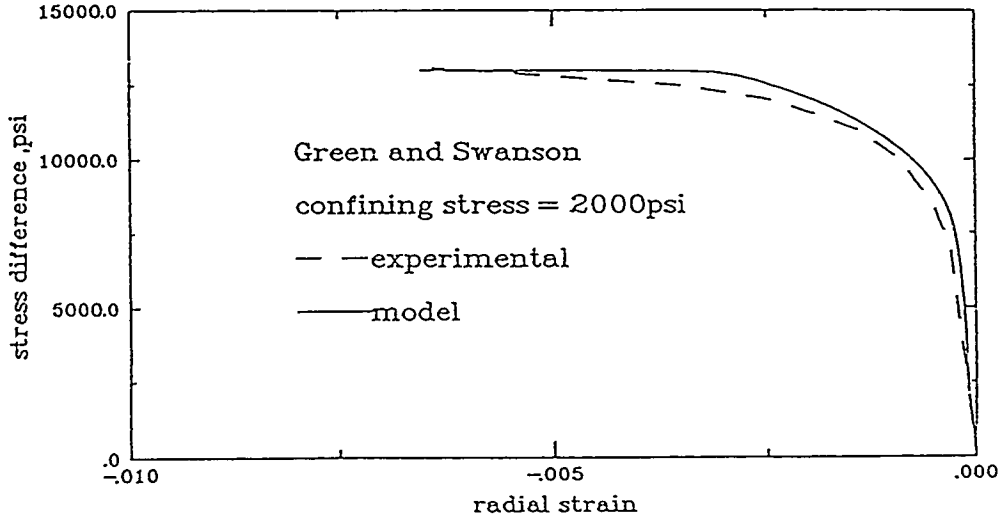

(c) Confining stress = 2000 psi

Figure 6-11. Comparison of experimental [Green and Swanson, 1973] and theoretical curves of stress versus strain for triaxial paths.

mechanism of inelastic flow alone can not provide a satisfactory specification for nonlinear features of quasi-brittle materials, and instead, the damaging or degradation of material properties often dominates in the cases of quasi-brittle materials under mechanical, thermal, and chemical effects, such as creep, stress corrosion, and leakage of seals. Thus, both the inelastic and damage processes should be fully understood to correctly model quasi-brittle materials nonlinear stress-strain response. The rapidly evolving continuum damage mechanics will be discussed in the next two chapters with emphasis on concrete.

7. DAMAGE MECHANICS

The concept of elastic or yield strength design is commonly used in conventional engineering design procedures. The post-limit behavior of materials is not normally taken into account. The concept of elastic or yield strength design might not be suitable for many engineering applications. For dynamic cases of very short load duration, such as explosive or seismic disturbances, no collapse occurs if a limit point is reached for a particular structural member. The response can be observed well beyond the limit point for a situation involving stress corrosion. Statically indeterminate structural members may help to preclude collapse. Since a significant amount of energy absorption can be associated with the post-limit regime, a realistic assessment of the nonlinear behavior of engineering structures must include the softening of material strength and stiffness in the post-limit regime. The post-limit response has become an active research field in recent years with increased need in environmental protection, space technology, and advanced engineering materials. Novel experimental techniques such as Laser Holographic Interferometry, X-Ray Radiography, and Image Analysis provide more details about microstructural features of materials, while the rapid development of digital computers makes advanced constitutive modeling more feasible than ever before.

Among continuous and discontinuous approaches in failure simulation, continuum damage mechanics (CDM) has been introduced and employed extensively to describe the progressive damaging experienced by material properties prior to the initiation of macrocracks. The historical development of the CDM dates back only about thirty years and has already been compiled in the literature [Kachanov, 1986; Krajcinovic, 1989; Lemaitre, 1984; Simo and Ju, 1987]. The CDM was originally applied to model creep rupture by using the concept of effective stress, and then developed to simulate the three main kinds of damage: fatigue damage, creep damage, and ductile damage. Recently, the CDM has found its place in describing micromechanics of failure of quasi-brittle materials such as concrete and rock, and the preliminary results appear quite promising. In the following sections, an up-to-date survey of failure simulation will be given based on experimental, theoretical, and computational points of view, and then the general formulation of damage models and corresponding numerical solution schemes will be discussed with emphasis on concrete.

7.1 Present Status of Failure Simulation

By means of carefully controlled experimental devices, phenomenological experimental data beyond the peak strength have been documented for some quasi-brittle materials such as concrete and rock [Van Mier, 1984; Shah and Gopalaratnam, 1985; Norman, 1990]. The apparent features characterized by the post-peak response include reductions of strength and stiffness accompanied by a small zone of large deformations, called softening with localization. At present, experimental investigations are providing micromechanical data from Laser Holographic Interferometry, X-Ray Radiography and Image Analysis [Maji et al., 1990; Wang et al., 1990]. The major difficulty associated with measuring the post-peak response is the sudden change from an original homogeneous deformation field to an inhomogeneous field where large deformations are localized into a thin band. Thus, it is difficult to derive the stress-strain relation in the post-peak regime directly from the normal force-displacement tests. It has been and is still a challenge to reduce the experimental data from highly inhomogeneous deformation fields in three-dimension to data suitable for evaluating constitutive equations

Two approaches exist to simulate structural failures: a discontinuous approach, such as linear elastic fracture mechanics and elastoplastic fracture mechanics, and a continuous approach, such as plasticity and damage mechanics. The discontinuous approach causes the problem requiring the remeshing in finite element calculations, while the continuous approach might not be valid when a macrocrack occurs. Also, the governing equations with rate-independent local softening models change from hyperbolic to elliptic equations for dynamic problems, and lose ellipticity for static problems. That is to say, the governing equations become ill-posed during the transition from the pre-peak to post-peak regime. Many research efforts have been conducted to clarify theoretical arguments associated with softening with localization, to make clear the relation between the evolution of localization zone and the post-peak response, and to simulate the degradation of material properties and localized failure modes [Bazant and Pijaudier-Cabot, 1988; Chen and Tzou, 1990; Chen and Schreyer, 1987; Chen, 1989; Chen and Schreyer, 1990; Costin and Stone, 1987; Ortiz, 1987; Schreyer and Chen, 1986; Schreyer and Wang, 1990; Taylor and Chen, 1986; Wawersik et al., 1990; Yazdani and Schreyer, 1990]. Among the models proposed are nonlocal plasticity, local or nonlocal continuum damage and other micromechanical models based on fracture mechanics. Preliminary results obtained for one- and two-dimensional sample problems look quite promising because, if a nonlocal model is used, the failure behavior of quasi-brittle materials can be simulated and the results are mesh independent. The correct predictions of crack propagation, anisotropy, and dynamic failure response, however, are still at an infant stage due to the extreme complexity of the

microstructural features of materials. Applications to the three-dimensional cases will not be feasible until a robust and efficient solution scheme is designed, even with the use of supercomputers.

As can be seen from the literature, an overwhelming number of models simulating engineering materials has been suggested. The development of sophisticated constitutive models itself might not be the limiting factor in structural analyses. Rather, a lack of suitable experimental data to identify material parameters and an inability to obtain a converged solution in nonlinear numerical analysis pose the major limitations. A robust solution scheme is a necessity for a model to be used in industry, but little attention has been paid to the numerical aspect of failure simulation. In nonlinear analyses, an incremental-iterative procedure is commonly employed to correct for the incremental linearization error. From the differential form of the stress-strain relation, it is a natural consequence to use the tangent instead of the secant tensor. The convergence behavior of the incremental-iterative scheme then depends heavily on the condition number of the tangent structural stiffness matrix. If the tangent stiffness matrix becomes ill-conditioned, the numerical solution will converge very slowly or even fail at some point on the solution path [Akinson, 1978; Bathe, 1982], especially, if bifurcation or limit points, which are typical of failure simulation, exist. In addition to an ill-conditioned tangent stiffness matrix, the load increment can not be directly prescribed if the right path in the post-peak regime is to be traced. From bifurcation analysis, it can be shown that more than one solution exists at a bifurcation point. Hence, a suitable constraint condition should be imposed to guide the solution path in the right direction. In other words, the post-peak solution heavily relies on the constraint condition. After reviewing existing solution procedures, failure-controlled solution strategies have been proposed for damage softening with localization and extended to include both incremental plasticity and damage with nonlocal features [Chen and Schreyer, 1989 and 1990; Chen et al., 1992; Neilsen et al., 1991]. The basic idea is that a secant instead of tangent stiffness matrix, that is derived based on plasticity and damage secant stiffness tensors, is used in the structural solution scheme controlled by a suitable measure of failure. The resulting procedure is very robust for simulating the post-peak response including snap-back and snap-through. Since practical finite element analyses usually require the use of elements that are much larger than the localization zone, an element constitutive relation is designed to describe the behavior of a finite element with a localized deformation region that is smaller than the element itself. The applicability of the proposed solution strategies in the general case needs to be further investigated.

In summary, more results have been achieved in failure simulation within the recent ten years than ever before. A thorough understanding of failure mechanism and the routine use of failure simulation in industry need a combined effort from experimental, theoretical,

and computational aspects. From a modeling point of view, it is useful to combine both plasticity and damage mechanics to simulate two distinct modes of microstructural changes of material: inelastic flow and the degradation of material properties.

7.2 General Formulation

Phenomenological and micromechanical approaches are two ways of formulating the damage models. There is no question that a meaningful constitutive model must be consistent with the micromechanics of the material considered. However, the detailed discussion of micromechanical features is well beyond the scope of the report, and instead, the restrictions of thermodynamics, which reflect fundamental laws of physics [Coleman and Noll, 1963; Coleman and Gurtin, 1967; Malvern, 1969; Marsden and Hughes, 1983; Truesdell, 1984], are imposed here on the development of constitutive models. The general formulations of both damage and inelasticity models follow the same procedure based on the internal variable theory of thermodynamics. However, more details will be given in this chapter to continuum damage models, which are proposed for simulating the progressive weakening of solids as reflected through the reduction of material stiffness. The part on inelasticity is provided for the purpose of showing an alternative method in formulating the inelastic hardening models discussed previously. It is assumed, as before, that the deformation and deformation gradients are small, so that the proposed damage models can be applicable up to the immediate post-peak regime.

For a purely mechanical case, there exists an internal energy per unit volume, $U(\boldsymbol{\varepsilon}, I_i)$, or a Gibbs free energy per unit volume, $G(\boldsymbol{\sigma}, I_i)$, where I_i ($i = 1,2,...,n$) are the internal variables representing the internal constitution of a material and hence governing the processes of inelastic flow and degradation of material properties. Additional independent variables can be introduced if the effects of thermal and chemical diffusion processes are considered. The Clausius-Duhem inequality that follows from the principles of thermodynamics can be expressed in terms of either the internal energy:

$$-\dot{U}(\boldsymbol{\varepsilon}, I_i) + \boldsymbol{\sigma}:\dot{\boldsymbol{\varepsilon}} \geq \boldsymbol{0} \tag{7.1}$$

or the Gibbs free energy:

$$\dot{G}(\boldsymbol{\sigma}, I_i) - \boldsymbol{\varepsilon}:\dot{\boldsymbol{\sigma}} \geq \boldsymbol{0} \tag{7.2}$$

for any admissible process. Equation (7.1) will lead to a strain-based formulation, while Eq. (7.2), a stress-based formulation. If the displacement-based finite element method [Bathe, 1982; Belytschko, 1983] is adopted for the semidiscretization in space, the strain-based Clausius-Duhem inequality in Eq. (7.1) has a computational advantage over the stress-based one in Eq. (7.2), although both formulations are related to each other, as will be explained later. Hence, Eq. (7.1) will be used in the formulation of a strain-based damage model, which is fairly simple and provides a computational advantage of reduced drifting errors from a damage surface.

From the definition of the internal energy, an alternative form of Eq. (7.1) is given by

$$\left(\boldsymbol{\sigma}-\frac{\partial U}{\partial \boldsymbol{\varepsilon}}\right):\dot{\boldsymbol{\varepsilon}}-\sum_{i=1}^{n}\frac{\partial U}{\partial I_i}\dot{I}_i\geq 0 \tag{7.3}$$

Standard arguments [Coleman and Noll, 1963; Coleman and Gurtin, 1967] and the assumption that inelastic and damage unloading processes are elastic result in

$$\boldsymbol{\sigma}=\frac{\partial U}{\partial \boldsymbol{\varepsilon}} \tag{7.4}$$

and the dissipative inequalities

$$-\frac{\partial U}{\partial I_i}\dot{I}_i\geq 0 \qquad i=1, 2, ..., n \tag{7.5}$$

Generally speaking, both inelastic flow and damaging processes are interacting, but at present a coupled theory would not be useful because of no physical or experimental support [Yazdani and Schreyer, 1990]. Therefore, a decoupled theory is developed here by assuming

$$U(\boldsymbol{\varepsilon}, I_i)=U^e(\boldsymbol{\varepsilon})+U^d(\boldsymbol{\varepsilon}, I_j)+U^i(\boldsymbol{\varepsilon}, I_k) \tag{7.6}$$
$$j=1, 2,..., l \qquad k=1, 2,...,m \quad l+m=n$$

where U^e, U^d, and U^i are related to the elastic, damage, and inelastic processes with corresponding internal variables, respectively. According to the features of these different processes, we can postulate the following forms:

$$U^e = \frac{1}{2}\boldsymbol{\varepsilon}:\boldsymbol{E}^e:\boldsymbol{\varepsilon} \tag{7.7-1}$$

$$U^d = \frac{1}{2}\boldsymbol{\varepsilon}:\boldsymbol{E}^d\left(I_j\right):\boldsymbol{\varepsilon} \tag{7.7-2}$$

$$U^i = \boldsymbol{\varepsilon}:\boldsymbol{\sigma}^i\left(I_k\right) \tag{7.7-3}$$

where $\boldsymbol{E}^e$ and $\boldsymbol{E}^d$ are secant stiffness tensors for the elastic and damage processes, respectively. They can be isotropic or anisotropic but possess inherent symmetry due to the definition of the internal energy. σ^i is the inelastic (relaxation) stress tensor.

Combining Eqs. (7.4), (7.6), and (7.7) yields the following expression for the total stress tensor:

$$\begin{aligned}\boldsymbol{\sigma} &= \frac{\partial U}{\partial \boldsymbol{\varepsilon}} = \boldsymbol{E}^e:\boldsymbol{\varepsilon} + \boldsymbol{E}^d:\boldsymbol{\varepsilon} + \boldsymbol{\sigma}^i = \boldsymbol{\sigma}^e + \boldsymbol{\sigma}^d + \boldsymbol{\sigma}^i \\ &= \boldsymbol{E}^{ed}:\boldsymbol{\varepsilon} + \boldsymbol{\sigma}^i\end{aligned} \tag{7.8}$$

where $\boldsymbol{E}^{ed}$ is the secant elastodamage stiffness tensor that is related to the internal energy through

$$\boldsymbol{E}^{ed} = \boldsymbol{E}^e + \boldsymbol{E}^d = \frac{\partial^2 U}{\partial \boldsymbol{\varepsilon}\partial \boldsymbol{\varepsilon}} \tag{7.9}$$

σ^e, σ^d, and σ^i are the elastic, damage, and inelastic parts of the total stress tensor, respectively, which is similar to the decomposition of the total strain tensor. The inelastic strain and inelastic stress have the relation that

$$\boldsymbol{\varepsilon}^i = -\left(\boldsymbol{E}^{ed}\right)^{-1}:\boldsymbol{\sigma}^i \tag{7.10}$$

since the inelastic parts are assumed to be fixed during elastic unloading.

From the dissipative inequalities in Eq. (7.5) and Eqs. (7.7), it follows that

$$-\frac{1}{2}\boldsymbol{\varepsilon}:\dot{\boldsymbol{E}}^d:\boldsymbol{\varepsilon} \geq 0 \tag{7.11-1}$$

$$-\boldsymbol{\varepsilon}:\dot{\boldsymbol{\sigma}}^i \geq 0 \tag{7.11-2}$$

Suppose the damage stiffness and inelastic stress tensors are described through the evolution equations:

$$\dot{E}^d = -\sum_{j=1}^{l} \dot{I}_j R_j \tag{7.12-1}$$

$$\dot{\sigma}^i = -\sum_{k=1}^{m} \dot{I}_k r_k \tag{7.12-2}$$

Then for the damage part of a constitutive model, there exists a damage surface that can be formulated via

$$f^d(\varepsilon, I_j) = \frac{1}{2}\sum_{j=1}^{l} \varepsilon : R_j : \varepsilon - S^2(I_j) \tag{7.13}$$

where S is called the damage hardening-softening function. Because the damage process is irreversible, namely, $\dot{I}_j \geq 0$, the tensor R_j must be positive definite so that the inequality (7.11-1) is satisfied. It should be pointed out that the theory of thermodynamics does not produce a constitutive model, and instead, only imposes certain constraint conditions on the functional forms of constitutive equations we define. The internal variables, I_j, are determined by a suitable set of damage hardening-softening rules:

$$dI_j = d\lambda^d s_j(\varepsilon, I_j) \tag{7.14}$$

in which λ^d is a monotonically increasing variable used to parameterize the evolution of damage. In order to obtain the differential $d\lambda^d$, the loading/unloading criteria for the damage process must be defined as

$$f^d \leq 0, \qquad d\lambda^d \geq 0, \qquad d\lambda^d f^d \equiv 0 \tag{7.15}$$

In other words, damage occurs only when the strain is such that the damage surface $f^d = 0$, which guarantees the satisfaction of the thermodynamic restrictions. Thus, $d\lambda^d$ can be found from the damage consistency condition: $df^d = 0$, i.e.,

$$d\lambda^d = -\frac{\frac{\partial f^d}{\partial \varepsilon} : d\varepsilon}{\sum_j \frac{\partial f^d}{\partial I_j} s_j} = -\frac{\sum_j \varepsilon : R_j : d\varepsilon}{\sum_j \frac{\partial f^d}{\partial I_j} s_j} \tag{7.16}$$

In the absence of inelastic flow, therefore, the strain-based constitutive equations for elastodamage process can be written in the differential form as follows:

$$d\boldsymbol{\sigma} = d\boldsymbol{\sigma}^e + d\boldsymbol{\sigma}^d \tag{7.17-1}$$

$$d\boldsymbol{\sigma}^e = \boldsymbol{E}^e : d\boldsymbol{\varepsilon} \tag{7.17-2}$$

$$d\boldsymbol{\sigma}^d = d\left(\boldsymbol{E}^d : \boldsymbol{\varepsilon}\right) \tag{7.17-3}$$

$$dI_j = d\lambda^d s_j \tag{7.17-4}$$

$$df^d\left(\boldsymbol{\varepsilon}, I_j\right) = 0 \tag{7.17-5}$$

For given increments in the total strain tensor, the internal variables, the elastic part of the total stress tensor, and the damage part of the total stress tensor can be obtained with the use of the loading/unloading criteria defined by Eq. (7.15). The difference between different damage models depends on the specific damage surface in Eq. (7.13), damage flow rule in Eq. (7.17-3), and hardening-softening rules in Eq. (7.14). The damage flow rule and the evolution equation (7.12-1) are related to each other (i.e., either the flow rule or the evolution equation can be specified independently).

For damage problems, it is a natural consequence to use the secant tensor, $\boldsymbol{E}^{ed}$, in computation to construct a structural stiffness matrix because of the explicit formulation of Eq. (7.8) with $\sigma^i = 0$,

$$\boldsymbol{\sigma} = \boldsymbol{E}^{ed} : \boldsymbol{\varepsilon} \tag{7.18}$$

It is not difficult to derive a corresponding tangent tensor, $\boldsymbol{T}^{ed}$, because it follows from Eqs. (7.9) and (7.18) that

$$d\boldsymbol{\sigma} = \boldsymbol{E}^{ed} : d\boldsymbol{\varepsilon} + d\boldsymbol{E}^d : \boldsymbol{\varepsilon} \tag{7.19}$$

The use of Eqs. (7.12-1), (7.14), and (7.16) yields

$$\boldsymbol{T}^{ed} = \boldsymbol{E}^{ed} + \frac{\left(\sum_j s_j \boldsymbol{R}_j\right) : \boldsymbol{\varepsilon} \otimes \boldsymbol{\varepsilon} : \left(\sum_j \boldsymbol{R}_j\right)}{\sum_j \frac{\partial f^d}{\partial I_j} s_j} \tag{7.20}$$

so that

$$d\boldsymbol{\sigma} = \boldsymbol{T}^{ed} : d\boldsymbol{\varepsilon} \tag{7.21}$$

Thus, a solution scheme can make use of either the tangent or secant tensor, although the constitutive equations remain in the differential forms shown in Eqs. (7.17) to simulate those paths that are load dependent with the least possible computer resources. The use of the secant tensor, however, avoids the singularity associated with the limit or bifurcation points [Chen and Schreyer, 1990].

For the inelastic part of a constitutive model, equations similar to those in Eqs. (7.17) can be constructed by using the above procedure. However, a secant tensor for the inelastic part can not be directly obtained as for the damage part, and instead, an alternative formulation must be invoked [Chen et al., 1992].

As mentioned before, the stress-based formulation for damage and inelasticity models can be derived from Eq. (7.2). Now let us find the counterpart of Eqs. (7.17) so that both the strain- and stress-based formulations can be compared with regard to their effectiveness in numerical calculations. According to the definition of the Gibbs free energy and with the use of Eq. (7.2) and standard arguments, we arrive at

$$\varepsilon = \frac{\partial G}{\partial \sigma} \tag{7.22}$$

and the dissipative inequalities

$$\frac{\partial G}{\partial I_i} \dot{I}_i \geq 0 \qquad i = 1,2,...,n \tag{7.23}$$

A stress-based decoupled theory can be developed by assuming

$$G(\sigma, I_i) = G^e(\varepsilon) + G^d(\varepsilon, I_j) + G^i(\varepsilon, I_k) \tag{7.24}$$
$$j = 1, 2,..., l \qquad k = 1, 2,..., m \qquad l + m = n$$

where G^e, G^d, and G^i correspond to the elastic, damage, and inelastic processes with corresponding internal variables, respectively. Based on the features typical of the elastic, damage, and inelastic processes, respectively, it can be postulated that

$$G^e = \frac{1}{2}\sigma : C^e : \sigma \tag{7.25-1}$$

$$G^d = \frac{1}{2}\sigma : C^d : \sigma \tag{7.25-2}$$

$$G^i = \sigma : \varepsilon^i \tag{7.25-3}$$

where C^e and C^d are secant compliance tensors for elastic and damage processes, respectively.

Combining Eqs. (7.22), (7.24), and (7.25) results in the following expression for the total strain tensor:

$$\begin{aligned}\varepsilon &= \frac{\partial G}{\partial \sigma} = C^e : \sigma + C^d : \sigma + \varepsilon^i \\ &= \varepsilon^e + \varepsilon^d + \varepsilon^i = C^{ed} : \sigma + \varepsilon^i\end{aligned} \tag{7.26}$$

where C^{ed} is the secant elastodamage compliance tensor that is related to the Gibbs free energy through

$$C^{ed} = C^e + C^d = \frac{\partial^2 G}{\partial \sigma \partial \sigma} \tag{7.27}$$

ε^e, ε^d, and ε^i are the elastic, damage, and inelastic parts of the total strain tensor, respectively.

According to the dissipative inequalities in Eq. (7.23) and Eqs. (7.25), it follows that

$$\frac{1}{2}\sigma : \dot{C}^d : \sigma \geq 0 \tag{7.28-1}$$

$$\sigma : \dot{\varepsilon}^i \geq 0 \tag{7.28-2}$$

The evolution equations or flow rules need to be defined for the damage compliance and inelastic strain tensors, namely,

$$\dot{C}^d = \sum_{j=1}^{l} \dot{l}_j \bar{R}_j \tag{7.29-1}$$

$$\dot{\varepsilon}^i = \sum_{k=1}^{m} \dot{l}_k \bar{r}_k \tag{7.29-2}$$

Then for the damage part of a constitutive model, we can construct a damage surface by letting

$$\bar{f}^d(\sigma, I_j) = \frac{1}{2}\sum_j \sigma : \bar{R}_j : \sigma - \bar{S}^2(I_j) \tag{7.30}$$

where $\bar{S}$ is the counterpart of the damage hardening-softening function in the strain-based formulation, and the tensor, $\bar{R}_j$, must be positive definite so that the inequality (7.28-1) is satisfied. The internal variables, I_j, are determined by a suitable set of damage hardening-softening rules:

$$dI_j = d\bar{\lambda}^d \bar{s}_j(\boldsymbol{\sigma}, I_j) \tag{7.31}$$

In order to find the positive parameter $d\bar{\lambda}^d$, the damage loading/unloading criteria in Eq. (7.15) must be invoked, and then the resulting damage consistency condition yields

$$d\bar{\lambda}^d = -\frac{\sum_j \boldsymbol{\sigma} : \bar{\boldsymbol{R}}_j : d\boldsymbol{\sigma}}{\sum_j \frac{\partial \bar{f}^d}{\partial I_j} \bar{s}_j} \tag{7.32}$$

The stress-based constitutive equations for elastodamage process can be summarized in the differential form in the absence of inelastic flow as follows:

$$d\boldsymbol{\varepsilon} = d\boldsymbol{\varepsilon}^e + d\boldsymbol{\varepsilon}^d \tag{7.33-1}$$
$$d\boldsymbol{\sigma} = \boldsymbol{E}^e : d\boldsymbol{\varepsilon}^e \tag{7.33-2}$$
$$d\boldsymbol{\varepsilon}^d = d\left(\boldsymbol{C}^d : \boldsymbol{\sigma}\right) \tag{7.33-3}$$
$$dI_j = d\bar{\lambda}^d \bar{s}_j \tag{7.33-4}$$
$$d\bar{f}^d(\boldsymbol{\sigma}, I_j) = 0 \tag{7.33-5}$$

and the corresponding tangent compliance tensor is given by

$$\bar{\boldsymbol{T}}^{ed} = \boldsymbol{C}^{ed} - \frac{\left(\sum_j s_j \bar{\boldsymbol{R}}_j\right) : \boldsymbol{\sigma} \otimes \boldsymbol{\sigma} : \left(\sum_j \bar{\boldsymbol{R}}_j\right)}{\sum_j \frac{\partial \bar{f}^d}{\partial I_j} s_j} \tag{7.34}$$

For the inelastic part of a constitutive model, results similar to Eqs. (7.33) can be obtained.

In summary, any damage and inelasticity models can be developed from either the strain- or stress-based general formulation constrained by thermodynamic restrictions. Both the strain- and stress-based formulations are related to and can be easily transformed to

each other, but the model derived from the strain-based formulation is computationally more efficient as shown in the next section.

7.3 Constitutive Equation Solver

As in the case of inelasticity models, damage models are usually nonlinear, and hence an incremental-iterative integration scheme is required to solve the differential constitutive equations. Because Eqs. (7.33) are the same as Eqs. (4.11), the integration schemes discussed in Chapter 4 can also be applied to the case of stress-based damage models, with only minor adaptations for damage variables. However, the integration schemes for the strain-based formulation can be made much simpler and introduce less numerical errors than for the stress-based one. The increment $\Delta\lambda^d$ can be found for given total strain increments by using either the Newton-Raphson or secant method. No elastic-predictor and damage-corrector are needed as in the stress-based formulation. The following is the outline of an integration scheme suitable for the strain-based damage model, based on Eqs. (7.17) and (7.18).

Algorithm 5.

For each increment Δt, the states of total strain, elastic stress, damage stress, and internal variables at the end of the previous increment are known and denoted with the subscript n -1, and the current total strain, ε_n, is prescribed. The iteration loop for solving $\Delta\lambda^d$ is identified with the index k. The final values of state variables at the end of current increment are denoted with the subscript n.

Step 1

Evaluate the damage surface $f_o^d = f^d\left[\boldsymbol{\varepsilon}_n, \left(I_j\right)_{n-1}\right]$ and check the damage loading/ unloading criterion:

If $f_o^d > 0$, then go to step 3. Otherwise, the solution is elastic.

Step 2

Update the elastic stress and damage stress at the end of current increment:

$$\boldsymbol{\sigma}_n = \left(\boldsymbol{E}^{ed}\right)_n : \boldsymbol{\varepsilon}_n$$

$$\boldsymbol{\sigma}_n^e = \boldsymbol{E}^e : \boldsymbol{\varepsilon}_n$$

$$\boldsymbol{\sigma}_n^d = \boldsymbol{\sigma}_n - \boldsymbol{\sigma}_n^e$$

where $\boldsymbol{E}^{ed}$ and $\boldsymbol{E}^e$ are the elastodamage and elastic stiffness tensors, respectively.

Exit or go to Step 1 for the next increment.

Step 3

Damage occurs and solve $f^d\left[\boldsymbol{\varepsilon}_n, \left(I_j\right)_k\right] = 0$ for λ_k^d by using either the Newton-Raphson or secant method. Go to Step 2 after a converged solution is achieved.

For a simple case given in Chapter 8, λ_n^d can be solved correctly without invoking Step 3 in the above algorithm. Thus, a very robust constitutive equation solver can be incorporated into commonly used structural solution codes.

8. DAMAGE MODELS

Experimental results [Wang et al., 1990] indicate that internal strain localization starts as early as 40% of the peak load for some concrete specimens, which implies that the degradation of material properties might occur well before the peak strength is reached. Thus, a damage model should be able to include both hardening and softening regimes, although inelastic flow might dominate the hardening phenomenon. Here, the emphasis will be put on the development of damage softening models, but the extension to the hardening part is straightforward as shown with an example.

If the elastodamage process is assumed to be isotropic, the elastodamage stiffness tensor can be expressed in terms of bulk and shear moduli, $B^{ed}(I_j)$ and $G^{ed}(I_j)$, respectively, and takes the form of

$$\boldsymbol{E}^{ed}(I_j) = 3B^{ed}(I_j)\boldsymbol{P}^s + 2G^{ed}(I_j)\boldsymbol{P}^d \tag{8.1-1}$$

with its initial value equal to the elastic stiffness tensor, namely,

$$\boldsymbol{E}^{ed}(0) = \boldsymbol{E}^e = 3B^e\boldsymbol{P}^s + 2G^e\boldsymbol{P}^d \tag{8.1-2}$$

and its damage part defined by

$$\boldsymbol{E}^d(I_j) = 3B^d(I_j)\boldsymbol{P}^s + 2G^d(I_j)\boldsymbol{P}^d \tag{8.1-3}$$

The corresponding elastodamage compliance tensor is given by

$$\boldsymbol{C}^{ed}(I_j) = \left(\boldsymbol{E}^{ed}\right)^{-1} = \frac{1}{3B^{ed}(I_j)}\boldsymbol{P}^s + \frac{1}{2G^{ed}(I_j)}\boldsymbol{P}^d \tag{8.2-1}$$

with

$$\boldsymbol{C}^{ed}(0) = \boldsymbol{C}^e = \left(\boldsymbol{E}^e\right)^{-1} = \frac{1}{3B^e}\boldsymbol{P}^s + \frac{1}{2G^e}\boldsymbol{P}^d \tag{8.2-2}$$

$$\boldsymbol{C}^d(I_j) = \boldsymbol{C}^{ed}(I_j) - \boldsymbol{C}^e = \frac{B^e - B^{ed}(I_j)}{3B^{ed}(I_j)B^e}\boldsymbol{P}^s + \frac{G^e - G^{ed}(I_j)}{2G^{ed}(I_j)G^e}\boldsymbol{P}^d \tag{8.2-3}$$

For the purpose of illustration, isotropic damage models of the von Mises type are developed in the next two sections via both the strain- and stress-based formulations. Since the models are in the deviatoric space, failures of shear type are simulated and no damage occurs in the volumetric space.

8.1 A Strain-Based Model

A strain-based damage model in the deviatoric space can be defined as

$$f^d = \bar{\varepsilon}^2 - S^2 \tag{8.3-1}$$

$$\boldsymbol{E}^d = 2G^d\boldsymbol{P}^d = 2c_0G^e\left[exp(-c_1\omega) - I\right]\boldsymbol{P}^d \qquad 0 \le \omega < \infty \tag{8.3-2}$$

$$d\omega = d\lambda^d \tag{8.3-3}$$

where the effective strain (strain invariant) and damage hardening-softening function are given, respectively, by

$$\bar{\varepsilon}^2 = \frac{3}{2}\boldsymbol{\varepsilon}^d : \boldsymbol{\varepsilon}^d \tag{8.4-1}$$

$$S = S_L(1+\omega) \tag{8.4-2}$$

Since the stiffness tensor is determined for given evolution equations and hardening-softening rules, Eq. (8.3-2) implicitly gives the definitions for the evolution equations and hardening-softening rules, which illustrates an alternative approach to set up a damage model. Eq. (8.3-1) is consistent with Eq. (7.13) if $\boldsymbol{R}_1 = 3\boldsymbol{P}^d$. Due to the simple form of Eq. (8.3-1), it follows from a Taylor expansion that

$$\Delta\omega = \Delta\lambda^d = \frac{f^d_{t-\Delta t} + \Delta\bar{\varepsilon}}{S_L} \tag{8.5}$$

Since the total strain increments are provided directly from the displacement-based finite element method, Algorithm 5 discussed in Section 7.3 can be used without invoking the Newton-Raphason or secant method, and no drifting error will be induced for the given damage surface. This might not be the case, however, if a stress-based model is used because the total stress increments are usually unknown before a converged solution is achieved.

The effects of the model parameters c_0 and c_1 on the strain-based damage model are illustrated in Figure 8-1 with $S_L = 10^{-3}$, $B^e = 24\ GPa$, and $G^e = 18GPa$ which are representative of concrete. The effect of c_0 is demonstrated for $c_1 = 1$. As expected, the smaller the value of c_0, the larger the residual stiffness. The rate of change of G^d with damage is simulated through the value of c_1 and is shown for $c_0 = 0.99$. From the figure, it can be found that both damaging hardening and softening are exhibited with different values of model parameters.

8.2 A Stress-Based Model

In this section, a stress-based damage model is developed by showing its correspondence to a strain-based formulation so that both a strain- and a stress-based formulations can be available for a specific damage model, which provides experimental and computational convenience.

A stress-based damage surface of the von Mises type can be defined as

$$\bar{f}^d = \bar{\sigma}^2 - \bar{S}^2 \tag{8.6-1}$$

$$\bar{\sigma}^2 = \boldsymbol{\sigma}^d : \boldsymbol{\sigma}^d \tag{8.6-2}$$

where $\bar{\sigma}$ and $\bar{S}$ are the effective stress (stress invariant) and damage hardening-softening function, respectively. Because

$$\begin{aligned} \boldsymbol{\sigma}^d : \boldsymbol{\sigma}^d &= \boldsymbol{\sigma} : \boldsymbol{P}^d : \boldsymbol{P}^d : \boldsymbol{\sigma} = \boldsymbol{\varepsilon} : \boldsymbol{E}^{ed} : \boldsymbol{P}^d : \boldsymbol{E}^{ed} : \boldsymbol{\varepsilon} \\ &= 4\left(G^{ed}\right)^2 \boldsymbol{\varepsilon} : \boldsymbol{P}^d : \boldsymbol{\varepsilon} = 4\left(G^{ed}\right)^2 \boldsymbol{\varepsilon}^d : \boldsymbol{\varepsilon}^d \end{aligned} \tag{8.7}$$

the stress-based formulation (8.6-1) can be changed to a strain-based one as follows:

$$f^d = \boldsymbol{\varepsilon} : \boldsymbol{R} : \boldsymbol{\varepsilon} - S^2 \tag{8.8}$$

in which

$$\boldsymbol{R} = \frac{1}{2}\boldsymbol{P}^d \tag{8.9-1}$$

$$S^2 = \frac{\bar{S}^2}{4\left(G^{ed}\right)^2} \tag{8.9-2}$$

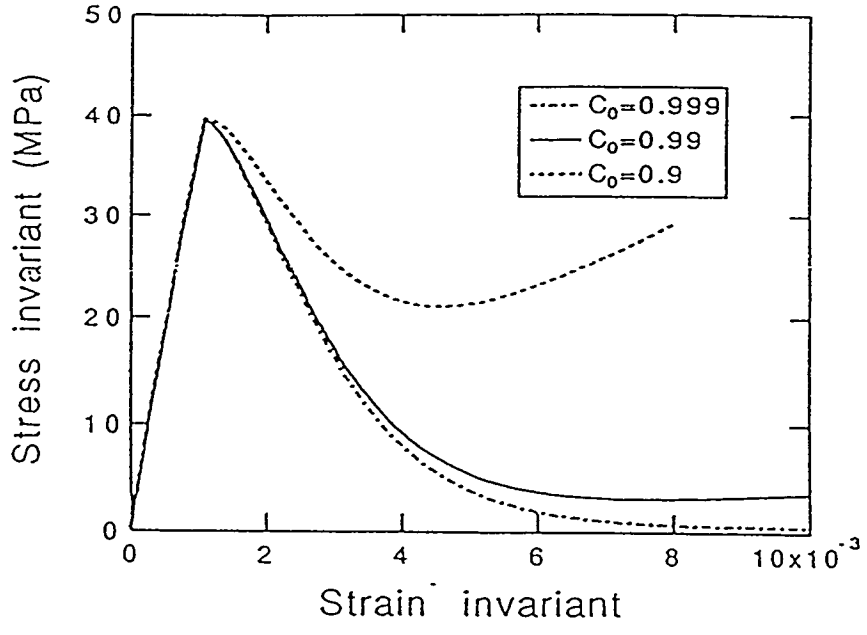

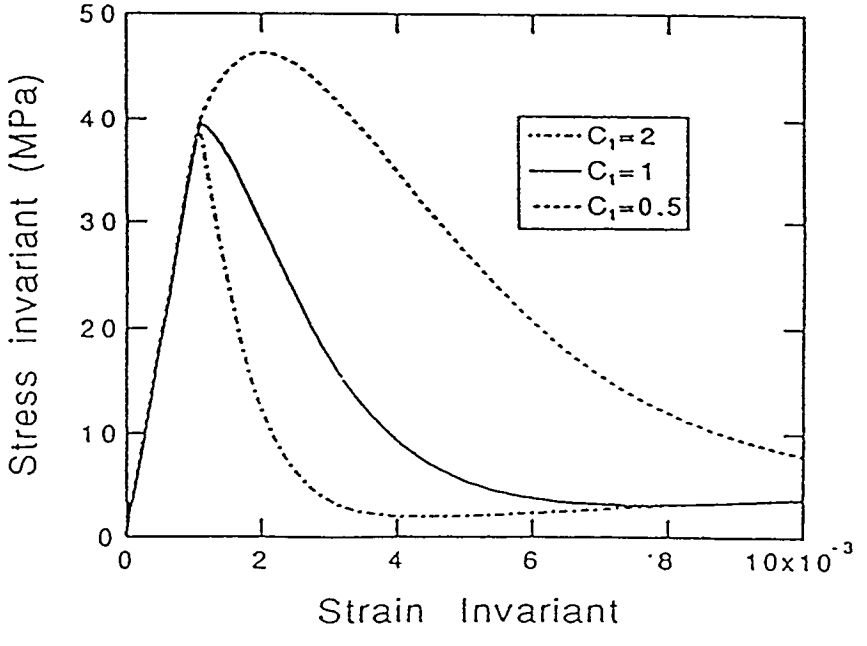

Figure 8-1. The effects of model parameters C_0 and C_1 on the stress-strain relation.

The strain-based damage surface in Eq. (8.8) is obtained by dividing Eq. (8.6-1) by $4\left(G^{ed}\right)^2$. The choice of $\boldsymbol{R}$ given in Eq. (8.9-1) is necessary for the equality of Eq. (8.8) to hold. If the numerator in Eq. (8.9-2) decreases faster than its denominator, the effective strain reduces with damage softening, a feature that might not be physically realistic.

With the use of one internal variable, I_1, a simple damage hardening-softening rule is given by

$$dI_1 = d\lambda^d \tag{8.10}$$

Then the use of Eqs. (7.12-1), (8.1-3), and (8.9-1) yields $B^d = 0$ and

$$2\dot{G}^d(I_1)\boldsymbol{P}^d = -\frac{\dot{I}_1}{2}\boldsymbol{P}^d \tag{8.11}$$

With the initial condition $G^d(0) = 0$, it follows that

$$G^d = -\frac{I_1}{4} \qquad 0 \le I_1 \le 4G^e \tag{8.12}$$

Thus, it can be found that

$$\boldsymbol{E}^{ed}(I_1) = 3B^e\boldsymbol{P}^s + 2G^e\left(1-\frac{I_1}{4G^e}\right)\boldsymbol{P}^d \tag{8.13-1}$$

$$\boldsymbol{C}^{ed}(I_1) = \frac{1}{3B^e}\boldsymbol{P}^s + \frac{2}{4G^e - I_1}\boldsymbol{P}^d \tag{8.13-2}$$

and Eq. (8.9-2) becomes

$$S^2 = \frac{\bar{S}^2}{\left[2G^e\left(1-\frac{I_1}{4G^e}\right)\right]^2} \tag{8.14}$$

In order to make the effective strain increase with the damage process, choose

$$\bar{S} = \bar{\sigma}_L\left(1-\frac{I_1}{4G^e}\right)^{\frac{1}{2}} \tag{8.15}$$

where $\bar{\sigma}_L$ denotes the limit effective stress. Substituting Eq. (8.15) into Eq. (8.14) and defining $\bar{\varepsilon}_L = \frac{\bar{\sigma}_L}{2G^e}$, we can get

$$f^d = \boldsymbol{\varepsilon} : \boldsymbol{R} : \boldsymbol{\varepsilon} - \frac{\bar{\varepsilon}_L}{1 - \frac{I_1}{4G^e}} \tag{8.16}$$

As can be seen from Eqs. (8.15) and (8.16), the effective stress reduces with the increase of the effective strain, which is a feature typical of damage softening.

The above gives all the equations necessary to construct Eqs. (7.17) for a strain-based damage model or Eqs. (7.33) for a stress-based damage model. It is now obvious that both Eqs. (7.17) and (7.33) are related to each other. With the material parameters $B^e = 24GPa$, $G^e = 18GPa$, and $\bar{\sigma}_L = 50MPa$, Figure 8-2 illustrates the loading and unloading of the simple damage model. As can be seen, no permanent deformation occurs after unloading, as expected for a damage model.

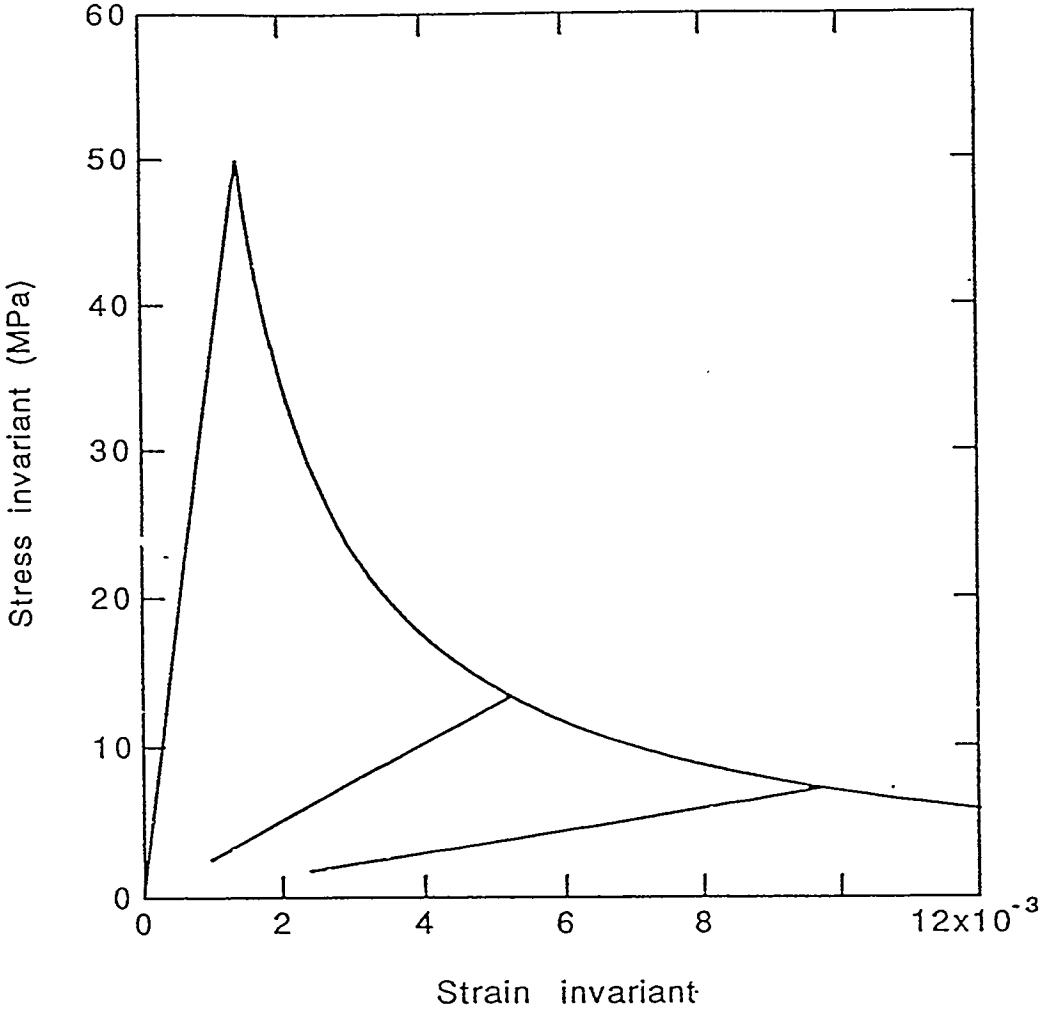

Figure 8-2. Loading and unloading of the damage model.

9. CONCLUSIONS

An effort has been made in this report to investigate, from experimental, theoretical, and computational points of view, nonlinear response features exhibited by quasi-brittle materials with emphasis on concrete. Based on the internal variable theory of thermodynamics, the general formulations of plasticity and damage models are given as useful tools to simulate two distinct modes of microstructural changes: inelastic flow and degradation of material properties, which identify the phenomenological nonlinear behavior of quasi-brittle materials as displayed in conventional experiments. Since the overall accuracy of nonlinear structural analyses depends not only on the unique characteristics of the stress-strain and load-displacement spaces but also on the relation between these two spaces, the computational aspects of plasticity and damage models are explored with respect to their effects on structural analyses. Thus, numerical schemes listed in Chapters 4 and 7 will make the various models discussed here available to users of advanced computational codes.

Because of the complexity of quasi-brittle materials, inelasticity, and damage models discussed in this report are still not satisfactory in the sense that some important nonlinear phenomena such as anisotropy, softening with localization, and coupled inelastic flow and damage can not be described. With the increased understanding of failure mechanisms, however, more suitable models for concrete can be developed in a systematic manner from the general formulations given in this report. An extensive list of references also gives valuable information for future research and application.

Since each specific constitutive model represents an attempt to correct a deficiency in existing models, this report provides the means for selecting a constitutive model according to the degree of accuracy that is needed. Starting with the simplest model, it is shown how additional features can be included to simulate the behavior of concrete. Limitations of models are discussed to indicate reasonable expectations of what current formulations can provide. A point which should be emphasized is that even though no single model is completely satisfactory, there do exist formulations which are a significant improvement over the most elementary plasticity models. With only a slight increase in computer cost and theoretical sophistication, such formulations can easily be incorporated into existing computational codes.

10. REFERENCES

Atkinson, K.E. 1978. *An Introduction to Numerical Analysis.* New York, NY: John Wiley & Sons.

Bathe, K.J. 1982. *Finite Element Procedures in Engineering Analysis.* Englewood Cliffs, NJ: Prentice-Hall, Inc.

Bazant, Z.P., and G. Pijaudier-Cabot. 1988. "Nonlocal Continuum Damage, Localization Instability and Convergence," *Journal of Applied Mechanics.* Vol. 55, no. 2, 287-293.

Belytschko, T. 1983. "An Overview of Semidiscretization and Time Integration Procedures," *Computational Methods for Transient Analysis.* Eds. T. Belytschko and T.J.R. Hughes. Computational Methods in Mechanics Vol. 1. New York, NY: North-Holland. 1-65.

Chen, E.P., and D.Y. Tzou. 1990. "A Continuum Damage Model for the Quasi-Static Response of Brittle Materials," *Micromechanics of Failure of Quasi-Brittle Materials, Proceedings of the International Conference on Micromechanics of Failure of Quasi-Brittle Materials, Albuquerque, NM, June 6-8, 1990.* Eds. S.P. Shah, S.E. Swartz, and M.L. Wang. New York, NY: Elsevier Applied Science. p. 620.

Chen, W.F. 1982. *Plasticity in Reinforced Concrete.* New York, NY: McGraw-Hill Book Co.

Chen, Z. 1989. "Nonlocal Theoretical and Numerical Investigations of Soil-Concrete Interfaces." Ph.D. dissertation. Albuquerque, NM: University of New Mexico.

Chen, Z., and H.L. Schreyer. 1987. "Simulation of Soil-Concrete Interfaces with Nonlocal Constitutive Models," *Journal of Engineering Mechanics.* Vol. 113, no. 11, 1665-1677.

Chen, Z., and H.L. Schreyer. 1989. "A Numerical Solution Scheme for Softening Problems Involving Total Strain Control," *Computers and Structures.* Vol. 37, no. 6, 1043-1050.

Chen, Z., and H.L. Schreyer. 1990. "Failure-Controlled Solution Strategies for Damage Softening with Localization," *Micromechanics of Failure of Quasi-Brittle Materials, Proceedings of the International Conference on Micromechanics of Failure of Quasi-Brittle Materials, Albuquerque, NM, June 6-8, 1990.* Eds. S.P. Shah, S.E. Swartz, and M.L. Wang. New York, NY: Elsevier Applied Science. p. 135.

Chen, Z., M.K. Neilsen, and H.L. Schreyer. 1992. "A Secant Structural Solution Scheme for Incremental Damage and Plasticity," *Constitutive Laws for Engineering Materials: Recent Advances and Industrial and Infrastructure Applications, Proceedings of the Third International Conference, Tucson, AZ, January 7-12, 1991.* Eds. C.S. Desai, E. Krempl, G. Frantziskonis, and H. Saadatmanesh. New York, NY: ASME Press. 677-682.

Coleman, B.D., and M.E. Gurtin. 1967. "Thermodynamics with Internal State Variables," *Journal of Chemical Physics.* Vol. 47, no. 2, 597-613.

Coleman, B.D., and W. Noll. 1963. "The Thermodynamics of Elastic Materials with Heat Conduction and Viscosity," *Archives of Rational Mechanical Analysis.* Vol. 13, 167-178.

Costin, L.S., and C.M. Stone. 1987. *A Finite Element Material Model for Microfracture-Damaged Brittle Rock.* SAND87-1227. Albuquerque, NM: Sandia National Laboratories.

Desai, C.S., and H.J. Siriwardane. 1984. *Constitutive Laws for Engineering Materials with Emphasis on Geologic Materials.* Englewood Cliffs, NJ: Prentice-Hall, Inc.

Faruque, M.O., and C.J. Chang. 1986. "New Cap Model for Failure and Yielding of Pressure-Sensitive Materials," *Journal of Engineering Mechanics.* Vol. 112, no. 10, 1041-1053.

Gear, C.W. 1971. *Numerical Initial Value Problems in Ordinary Differential Equations.* Englewood Cliffs, NJ: Prentice-Hall, Inc.

Gopalaratnam, V.S., and S.P. Shah. 1985. "Softening Response of Plain Concrete in Direct Tension," *Journal of the American Concrete Institute*. Vol. 82, no. 3, 310-323.

Golub, G.H., and C.F. van Loan. 1983. *Matrix Computations*. Baltimore, MD: The Johns Hopkins University Press.

Green, S.J., and S.R. Swanson. 1973. *Static Constitutive Relations for Concrete.* AFWL-TR-72-244. Albuquerque, NM: Air Force Weapons Laboratory, Kirtland Air Force Base.

Hill, R. 1950. *The Mathematical Theory of Plasticity*. London: Oxford University Press.

Hughes, T.J.R. 1983. "Analysis of Transient Algorithms with Particular Reference to Stability Behavior," *Computational Methods for Transient Analysis.* Eds. T. Belytschko and T.J.R. Hughes. Computational Methods in Mechanics Vol. 1. New York, NY: North-Holland. 67-155.

Kachanov, L.M. 1986. *Introduction to Continuum Damage Mechanics*. Boston, MA: Martinus Nijhoff Publishers.

Kovarna, J. 1981. *Fitter: A General Nonlinear Curve Fitter Code.* AFWL-TR-80-123. Albuquerque, NM: Air Force Weapons Laboratory, Kirtland Air Force Base.

Krajcinovic, D. 1989. "Damage Mechanics," *Mechanics of Materials*. Vol. 8, no. 2/3, 117.

Kupfer, H., H.K. Hilsdorf, and H. Rusch. 1969. "Behavior of Concrete Under Biaxial Stresses," *ACI Journal.* Vol. 66, no. 52, 656.

Lemaitre, J. 1984. "How to Use Damage Mechanics," *Nuclear Engineering and Design.* Vol. 80, no. 2, 233-245.

Maji, A.K., D. Leeman, and J. Wang. 1990. "Observation of Tensile Fracture by Laser Interferometry," *Micromechanics of Failure of Quasi-Brittle Materials, Proceedings of the International Conference on Micromechanics of Failure of Quasi-Brittle Materials*, Eds. S.P. Shah, S.E. Swartz, and M.L. Wang. New York, NY: Elsevier. 43.

Malvern, L.E. 1969. *Introduction to the Mechanics of a Continuous Medium.* Englewood Cliffs, NJ: Prentice-Hall, Inc.

Marsden, J.E., and T.J.R. Hughes. 1983. *Mathematical Foundations of Elasticity.* Englewood Cliffs, NJ: Prentice-Hall, Inc.

Martin, J.B. 1975. *Plasticity.* Cambridge, MA: The MIT Press.

Neilsen, M.K., Z. Chen, and H.L. Schreyer. 1991. "A Structural Constitutive Algorithm Based on Continuum Damage Mechanics for Softening with Snap-Back," *Constitutive Laws for Engineering Materials: Recent Advances and Industrial and Infrastructure Applications, Proceedings of the Third International Conference, Tucson, AZ, January 7-12, 1991.* Eds. C.S. Desai, E. Krempl, G. Frantziskonis, and H. Saadatmanesh. New York, NY: ASME Press. 751-754.

Neville, A.M., and J.J. Brooks. 1987. *Concrete Technology.* Harlow, Essex, UK: Longman Scientific and Technical; New York, NY: John Wiley.

Norman, C.D. 1990. *Evaluation of Nonlinear Constitutive Properties of Concrete.* SL-90-1. Vicksburg, MS: Army Engineer Waterways Experiment Station.

Ortiz, M. 1987. "An Analytical Study of the Localized Failure Modes of Concrete," *Mechanics of Materials.* Vol. 6, no. 2, 159-174.

Ortiz, M., and E.P. Popov. 1985. "Accuracy and Stability of Integration Algorithms for Elastoplastic Constitutive Relations," *International Journal for Numerical Methods in Engineering.* Vol. 21, no. 9, 1561-1576.

Resende, L., and J.B. Martin. 1985. "Formulation of Drucker-Prager Cap Model," *Journal of Engineering Mechanics.* Vol. 111, no. 7, 855-881.

Sandler, I.S., and D. Rubin. 1979. "An Algorithm and a Modular Subroutine for the Cap Model," *International Journal for Numerical and Analytical Methods in Geomechanics*. Vol. 3, 173-186.

Sandler, I.S., F.L. Dimaggio, and G.Y. Baladi. 1976. "Generalized Cap Model for Geological Materials," *Journal of the Geotechnical Engineering Division ASCE*. Vol. 102, no. GT7, 683-699.

Schreyer, H.L., and S.M. Babcock. 1985. "A Third-Invariant Plasticity Theory for Low-Strength Concrete," *Journal of Engineering Mechanics*. Vol. III, no. 4, 545-558.

Schreyer, H.L., and Z. Chen. 1986. "One Dimensional Softening with Localization," *Journal of Applied Mechanics*. Vol. 53, no. 4, 791-797.

Schreyer, H.L., and M.L. Wang. 1990. "Elementary Constitutive Relations for Quasi-Brittle Materials Based on Continuum Damage Mechanics," *Micromechanics of Failure of Quasi-Brittle Materials, Proceedings of the International Conference on Micromechanics of Failure of Quasi-Brittle Materials, Albuquerque, NM, June 6-8, 1990.* Eds. S.P. Shah, S.E. Swartz, and M.L. Wang. New York, NY: Elsevier. 95.

Simo, J.C., and J.W. Ju. 1987. "Strain- and Stress-Based Continuum Damage Models — I. Formulation," *International Journal of Solids and Structures*. Vol. 23, no. 7, 821-840.

Simo, J.C., J.W. Ju, K.S. Pister, and R.L. Taylor. 1988. "Assessment of Cap Model: Consistent Return Algorithms and Rate-Dependent Extension," *Journal of Engineering Mechanics*. Vol. 114, no. 2, 191-218.

Taylor, L.M., E.P. Chen, and J.S. Kuszmaul. 1986. "Microcrack-Induced Damage Accumulation in Brittle Rock under Dynamic Loading," *Computer Methods in Applied Mechanics and Engineering*. Vol. 55, no. 3, 301-320.

Truesdell, C. 1984. *Rational Thermodynamics*. 2nd ed. New York, NY: Springer-Verlag.

Underwood, P. 1983. "Dynamic Relaxation," *Computational Methods for Transient Analysis*. Eds. T. Belytschko and T.J.R. Hughes. New York, NY: Elsevier. 245-265.

Van Mier, J.G.M. 1984. "Strain-Softening of Concrete Under Multiaxial Loading Conditions." Ph.D. dissertation. The Netherlands: University of Eindhoven.

Vermeer, P.A., and R. de Borst. 1984. "Non-Associated Plasticity for Soils, Concrete and Rock," *Heron* (The Netherlands). Vol. 29, no. 3, 64 pp.

Wang, M.L., H.L. Schreyer, and G.A. Rutland. 1990. "Internal Deformation Measurements with the Use of Real Time X-Rays," *Micromechanics of Failure of Quasi-Brittle Materials, Proceedings of the International Conference on Micromechanics of Failure of Quasi-Brittle Materials*. Eds. S.P. Shah, S.E. Swartz, and M.L. Wang. New York, NY: Elsevier. 81.

Wawersik, W.R., W.A. Olsson, D.J. Holcomb, J.W. Rudnicki, and K.T. Chau. 1990. "Localization of Deformation in Brittle Rock: Laboratory and Theoretical Investigations," *Micromechanics of Failure of Quasi-Brittle Materials, Proceedings of the International Conference on Micromechanics of Failure of Quasi-Brittle Materials*. Eds. S.P. Shah, S.E. Swartz, and M.L. Wang. New York, NY: Elsevier Applied Science. 115.

White, G.R. 1977. *Concrete Technology*. Albany, NY: Delmar Publishers.

Yazdani, S., and H.L. Schreyer. 1988. "An Anisotropic Damage Model with Dilatation for Concrete," *Mechanics of Materials*. Vol. 7, no. 3, 231.

Yazdani, S., and H.L. Schreyer. 1990. "A Combined Plasticity and Damage Mechanics Model for Plain Concrete," *Journal of Engineering Mechanics*. Vol. 116, no. 7, 1435.

This Page Intentionally Left Blank

WIPP PERFORMANCE ASSESSMENT DISTRIBUTION LIST

(Send Distribution list changes to F. Puffer, Tech Reps. Inc.,
5000 Marble NE, Albuquerque, NM 87110, (505) 266-5678, FAX: (505) 265-2687)
9/22/95

Federal Agencies

US Department of Energy (6)
Office of Civilian Radioactive Waste Management
Attn: Deputy Director, RW-2
Associate Director, RW-10/50
Office of Program and Resources Management
Office of Contract Business Management
Director, RW-22, Analysis and Verification Division
Associate Director, RW-30
Office of Systems and Compliance
Associate Director, RW-40
Office of Storage and Transportation
Director, RW-4/5
Office of Strategic Planning and International Programs Office of External Relations
Forrestal Building
Washington, DC 20585

US Department of Energy
Albuquerque Operations Office
Attn: National Atomic Museum Library
PO Box 5400
Albuquerque, NM 87185

US Department of Energy
Office of Environmental Restoration and Waste Management
Attn: C. Frank, EM-50
Washington, DC 20585

US Department of Energy (3)
Office of Environmental Restoration and Waste Management
Attn: M. Frei, EM-34 / Trevion II
Director, Waste Management Projects
Washington, DC 20585-0002

US Department of Energy
Office of Environmental Restoration and Waste Management
Washington, DC 20585-0002

US Department of Energy
Office of Environmental Restoration and Waste Management
Attn: S. Schneider, EM-342
Trevion II
Washington, DC 20585-0002

US Department of Energy (3)
WIPP Task Force
Attn: G.H. Daly
S. Fucigna
B. Bower
12800 Middlebrook Rd., Suite 400
Germantown, MD 20874

US Department of Energy (3)
Office of Environment, Safety and Health
Attn: R.P. Berube, EH-20
R. Pelletier, EH-231
K. Taimi, EH-232
Washington, DC 20585

US Department of Energy (2)
WIPP Project Integration Office
Attn: S. Alcorn
L.W. Gage
PO Box 5400
Albuquerque, NM 87115-5400

US Department of Energy, AL/ERD
UMTRA Project Office
Attn: J. Coffey
2155 Louisiana, NE, #4000
Albuquerque, NM 87111

US Department of Energy
OMD
Attn: P.J. Higgins
PO Box 5400
Albuquerque, NM 87115-5400

US Department of Energy
WIPP Project Integration Satellite Office
Attn: R. Becker
PO Box 3090, Mail Stop 525
Carlsbad, NM 88221-3090

US Department of Energy (6)
Carlsbad Operations Center
Attn: A. Hunt (4)
L. Lippis
K. Hunter
PO Box 3090
Carlsbad, NM 88221-3090

US Department of Energy
Office of NEPA Policy and Assistance
EH-42
Attn: Carolyn Osborn
Stephen Simpson
1000 Independence Ave., SW
Washington, DC 20585

US Department of Energy
Research & Waste Management Division
Attn: Director
PO Box E
Oak Ridge, TN 37831

US Department of Energy (2)
Idaho Operations Office
Office of Waste Management
Attn: George Wells
805 Energy Dr., MS-1118
Idaho Falls, ID 83402

US Department of Energy
Savannah River Operations Office
Defense Waste Processing
Facility Project Office
Attn: W.D. Pearson
PO Box A
Aiken, SC 29802

US Department of Energy (2)
Richland Operations Office
Waste Management Division
Attn: R. E. Westerman
1804 Marshall
PO Box 550
Richland, WA 99352

US Department of Energy
Richland Operations Office
Solid Waste Programs
Attn: Rudy F. Guercia
PO Box 550, S7-55
Richland, WA 99352

US Department of Energy
Yucca Mountain Project Office
Attn: Project Manager
PO Box 98608
Las Vegas, NV 89193-8608

US Department of Energy (3)
Nevada Operations Office
Attn: J.R. Boland
D. Livingston
P.K. Fitzsimmons
2753 S. Highland Drive
Las Vegas, NV 89183-8518

US Department of Energy (2)
Technical Information Center
PO Box 62
Oak Ridge, TN 37831

US Department of Energy (2)
Chicago Operations Office
Attn: J.C. Haugen
9800 South Cass Avenue
Argonne, IL 60439

US Department of Energy (3)
Rocky Flats Field Office
Attn: W.C. Rask
G. Huffman
T. Lukow
PO Box 928
Golden, CO 80402-0928

US Department of Energy
Los Alamos Area Office
Attn: D. Bruce Lebrun
528 35th Street
Los Alamos, NM 87544

US Department of Energy
Ohio Field Office
Attn: R. Grandfield
PO Box 3020
Miamisburg, OH 45343-3020

US Bureau of Land Management
Carlsbad Resource Area
PO Box 1778
Carlsbad, NM 88221-1778

US Bureau of Land Management
New Mexico State Office
PO Box 27115
Santa Fe, NM 87502-7115

US Environmental Protection Agency (2)
Radiation Protection Programs
Attn: Al Colli (6602J)
401 M Street, SW
Washington, DC 20460

US Environmental Protection Agency,
Region 6
Attn: C. Byrum, 6T-ET
1445 Ross Ave.
Dallas, TX 75202

US Geological Survey (2)
Water Resources Division
Attn: C. Peters
4501 Indian School NE
Suite 200
Albuquerque, NM 87110

US Nuclear Regulatory Commission
Division of Waste Management
Attn: H. Marson
Mail Stop 4-H-3
Washington, DC 20555

US Nuclear Regulatory Commission (4)
Advisory Committee on Nuclear Waste
Attn: D. Moeller
M.J. Steindler
P.W. Pomeroy
W.J. Hinze
11555 Rockville Pike
Rockville, MD 20852-2738

Defense Nuclear Facilities Safety Board
Attn: D. Winters
625 Indiana Ave. NW, Suite 700
Washington, DC 20004

Nuclear Waste Technical Review Board
Attn: Library (2)
1100 Wilson Blvd., Suite 910
Arlington, VA 22209-2297

State Agencies

New Mexico Bureau of Mines and Mineral
Resources
Socorro, NM 87801

New Mexico Energy, Minerals and Natural Resources Department
Attn: Librarian
2040 South Pacheco
Santa Fe, NM 87505

New Mexico Energy, Minerals and Natural Resources Department
NM Radioactive Waste ConsultationTask Force (2)
(Governor's WIPP Task Force)
Attn: Jennifer Salisbury, Chairwoman
Chris Wentz, Senior Policy Analyst
2040 South Pacheco
Santa Fe, NM 87505

Bob Forrest
Mayor, City of Carlsbad
PO Box 1569
Carlsbad, NM 88221

Carlsbad Department of Development
Executive Director
Attn: Mark Donham
PO Box 1090
Carlsbad, NM 88221-1090

New Mexico Environment Department
Secretary of the Environment (3)
Attn: J. Espinosa
PO Box 968
1190 St. Francis Drive
Santa Fe, NM 87503-0968

New Mexico Environment Department
Attn: P. McCasland
WIPP Project Site Office
PO Box 3090
Carlsbad, NM 88221-3090

New Mexico State Engineer's Office
Attn: M. Chudnoff
PO Box 25102
Santa Fe, NM 87504-5102

Environmental Evaluation Group (5)
Attn: R. Neill
7007 Wyoming Blvd. NE, Suite F-2
Albuquerque, NM 87109

Advisory Committee on Nuclear Facility Safety

John F. Ahearne
Sigma Xi
PO Box 13975
Research Triangle Park, NC 27709

James E. Martin
109 Observatory Road
Ann Arbor, MI 48109

WIPP Committee, National Research Council's Board on Radioactive Waste Management

National Research Council (2)
Board on Radioactive Waste Management
Attn: C.A. Anderson
I.B. Alterman
2101 Constitution Ave. NW
Harris Bldg. HA 456
Washington, DC 20418

Howard Adler
Oxyrase, Inc.
7327 Oak Ridge Highway
Knoxville, TN 37931

John O. Blomeke
720 Clubhouse Way
Knoxville, TN 37909

John D. Bredehoeft
Western Region Hydrologist
Water Resources Division
US Geological Survey (M/S 439)
345 Middlefield Road
Menlo Park, CA 94025

Rodney C. Ewing
Department of Geology
University of New Mexico
Albuquerque, NM 87131

Charles Fairhurst
Dept. of Civil and Mineral Engineering
University of Minnesota
500 Pillsbury Dr. SE
Minneapolis, MN 55455-0220

B. John Garrick
PLG, Incorporated
4590 MacArthur Blvd., Suite 400
Newport Beach, CA 92660-2027

Leonard F. Konikow
US Geological Survey
431 National Center
Reston, VA 22092

Christopher G. Whipple
ICF Kaiser Engineers
1800 Harrison St., 7th Floor
Oakland, CA 94612-3430

Thomas A. Zordan
Zordan Associates, Inc.
3807 Edinburg Dr.
Murrysville, PA 15668

Performance Assessment Peer Review Panel

G. Ross Heath
College of Ocean & Fishery Sciences
University of Washington
1013 NE 40th Street
Seattle, WA 98105-6698

Thomas H. Pigford
University of California
166 Alpine Terrace
Oakland, CA 94618

Thomas A. Cotton
JK Research Associates, Inc.
4429 Butterworth Place NW
Washington, DC 20016

Robert J. Budnitz
President, Future Resources Associates, Inc.
2039 Shattuck Ave., Suite 402
Berkeley, CA 94704

C. John Mann
Department of Geology
245 Natural History Bldg.
1301 West Green Street
University of Illinois
Urbana, IL 61801

Frank W. Schwartz
Department of Geology and Mineralogy
The Ohio State University
Scott Hall
1090 Carmack Rd.
Columbus, OH 43210

National Laboratories

Argonne National Laboratory
Attn: A. Smith
9700 South Cass, Bldg. 201
Argonne, IL 60439

Argonne National Laboratory
Attn: D. Tomasko
9700 South Cass, Bldg. 900
Argonne, IL 60439

Battelle Pacific Northwest Laboratory (2)
Attn: S. Bates
R.E. Westerman
MSIN P8-44
Battelle Boulevard
Richland, WA 99352

Idaho National Engineering Laboratory (2)
Westinghouse-Idaho Nuclear Co.
Attn: H. Loo
R. Klingler
PO Box 4000, Mail Stop 3422
Idaho Falls, ID 83415-3422

Los Alamos National Laboratory (4)
Attn: M. Ennis, HS-12, Mail Stop J900
S. Kosiewicz, EM-7, Mail Stop J595
L. Soholt, EM-13, Mail Stop M992
J. Wenzel, HS-12, Mail Stop K482
PO Box 1663
Los Alamos, NM 87545

Lockheed Martin Energy Systems, Inc.
Attn: Thomas H. Monk
PO Box 2008
Oak Ridge, TN 37831-6023

Sandia National Laboratories
Attn: H. Richard Yoshimura
PO Box 5800
Albuquerque, NM 87185-0718

Westinghouse–Savannah River Technology Center (4)
Attn: N. Bibler
J.R. Harbour
M.J. Plodinec
G.G. Wicks
Aiken, SC 29802

Corporations/Members of the Public

Benchmark Environmental Corp.
Attn: C. Frederickson
4501 Indian School NE, Suite 105
Albuquerque, NM 87110

Beta Corporation Int.
Attn: E. Bonano
671 9-D Academy Road, NE
Albuquerque, NM 87109

City of Albuquerque
Public Works Department
Utility Planning Division
Attn: W.K. Summers
PO Box 1293
Albuquerque, NM 87103

Prindle Hinds Environmental, Inc.
Attn: R.W. Prindle, P.E.
7208 Jefferson NE
Albuquerque, NM 87109

Disposal Safety, Inc.
Attn: B. Ross
1660 L Street NW, Suite 314
Washington, DC 20036

Ecodynamics (2)
Attn: P. Roache
R. Blaine
PO Box 9229
Albuquerque, NM 87119-9229

EG & G Idaho
1955 Fremont Street
Attn: T.I. Clements
Idaho Falls, ID 83415

Geomatrix
Attn: K. Coppersmith
100 Pine St., Suite 1000
San Francisco, CA 94111

Golder Associates, Inc.
Attn: R. Kossik
4104 148th Avenue NE
Redmond, WA 98052

John Hart and Associates, P.A.
Attn: J.S. Hart
2815 Candelaria Road NW
Albuquerque, NM 87107

John Hart and Associates, P.A.
Attn: K. Lickliter
8130 Camino Del Venado NW
Albuquerque, NM 87120

Joe P. Harvill
WIPP Technical Assistance Contractor
PO Box 1270
Carlsbad, NM 88220

INTERA, Inc.
Attn: A.M. LaVenue
1650 University Blvd. NE, Suite 300
Albuquerque, NM 87102

INTERA, Inc.
Attn: J.F. Pickens
6850 Austin Center Blvd., Suite 300
Austin, TX 78731

INTERA, Inc.
Attn: W. Stensrud
PO Box 2123
Carlsbad, NM 88221

INTERA, Inc.
Attn: W. Nelson
101 Convention Center Dr., Suite 540
Las Vegas, NV 89109

IT Corporation (2)
Attn: R.F. McKinney
J. Myers
Regional Office, Suite 700
5301 Central Avenue NE
Albuquerque, NM 87108

W. E. Kennedy, Jr.
c/o Dade Moeller & Associates
1845 Terminal Dr., Suite 140
Richland, WA 99352

Lawrence Berkeley Laboratory
Attn: J. Long
Building 50 E
Berkeley, CA 94720

Morgan, Lewis & Bockius
Attn: M.A. Bauser
1800 M. Street NW
Washington, DC 20036

NMERI
Attn: Z. Chen (10)
University of New Mexico
Albuquerque, NM 87131

RE/SPEC, Inc. (2)
Attn: Angus Robb
4775 Indian School NE, Suite 300
Albuquerque, NM 87110

RE/SPEC, Inc.
Attn: J.L. Ratigan
PO Box 725
Rapid City, SD 57709

Reynolds Electric and Engineering
Company, Inc.
Attn: E.W. Kendall
3281 S. Highland, Suite 807
Las Vegas, NV 89109

SAIC
Attn: H.R. Pratt
10260 Campus Point Drive
San Diego, CA 92121

SAIC
Attn: C.G. Pflum
101 Convention Center Dr.
DA-3
Las Vegas, NV 89109

SAIC (3)
Attn: M. Davis
R. Guzowski
J. Tollison
2109 Air Park Road SE
Albuquerque, NM 87106

SAIC (2)
Attn: J. Young
D. Lester
18706 North Creek Parkway, Suite 110
Bothell, WA 98011

Southwest Research Institute
Nuclear Waste Regulatory Analysis (2)
Attn: P.K. Nair
6220 Culebra Road
San Antonio, TX 78228-0510

Southwest Research Institute
Attn: Dr. Hersh K. Manaktala
PO Drawer 28510
San Antonio, TX 78228

Systems, Science, and Software (2)
Attn: E. Peterson
P. Lagus
Box 1620
La Jolla, CA 92038

TASC
Attn: S.G. Oston
55 Walkers Brook Drive
Reading, MA 01867

Tech Reps, Inc. (4)
Attn: J. Chapman
F. Puffer
T. Peterson
D. Scott
5000 Marble NE
Albuquerque, NM 87110

Tolan, Beeson & Associates
Attn: T.L. Tolan
2320 W. 15th Avenue
Kennewick, WA 99337

TRW Environmental Safety Systems (2)
Attn: I. Sacks, Suite 800
L. Wildman, Suite 1300
2650 Park Tower Drive
Vienna, VA 22180-7306

Sanford Cohen and Associates
Attn: J. Channell
7101 Carriage Rd NE
Albuquerque, NM 87109

Westinghouse Electric Corporation (5)
Attn: Library
C. Cox
L. Fitch
B.A. Howard
R.F. Kehrman
PO Box 2078
Carlsbad, NM 88221

Westinghouse Hanford Company
Attn: D.E. Wood, MSIM H6-30
PO Box 1970
Richland, WA 99352

Western Water Consultants
Attn: P.A. Rechard
PO Box 4128
Laramie, WY 82071

Western Water Consultants
Attn: D. Fritz
1949 Sugarland Drive, #134
Sheridan, WY 82801-5720

WTECH
Attn: Carl Hess
101 E. Mermod
Carlsbad, NM 88220

P. Drez
8816 Cherry Hills Road NE
Albuquerque, NM 87111

David Lechel
9600 Allende Rd. NE
Albuquerque, NM 87109

C.A. Marchese
PO Box 21790
Albuquerque, NM 87154

Arend Meijer
3821 Anderson SE
Albuquerque, NM 87108

D.W. Powers
HC 12 Box 87
Anthony, TX 79821

Shirley Thieda
PO Box 2109, RR1
Bernalillo, NM 87004

Jack Urich
c/o CARD
144 Harvard SE
Albuquerque, NM 87106

Universities

University of California
Mechanical, Aerospace, and Nuclear Engineering Department
Attn: D. Browne
5532 Boelter Hall
Los Angeles, CA 90024

University of California
Nuclear Engineering Department
Attn: W. Kastenberg
4153 Etcheverry Hall
Berkeley, CA 94720-1730

University of California
Engineering and Applied Science
Attn: D. Okrent
48-121A Engineering IV
Los Angeles, CA 90024-1597

University of California
Mine Engineering Department
Rock Mechanics Engineering
Attn: N. Cook
Berkeley, CA 94720

University of Hawaii at Hilo
Business Administration
Attn: S. Hora
Hilo, HI 96720-4091

University of Illinois
Department of Geology
Attn: C. Bethke
1301 W. Green St.
Urbana, IL 61801

University of New Mexico
Geology Department
Attn: Library
Albuquerque, NM 87131

University of New Mexico (5)
Mechanical Engineering
Attn: H. Schreyer
102 Scholes Hall
Albuquerque, NM 87131

University of Wyoming
Department of Civil Engineering
Attn: V.R. Hasfurther
Laramie, WY 82071

Libraries

Thomas Brannigan Library
Attn: D. Dresp
106 W. Hadley St.
Las Cruces, NM 88001

New Mexico State Library
Southwest Room
Attn: N. McCallan
325 Don Gaspar
Santa Fe, NM 87501-2777

New Mexico Tech Library
Government Documents
Campus Station
Socorro, NM 87801

New Mexico Junior College
Pannell Library
Library Acquisitions
Attn: Karen Elliott
5317 Lovington Highway
Hobbs, NM 88240

Carlsbad Museum
WIPP Public Reading Room
Attn: Pat Jablonsky
418 W. Fox Street
Carlsbad, NM 88220

University of New Mexico
Zimmerman Library
Government Publications Department
Albuquerque, NM 87131

NEA/Performance Assessment Advisory Group (PAAG)

P. Duerden
ANSTO
Lucas Heights Research Laboratories
Private Mail Bag No. 1
Menai, NSW 2234
AUSTRALIA

Gordon S. Linsley
Division of Nuclear Fuel Cycle and Waste Management
International Atomic Energy Agency
PO Box 100
A-1400 Vienna
AUSTRIA

Nicolo Cadelli
Commission of European Communities
200, Rue de la Loi
B-1049 Brussels
BELGIUM

J. Marivoet
Centre d'Etudes de l'Energie Nucléaire (CEN/SCK)
Boeretang 200
B-2400 Mol
BELGIUM

P. Conlon
Waste Management Division
Atomic Energy Control Board (AECB)
PO Box 1046
Ottawa, Ontario KIP 559
CANADA

A.G. Wikjord
Manager, Environmental and Safety Assessment Branch, AECL
Whiteshell Laboratories
Pinawa, Manitoba ROE 1LO
CANADA

Teollisuuden Voima Oy (TVO) (2)
Attn: Timo Äikäs
Jukka-Pekka Salo
Annankatu 42 C
SF-00100 Helsinki Suomi
FINLAND

Timo Vieno
VTT Energy
PO Box 1604
FIN-02044 VTT
FINLAND

Division de la Sécurité et de la Protection de l'Environment (DSPE)
Commissariat á l'Energie Atomique
Agence Nationale pour la Gestion des Déchets Radioactifs (ANDRA)
Attn: Gérald Ouzounian
Route du Panorama Robert Schuman
B. P. No. 38
F-92266 Fontenay-aux-Roses Cedex
FRANCE

ANDRA/DRI
Attn: M. Claude Ringeard
1/7 Rue Jean Monnet
92.298 Chatenay-Malabry-Cedex
FRANCE

Claudio Pescatore
Division of Radiation Protection and
Waste Management
OECD Nuclear Energy Agency
38, Boulevard Suchet
F-75016 Paris
FRANCE

M. Dominique Greneche
Commissariat á l'Energie Atomique
IPSN/DAS/SASICC/SAED
B.P. No. 6
F-92265 Fontenay-aux-Roses Cedex
FRANCE

Robert Fabriol
Bureau de Recherches Géologiques et
Miniéres (BRGM)
B.P. 6009
45060 Orléans Cedex 2
FRANCE

P. Bogorinski
Gesellschaft für Reaktorsicherheit und
Reakforsicherheit (GRS) mhH
Schwertnergasse 1
50667 Köln
GERMANY

R. Storck
GSF - Institut für Tieflagerung
Theodor-Heuss-Strabe 4
D-3300 Braunschweig
GERMANY

Ferrucio Gera
ISMES S.p.A
Via Pastrengo 9
24068 Seriate, BG
ITALY

Hiroyuki Umeki
Isolation System Research Program
Radioactive Waste Management Project
Power Reactor and Nuclear Fuel
Development Corporation (PNC)
1-9-13, Akasaka, Minato-ku
Tokyo 107
JAPAN

Tönis Papp
SKB
Box 5864
S 102 40 Stockholm
SWEDEN

Conny Hägg
Swedish Radiation Protection Institute (SSI)
Box 60204
S-104 01 Stockholm
SWEDEN

J. Hadermann
Paul Scherrer Institute
Waste Management Programme
CH-5232 Villigen PSI
SWITZERLAND

J. Vigfusson
HSK-Swiss Nuclear Safety Inspectorate
Federal Office of Energy
CH-5232 Villigen-HSK
SWITZERLAND

D.E. Billington
Departmental Manager–Assessment Studies
Radwaste Disposal R&D Division
AEA Decommissioning & Radwaste
Harwell Laboratory, B60
Didcot Oxfordshire OX11 ORA
UNITED KINGDOM

P. Grimwood
Waste Management Unit, BNFL
Sellafield
Seascale, Cumbria CA20 1PG
UNITED KINGDOM

Alan J. Hooper
UK Nirex Ltd
Curie Avenue
Harwell, Didcot
Oxfordshire, OX11 ORH
UNITED KINGDOM

Jerry M. Boak
Yucca Mountain Project Office
US Department of Energy
PO Box 98608
Las Vegas, NV 89193

Seth M. Coplan, Chairman
US Nuclear Regulatory Commission
Division of HLW Management
Mail Stop 4-H-3
Washington, DC 20555

A.E. Van Luik
Yucca Mountain Site Characterization Office
PO Box 98608
Las Vegas, NV 89109

NEA/Probabilistic System Assessment Group (PSAG)

Shaheed Hossain
Division of Nuclear Fuel Cycle and Waste Management
International Atomic Energy Agency
Wagramerstrasse 5
PO Box 100
A-1400 Vienna
AUSTRIA

Eduard Hofer
Gesellschaft für Reaktorsicherheit (GRS) MBH
Forschungsgelände
D-8046 Garching
GERMANY

Andrea Saltelli
Commission of European Communities
Joint Resarch Centre of Ispra
I-21020 Ispra (Varese)
ITALY

Alejandro Alonso
Cátedra de Tecnología Nuclear
E.T.S. de Ingenieros Industriales
José Gutiérrez Abascal, 2
E-28006 Madrid
SPAIN

ENRESA (2)
Attn: M. A. Cuñado
F. J. Elorza
Calle Emilio Vargas, 7
E-28043 Madrid
SPAIN

Pedro Prado
CIEMAT
Instituto de Tecnología Nuclear
Avenida Complutense, 22
E-28040 Madrid
SPAIN

Björn Cronhjort
Royal Institute of Technology
Fladergrand 12
SWE-183 73 Taby
SWEDEN

Richard A. Klos
Paul-Scherrer Institute (PSI)
CH-5232 Villingen PSI
SWITZERLAND

Nationale Genossenschaft für die
Lagerung Radioaktiver Abfälle (2)
Attn: C. McCombie
F. Van Dorp
Hardstrasse 73
CH-5430 Wettingen
SWITZERLAND

N. A. Chapman
Intera Information Technologies
Park View House, 47 Burton Street
Melton Mowbray
Leicestershire LE13 1AE
UNITED KINGDOM

Daniel A. Galson
Galson Sciences Ltd.
5 Grosvenor House
Melton Road
Oakham
Rutland LE15 6AX
UNITED KINGDOM

David P. Hodgkinson
Intera Information Technologies
45 Station Road, Chiltern House
Henley-on-Thames
Oxfordshire RG9 1AT
UNITED KINGDOM

Brian G.J. Thompson
Department of the Environment: Her
Majesty's Inspectorate of Pollution
Room A5.33, Romney House
43 Marsham Street
London SW1P 2PY
UNITED KINGDOM

Intera Information Technologies
Attn: M.J.Apted
3609 South Wadsworth Blvd.
Denver, CO 80235

US Nuclear Regulatory Commission (2)
Attn: R. Codell
N. Eisenberg
Mail Stop 4-H-3
Washington, DC 20555

Battelle Pacific Northwest Laboratories
Attn: P.W. Eslinger
MS K2-32
PO Box 999
Richland, WA 99352

Center for Nuclear Waste Regulatory
Analysis (CNWRA)
Southwest Research Institute
Attn: B. Sagar
PO Drawer 28510
6220 Culebra Road
San Antonio, TX 78284

Geostatistics Expert Working Group (GXG)

Rafael L. Bras
R.L. Bras Consulting Engineers
44 Percy Road
Lexington, MA 02173

Jesus Carrera
Universidad Politècnica de Cataluñya
E.T.S.I. Caminos; Campus Nord; D-2
E-08034 Barcelona
SPAIN

Ghislain de Marsily (GXG Chairman)
Universite Pierre et Marie Curie
Laboratoire de Geologie Applique
4, Place Jussieu
T.26 - 5^{e} etage, Cabe 123
75252 Paris Cedex 05
FRANCE

Alain Galli
Centre de Geostatistique
Ecole des Mines de Paris
35 Rue St. Honore
77035 Fontainebleau
FRANCE

Christian Ravenne
Geology and Geochemistry Division
Institut Francais du Pétrole
1 & 4, Av. de Bois-Préau B.P. 311
92506 Rueil Malmaison Cedex
FRANCE

Peter Grindrod
INTERA Information Technologies Ltd.
Chiltern House
45 Station Road
Henley-on-Thames
Oxfordshire, RG9 1AT
UNITED KINGDOM

Alan Gutjahr
Department of Mathematics
NM Institute of Mining and Technology
Socorro, NM 87801

C. Peter Jackson
AEA Technology
424.4 Harewell
Didcot
Oxfordshire OX11 ORA
UNITED KINDGOM

Rae Mackay
Department of Civil Engineering
University of Newcastle Upon Tyne
Newcastle Upon Tyne NE1 7RU
UNITED KINGDOM

Steve Gorelick
Department of Applied Earth Sciences
Stanford University
Stanford, CA 94305-2225

Peter Kitanidis
60 Peter Coutts Circle
Stanford, CA 94305

Dennis McLaughlin
Parsons Laboratory
Room 48-209
Department of Civil Engineering
Massachusetts Institute of Technology
Cambridge, MA 02139

Shlomo P. Neuman
College of Engineering and Mines
Hydrology and Water Resources Dept.
University of Arizona
Tucson, AZ 85721

Yoram Rubin
Department of Civil Engineering
University of California
Berkeley, CA 94720

Foreign Addresses

ONDRAF
Attn: P. Manfroy
Place Madou 1 B.24-25
B. 1030 Brussels
BELGIUM

Studiecentrum Voor Kernenergie
Centre D'Energie Nucleaire
Attn: A. Bonne
SCK/CEN
Boeretang 200
B-2400 Mol
BELGIUM

Atomic Energy of Canada, Ltd. (2)
Chalk River Laboratories Waste
Management Operations
Attn: M.E. Stevens
B.W. Goodwin
Chalk River, Ontario, KOJ 1JO
CANADA

Juhani Vira
Teollisuuden Voima Oy (TVO)
Annankatu 42 C
SF-00100 Helsinki Suomi
FINLAND

Jean-Pierre Olivier
OECD Nuclear Energy Agency (2)
38, Boulevard Suchet
F-75016 Paris, FRANCE

Claude Sombret
Centre D'Etudes Nucleaires
De La Vallee Rhone
CEN/VALRHO
S.D.H.A. B.P. 171
30205 Bagnols-Sur-Ceze
FRANCE

Commissariat a L'Energie Atomique
Attn: D. Alexandre
Centre d'Études de Cadarache
13108 Saint Paul Lez Durance Cedex
FRANCE

Bundesministerium für Forschung und
Technologie
Postfach 200 706
5300 Bonn 2
GERMANY

Bundesanstalt für Geowissenschaften
und Rohstoffe
Attn: M. Langer
Postfach 510 153
D-30631 Hannover
GERMANY

Gesellschaft für Anlagen und
Reaktorsicherheit (GRS) mbH
Attn: B. Baltes
Theodor-Hess-Str. 4
38122 Braunschweig
GERMANY

Wolfgang Muller
1 STEC
Abteilung Abfallbeseitigung
Schwertnergasse 1
D-50667 Koln
GERMANY

Institut fur Bergbaukunde und
Bergwirtschaftslehre der Technishen
Universitat Clausthal
Attn: K. Kuhn
Erzstrasse 20
D-38678 Clausthal Zellerfeld
GERMANY

Bundesaunt fuer Strahlenschutz
Attn: P. Brenneke
PO Box 10 01 49
38201 Salzgitter
GERMANY

Shingo Tashiro
Radioactive Waste Management Center
Mori Building #15 8-10
Toranomon 2-Chrome
Minato-Ku, Tokyo, 105
JAPAN

Netherlands Energy Research Foundation
Attn: T. Prij
3 Westerduingwed
PO Box 1
1755 Zg Petten
THE NETHERLANDS

Johan Andersson
INTERA Information Technologies
Vallvagen 22
S-125 33 Alvsjo
SWEDEN

Fred Karlsson
Svensk Kärnbränsleforsorjning AB
SKB Library
Box 5864
102 40 Stockholm
SWEDEN

Nationale Genossenschaft für die
Lagerung Radioaktiver Abfälle (2)
Attn: S. Vomvoris
P. Zuidema
Hardstrasse 73
CH-5430 Wettingen
SWITZERLAND

AEA Technology
Attn: J.E. Tinson
B4244 Harwell Laboratory
Didcot, Oxfordshire OX11 ORA
UNITED KINGDOM

AEA Technology
Attn: J.H. Rees
B.424.4
Harwell
Oxon OX11 ORA
UNITED KINGDOM

AEA Technology
Attn: W.R. Rodwell
O44/A31 Winfrith Technical Centre
Dorchester
Dorset DT2 8DH
UNITED KINGDOM

D.R. Knowles
British Nuclear Fuels, plc
Risley, Warrington
Cheshire WA3 6AS, 1002607
UNITED KINGDOM

Internal

MS	Org.	
MS-0101	0001	C. Paul Robinson
MS-0102	0002	O.E. Jones
MS-0827	1511	D.K. Gartling
MS-0127	4515	D.P. Garber
MS-0724	6000	D.L. Hartley
MS-1324	6115	P.B. Davies
MS-1324	6115	R.L. Beauheim
MS-0750	6118	H.R. Westrich
MS-1320	6719	E.J. Nowak
MS-1322	6121	J.R. Tillerson
MS-1322	6121	Staff (7)
MS-1395	6701	L.E. Shephard
MS-1395	6700	S.Y. Pickering
MS-1335	6000	W.D. Weart
MS-1335	6705	M.Y. Chu
MS-1345	6115	A.R. Lappin
MS-1341	6706	A.L. Stevens
MS-1326	6300	F.W. Bingham
MS-1326	6313	L.S. Costin
MS-1345	6331	D.P. Gallegos
MS-1328	6749	D.R. Anderson
MS-1328	6741	H.N. Jow
MS-1328	6749	Staff (20)
MS-1395	6743	V.H. Slaboszewicz
MS-1395	6743	Staff (3)
MS-1341	6747	D.R. Schafer
MS-1341	6748	J.T. Holmes
MS-1341	6748	Staff (18)
MS-1343	6351	R.E. Thompson
MS-0746	6613	R.M. Cranwell
MS-0746	6613	C. Leigh
MS-0718	6641	R. Yoshimura, Acting
MS-1330	6352	Carol Michaels (2)
MS-1330	6352	NWM Library (20)
MS-0899	13414	Technical Library (5)
MS-0619	12615	Print Media
MS-0100	7613-2	Document Processing for DOE/OSTI (10)
MS-9018	8523-2	Central Technical Files